SCUOLA DI DOTTORATO
UNIVERSITÀ DEGLI STUDI DI MILANO-BICOCCA

MISSIONE 4
ISTRUZIONE
RICERCA

Department of **Earth and Environmental Sciences DISAT**

PhD program in **Chemical, Geological and Environmental Sciences**

Cycle **XXXVIII III**

Curriculum in **Geological Sciences**

NATURE BASED SOLUTIONS FOR URBAN REGENERATION: STUDYING THE EFFECTS OF GREENING AND DE-PAVING TO REDUCE THE URBAN HEAT ISLAND

Gallia Luca

mat. 806607

Supervisor: *Prof. Federico Agliardi*

Tutor: *Prof. Giovanni Battista Crosta*

Coordinator: *Prof. Giovanni Marco Malusà*

Academic Year 2025/2026

Finanziato dall'Unione europea NextGenerationEU
Ministero dell'Università e della Ricerca
Italiadomani PIANO NAZIONALE DI RIPRESA E RESILIENZA

Table of Contents

Table of Figures

Fig. 66 The maps illustrate the pre-work and post-work scenarios with mature vegetation, where the points at which thermal comfort is measured are visible. The following three graphs illustrate the overall comfort levels in each scenario. The values ranging from -4 to +4 express comfort, with -4 representing the most uncomfortable condition (very uncomfortable) and +4 representing the most comfortable condition (very comfortable) 124

Abstract

The present thesis analyses the Urban Heat Island (UHI) phenomenon in Milan (Italy), with a focus on summertime conditions and thermal exposure in outdoor spaces. Given the variability of this phenomenon at different scales, the study adopts a multiscale, multi-sensor approach. This combines remote sensing, spectral indices, ancillary land cover and land use information, in situ monitoring and numerical modelling. This integration links metropolitan patterns, intra-urban variability and microclimatic conditions experienced at pedestrian height.

At the metropolitan scale, surface UHI is reconstructed using satellite thermal observations, alongside ancillary spatial data and multivariate analysis, to identify recurring spatial structures and their links with impervious surfaces, vegetation and major infrastructure. At the district scale, the heterogeneous and evolving Bicocca district is analysed, revealing stable internal contrasts: surface temperature differences between paved and vegetated areas are significant, while air temperature differences are smaller yet consistent during warm periods. At the site scale, the regeneration phases of Piazza della Scienza (University of Milano-Bicocca) are investigated using field measurements and validated microclimate modelling. This allows consistent comparisons among mitigation scenarios and the assessment of their effects on microclimate.

The results demonstrate that urban heat island effects in Milan are both spatially structured and scale dependent. Metropolitan patterns highlight recurring hotspots and mitigating sectors linked to imperviousness, vegetation, and major urban systems. District analyses reveal stable internal contrasts that translate these signals into site-relevant exposure conditions. At the site scale, the assessment confirms that material changes mainly affect surface temperatures, whereas outdoor comfort is largely shaped by the radiative environment and therefore by shading and vegetation development. Trade-offs can emerge with higher albedo, and vegetation performance depends on realistic management conditions. The thesis aims to support regeneration and design choices by translating multi-scale analyses into criteria for prioritising interventions and for optimising mitigation strategies based on microclimate and thermal comfort assessment.

Chapter 1

1 Introduction

1.1 Context and motivation

According to the World Population Prospects 2024, the global population is expected to continue growing over the coming decades, reaching a peak of around 10.3 billion people in the mid-2080s, after having surpassed 8.2 billion in 2024 (Fig. 1; World Population Prospects, 2024).

This demographic trend is expected to translate into further urban growth. In fact, the 2018 Revision of the World Urbanization Prospects reports that about 55% of the global population lived in urban areas in 2018, and projections indicate that this share will rise to 68% by 2050 (World Urbanization Prospects Revision, 2019). Rapid urbanisation has well-documented implications for local climate. By transforming land cover and surface properties, cities modify radiation exchange, airflow and energy partitioning, generating microclimates that differ from surrounding rural areas (Masson et al., 2020; Oke et al., 2017; Rizwan et al., 2008). One of the most prominent manifestations of this urban climate signal is the Urban Heat Island (UHI), commonly defined as systematically higher temperatures in urban areas than in their rural surroundings (Oke et al., 2017). The UHI has direct consequences for environmental quality and human health, and its relevance has increased alongside climate change and urban densification, motivating a substantial body of research (Santamouris et al., 2015; Zhou et al., 2019).

In light of these considerations, policy frameworks are progressively emphasizing the necessity for urban adaptation strategies that are both effective and context specific. The EU Strategy on Adaptation to Climate Change promotes urban planning that is both informed by climate considerations and prepared for the future. It explicitly warns against 'climate-blind' decisions, emphasising the importance of basing choices on robust evidence of the risks and losses associated with climate change (European Commission, 2021). In a similar direction, European knowledge frameworks emphasize that urban vulnerability is strongly shaped by physical structure and land cover: extensive built-up surfaces and limited green space tend to exacerbate higher urban temperatures and heat-related impacts (EEA, 2023).

In this context, the limitation of heat exposure demands more than generic mitigation targets; it necessitates a fundamental shift in the way cities are planned and retrofitted, with a focus on the environmental regeneration of existing districts and the design of public spaces that mitigate heat stress under both present and future summers. The growing relevance of urban overheating therefore increases the value of approaches that can characterize the UHI and its drivers in a way that is operational for design and regeneration, connecting city-scale diagnostics with the local processes that determine thermal conditions at pedestrian level (UNFCCC, 2016).

Consequently, research focusing on urban overheating and UHI processes is gaining importance. A robust characterization of the phenomenon is therefore essential for identifying the locations and reasons for the occurrence of critical thermal conditions, which is a prerequisite for selecting and prioritizing effective countermeasures. This evidence ultimately supports urban design and planning choices that are oriented towards environmental regeneration and the creation of heat-resilient public spaces.

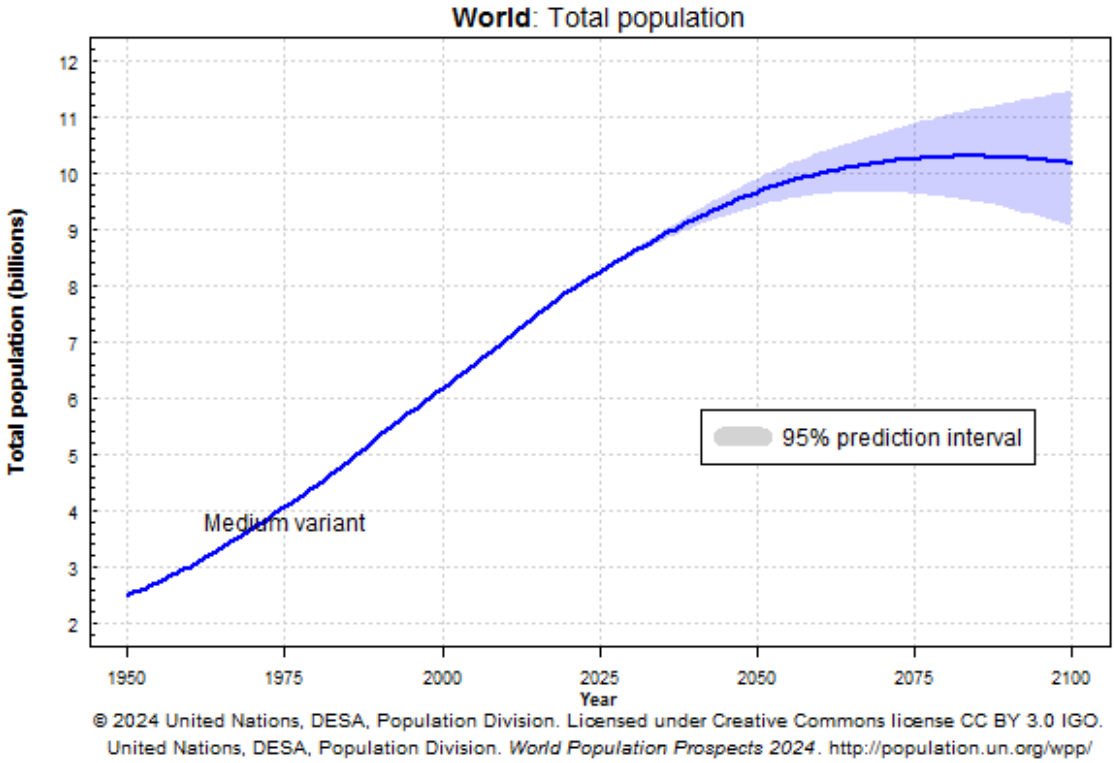

Fig. 1 World total population over the years (World Population Prospects, 2024).

1.2 Scope and approach

The present thesis adopts a multi-scale framework to investigate urban overheating, with the underlying premise that Urban Heat Island can be characterised through multiple observational scales and multiple data sources. Urban thermal conditions are the result of the interaction between land cover and land use patterns, surface properties, urban form, and local meteorological controls. These processes vary in their manifestation across different spatial scales, and as a result, they are captured by different measurement strategies. In this context, the study combines complementary perspectives, ranging from the city-wide characterisation of the Urban Heat Island to detailed, site-specific microclimatic analyses in real urban settings.

At the macroscale, the work focuses on surface thermal patterns across Milan using satellite-derived products, with Land Surface Temperature employed to analyse the spatial structure of urban overheating and to identify broader thermal gradients and hotspots at the metropolitan level. In order to facilitate interpretation, this surface thermal signal is examined in combination with spatial descriptors that represent key urban drivers, including vegetation and built-up intensity proxies and land use and land cover information. This city-scale perspective provides a consistent view that it is essential to place local observations within the wider urban thermal context and to frame prioritisation in terms of areas of potential intervention.

At the microscale, the study adopts a detailed observational approach based on *in situ* monitoring using multiple instruments, aimed at capturing the variability of the urban thermal environment in public spaces. This component investigates how local urban characteristics shape both surface and near surface atmospheric thermal conditions. Numerical analysis and modelling, where applied, are used to support the interpretation of the observations by relating measured patterns to underlying microclimatic mechanisms and by strengthening their relevance for applied decision-making. Overall, this integrated approach connects city-level analysis with local microclimatic processes and provides a coherent basis for defining the case studies and formulating the research questions and objectives.

1.3 Milan as case study and project framework

In line with current international and European climate objectives, cities are increasingly required to develop strategies for overheating adaptation that are both effective and context-specific (UNFCCC, 2016; European Commission, 2018;). Within this broader framework, Milan represents a particularly relevant case study in Italy, given the scale of ongoing urban transformation and the growing attention devoted to heat mitigation in planning and regeneration policies. Milan is currently transforming. This transformation is expressed through regeneration programmes that reshape entire districts and, crucially, their open-space systems, where heat exposure is experienced and can be mitigated. Alongside metropolitan greening policies such as ForestaMi (Comune di Milano, 2019b), which presents large-scale tree planting as a measure to adapt to climate change for the urban area, major redevelopment projects have incorporated significant public green infrastructure within dense urban areas. At a different scale, the municipality has also promoted tactical and incremental transformations through the "Piazze Aperte" public call (Comune di Milano, 2019a), with municipal documentation noting that the initiative attracted over 65 projects, supporting the reconfiguration of streets and small squares into public spaces oriented to pedestrian welfare. Together, these examples motivate the dual focus of the thesis: Milan as a citywide laboratory for urban overheating and urban regeneration as the arena in which design choices that respond to the climate must be tested against the microclimatic mechanisms of a specific site. Furthermore, this thesis is developed within the wider context of MUSA (Multilayered Urban Sustainability Actions), a collaborative initiative involving public and private stakeholders and four main universities of Milan, established to address critical environmental, social, and economic challenges through applied research. Building on this framework, the present work contributes to the understanding of urban overheating in Milan by combining evidence at different spatial scales, with the explicit aim of supporting choices in urban regeneration and climate-oriented design.

1.4 Research questions and objectives

This thesis examines urban overheating in Milan at multiple spatial scales. It treats overheating as a phenomenon that changes in form, intensity and drivers when moving from the metropolitan region to neighbourhoods and, ultimately, to the conditions experienced at

pedestrian height. The work combines observations based on satellite data, district-scale surface characterisation, environmental monitoring and numerical microclimate modelling, validated against measurements. By doing so, it provides a coherent approach that links spatial diagnosis to evidence that can inform regeneration processes and public space design. Within this framework, the thesis pursues three objectives. The first is to describe summertime overheating across the wider metropolitan region, identifying the dominant spatial structures and the relative intensity of the phenomenon, and linking these patterns to urban features, with particular attention to surface types and their spatial distribution. The second objective is to analyse a heterogeneous urban district shaped by long-term transformation and regeneration to interpret how internal contrasts correspond to different thermal responses, using this intermediate level to connect metropolitan patterns with local exposure conditions. The third objective is to develop and apply an evidence-based workflow to assess the influence of materials, shading and vegetation development on local thermal conditions and heat exposure. By integrating observational data with validated modelling, this component enables consistent comparisons among scenarios and provides a quantitative basis for translating microclimate results into practical design suggestions.

1.5 Structure of the Thesis

The structure of this thesis is designed to progress from a general definition of Urban Heat Island to an analysis of Milan on multiple spatial scales. Starting from a macro and mesoscale characterization, the thesis arrives at an application oriented towards regeneration, supported by measurements and modelling.

- Chapter 1 provides a contextual framework, elucidating the motivations and objectives that guided the development of this thesis.
- Chapter 2 provides the conceptual and methodological context. The text introduces the concepts and operational definitions of the Urban Heat Island, outlines the main factors and descriptors used to interpret the phenomenon, and examines observation approaches at different scales. The chapter also summarizes the key impacts and main families of mitigation strategies, emphasizing how scientific evidence can influence planning and design choices.

- Chapter 3 presents a macroscale analysis of Urban Heat Islands in the metropolitan context of Milan (Italy). The study area is described, and the analyses used to interpret surface patterns are integrated with tools such as satellite products associated with auxiliary information on land use and land cover. The chapter presents the results on a macroscale, with a particular focus on the spatial structure of surface warming and the identification of the main thermal patterns in the entire urban region.
- Chapter 4 focuses on mesoscale analysis and characterization of the surface area of interest, treated as a heterogeneous urban system in which different surface types and spatial configurations generate distinct thermal responses. In addition to satellite diagnostics, the chapter presents the integration of data from environmental monitoring distributed in space and time, thereby enabling the interpretation of surface patterns supported and contextualized by in situ observations over time.
- Chapter 5 presents the analysis at microscale. The microclimate case study and the regeneration strategies assessment are discussed. The study site, the monitoring strategy and the simulated scenarios are described, and the results for near-ground conditions and thermal comfort are presented. The chapter discusses how changes in materials and vegetation alter local microclimatic performance, and it evaluates how combined observational and modelling evidence can support design comparisons in real regeneration settings.
- Chapter 6 provides a summary of the main findings, highlighting implications for urban regeneration and design of public space in a climate perspective, and discussing directions for future research.
- Chapter 7 identifies limitations and provides guidance for future research.

Chapter 2

2 UHI description and background

2.1 UHI types and concepts

The phenomenon of urban overheating is commonly explained through the concept of the Urban Heat Island (UHI), which was first systematically observed in London by Howard (1833).

In its broadest and most widely used sense, UHI indicates an urban domain in which temperatures are persistently higher than those recorded in surrounding rural areas when compared under similar meteorological conditions (Oke, 1982). This temperature anomaly is linked to meaningful environmental and societal impacts (Oke et al., 2017; Masson et al., 2020) Therefore, it represents a key entry point for both scientific investigation and applied mitigation planning.

In order to establish a consistent definition of UHI, it is first necessary to comprehend the way cities interact with the lower atmosphere. The Atmospheric Boundary Layer (ABL) constitutes the lowest portion of the troposphere, which is directly influenced by surface forcing (heat, moisture, roughness) on time scales of hours or less (Oke et al., 2017). The ABL is frequently characterised as consisting of a deeper Mixed Layer (ML) and a shallower Surface Layer (SL), with the SL being the component most directly influenced by surface roughness, radiative/thermal exchanges, and the emission of moisture and pollutants. The presence of an urban area has been shown to modify these near-surface processes sufficiently to generate an "urbanised" internal structure within the boundary layer (Oke et al., 2017). This structure is typically referred to as the Urban Boundary Layer (UBL; Fig. 2).

The UBL may assume different configurations depending on synoptic conditions. In conditions of weak regional winds, the city is capable of producing a relatively confined atmospheric "dome" over its area of influence; however, under stronger advection, the urban influence develops from the rural–urban boundary and grows downwind, progressively extending through a larger fraction of the ABL. In such conditions, the urban influence is also associated with the concept of an urban "plume", i.e. a column or trail of warmer and more polluted air transported away from the city (Clarke, 1969; Oke et al., 2017).

Within the lower part of the UBL, and particularly within the SL, further sub-structure becomes relevant for the concepts of heat islands. The Urban Canopy Layer (UCL) is defined as the air volume embedded within the "canopy" of urban elements (buildings and trees). This layer is characterised by strong spatial heterogeneity and strong coupling to local morphology and surface properties (Oke, 1976; Oke et al., 2017). Concurrently, the urban surface and subsurface function as thermal reservoirs, thereby exchanging heat and moisture with the atmosphere above. This phenomenon contributes to the persistence and spatial structure of the UHI signal (Oke et al., 2017).

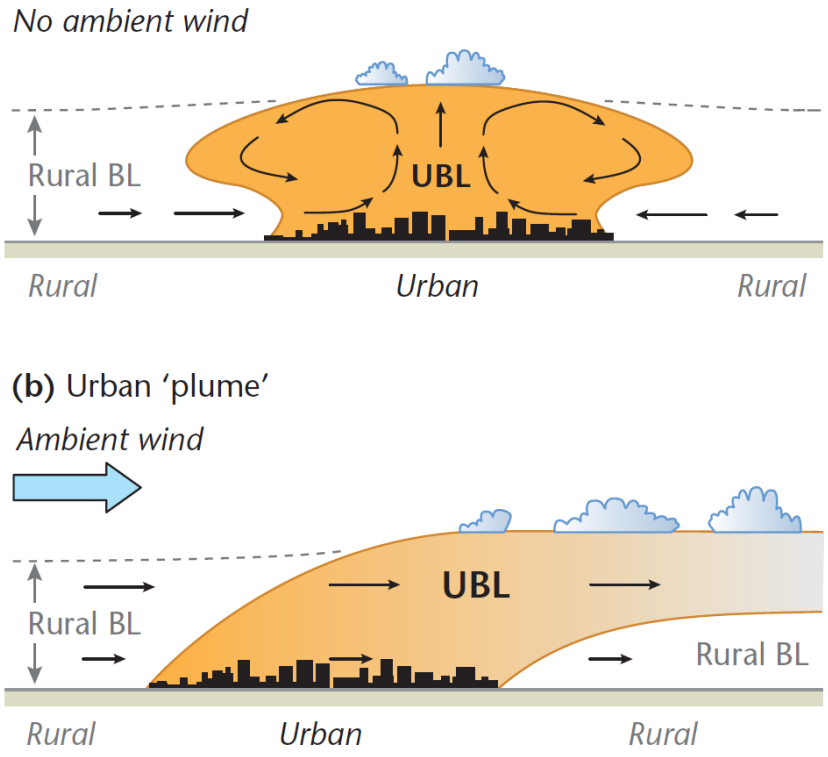

Fig. 2 Typical overall form of boundary later at city scale (Oke et al., 2017).

2.1.1 Urban Heat Island types

It is evident that the UHI phenomenon is not a single phenomenon measured in a unidimensional way, since the city affects both surface temperatures and air temperatures across a variety of atmospheric layers. Within this framework, four UHI "types" are commonly distinguished (Oke, 1995; Oke et al., 2017):

- Sub-surface heat island (UHI_{sub}): the temperature difference between urban and rural subsurface conditions.

- Surface heat island (UHI_{surf} / SUHI): the temperature difference between urban and rural surfaces, typically expressed through surface "skin" temperature.
- Canopy Layer Heat Island (UHI_{UCL} / CLHI): the air temperature difference within the layer below means roof height (the UCL) relative to its rural counterpart.
- Boundary Layer Heat Island (UHI_{UBL} / BLHI): the air temperature difference through the urban-influenced boundary layer above the canopy layer, relative to the surrounding rural atmosphere at comparable elevation.

In the relevant literature, the terminology is occasionally consolidated to emphasise the three most operationally prevalent categories: the Surface Urban Heat Island (SUHI), the Canopy Layer Heat Island (CLHI), and the Boundary Layer Heat Island (BLHI;Voogt and Oke, 2003; Pichierri et al., 2012). In some cases, CLHI and BLHI are grouped under the term Atmospheric UHI (AUHI; Jabbar et al., 2023), in order to distinguish between phenomena related to air temperature and the surface signal. For the purpose of maintaining consistency throughout this thesis, the focus is placed on SUHI and CLHI as the principal reference types, while BLHI and subsurface categories are acknowledged but not treated as a primary analytical target.

2.1.1.1 Canopy Layer Heat Island (CHLI)

CLHI (Fig. 3) is the most directly relevant UHI manifestation for human exposure, as it describes the air temperature experienced by people within streets, squares, and other open public spaces. Its spatial structure is frequently described as a combination of sharp transitions at the rural-urban edge ("cliff"), relatively stable inner-urban gradients ("plateau"), local maxima associated with dense or intensely built-up zones ("peak"), and local minima linked to parks and vegetated areas ("valleys" or "cool islands"). This conceptual structure is advantageous due to its ability to emphasise the non-uniformity of CLHI. The phenomenon of CLHI emerges from the interaction between urban form (e.g. street canyons, building heights, SVF) and atmospheric controls such as wind and cloud cover. These controls regulate mixing and nocturnal radiative cooling (Oke et al., 2017).

It is important to note that CLHI is typically most pronounced under calm, clear conditions, especially at night, when reduced ventilation and enhanced longwave trapping within canyons limit heat loss from the urban fabric (Oke et al., 2017). In conditions characterised

by strong winds or overcast skies, the contrast between urban and rural canopies tends to diminish. This is due to the fact that advection and mixing processes reduce horizontal temperature variations, whilst clouds mitigate net radiative differences.

2.1.1.2 Surface Layer Heat Island (SUHI)

SUHI (Fig. 3) differs both in concept and in observational evidence from CLHI because it refers to surface temperature rather than air temperature. From an energy-balance perspective, SUHI can be interpreted as a disturbance of the surface equilibrium driven by changes in radiative exchange, storage, moisture availability, and anthropogenic heat contributions after natural covers are replaced by impervious materials. It is evident that surfaces respond expeditiously to solar forcing and local shading; therefore, SUHI typically exhibits more pronounced spatial contrasts than CLHI. This is due to the fact that adjacent patches of differing materials or exposure levels can exhibit substantial temperature variations over brief distances. A robust finding in the literature is that SUHI is often stronger during the day than at night, whereas atmospheric UHI (particularly CLHI) is often most evident at night (Voogt and Oke, 2003; Zhou et al., 2019). This observed asymmetry can be attributed to the differential response of urban surfaces to solar radiation, with low moisture availability and high heat storage capacity resulting in significant surface warming during the day. In contrast, vegetated and moist rural surfaces exhibit a greater tendency to allocate energy towards latent heat fluxes (evapotranspiration), thereby limiting surface warming. During nocturnal periods, surface contrasts tend to diminish, but urban materials may remain warmer because of stored heat release and reduced radiative cooling within canyon geometries (Oke et al., 2017).

2.1.1.3 Urban Heat Island intensity (UHII)

Across all types, UHI is generally quantified through an intensity (or magnitude) defined as the temperature difference between a representative urban temperature and a corresponding rural reference (Fig. 3; Oke et al., 2017). The following equation can be used to summarise this concept:

$$\Delta T_{UHI,type} = T_{U,type} - T_{R,type} \quad \textit{Eq. [1]}$$

This variable is indicative of the temperature measured (or estimated) for the urban area for a specific UHI type (surface, canopy layer, or boundary layer). $T_{R,type}$ is representative of the corresponding rural reference under comparable conditions (Oke et al., 2017). The practical implications of this are of crucial significance. The definition of temperature is understood to vary according to the type; that is to say, surface temperature for SUHI, near-surface air temperature for CLHI, and boundary-layer air temperature for BLHI. It is therefore vital that the choice of observations and interpretation remains consistent with the definition (Voogt and Oke, 2003). Finally, given that urban-rural contrasts are contingent on synoptic controls (e.g., wind, cloud cover, seasonality) and the representativeness of the rural reference, the validity of ΔT as an operational metric is contingent on the rigorous selection of comparison domains and measurement context (Oke et al., 2017). This point assumes particular significance in the transition from conceptual definitions to observation strategies, a matter that is addressed in the subsequent sections on drivers, descriptors, and methods.

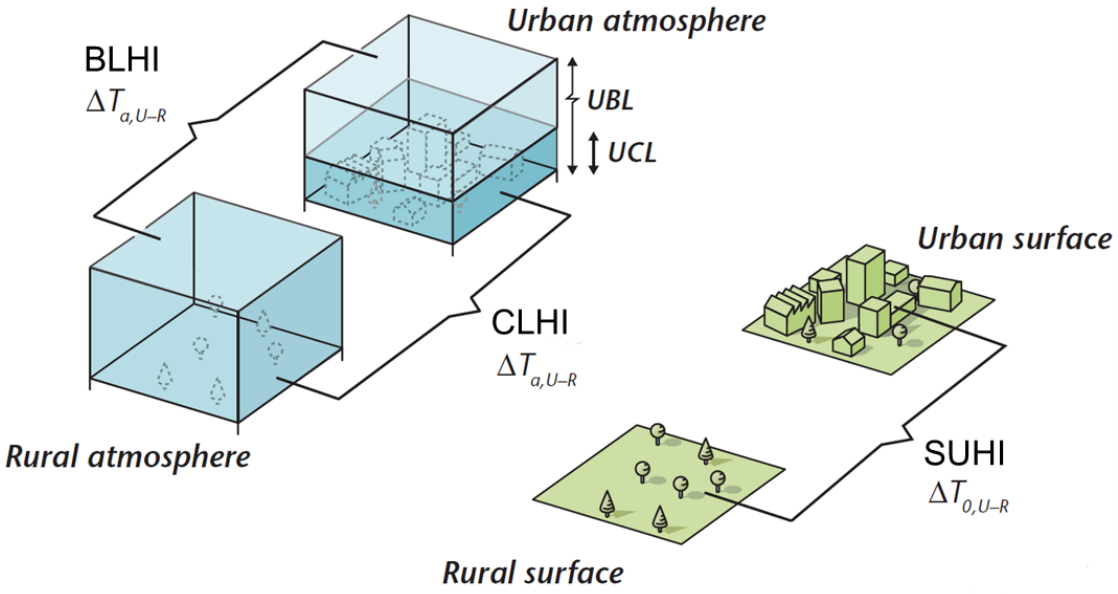

Fig. 3 Visual representation of UHI types and the traditional definition (Oke et al., 2017).

2.1.2 Local Climate Zones (LCZ)

To facilitate consistent comparisons across cities and to link thermal patterns to physically meaningful urban forms, a standardised classification framework based on Local Climate Zone (LCZ) has been developed (Oke et al., 2017). The term LCZs is employed to denote areas distinguished by the presence of relatively uniform surface cover, structural

characteristics, materials and human activity. These LCZs typically span a range from a few hundred metres to several kilometres (Stewart and Oke, 2012; Oke et al., 2017). The primary purpose of defining these LCZs is to serve as proxies for neighbourhood-scale urban environments, thereby ensuring the relevance of the data for temperature studies.

The LCZ scheme is predicated on the grouping of landscapes according to their capacity to modify local surface climate. This is achieved through the clustering of four climatically relevant controls: fabric, land cover, structure and metabolism. These are known to influence wind, temperature and moisture.

In its standard formulation, the classification includes 10 built types (LCZ 1–10) and 7 land-cover types (LCZ A–G). For the built environment, the scheme is associated with typical ranges of measurable properties, including building and impervious plan fractions, canyon aspect ratio and sky view factor, mean height of roughness elements, thermal admittance and anthropogenic heat flux density (Stewart and Oke, 2012; Oke et al., 2017).

A key advantage of LCZs is that they are more suited to urban climate analyses than functional land-use labels, because land-use categories mainly describe urban function (e.g. residential, commercial) rather than the physical site properties that control climatic responses.

Furthermore, the scheme can be implemented using objective criteria derived from aerial photographs, remote sensing and maps, and has been tested against temperature observations in real cities as well as model simulations, reinforcing its role as a common reference framework in UHI-related applications (Oke et al., 2017).

2.2 UHI drivers and descriptors

Given the multitude of causes and interacting processes involved in the Urban Heat Island, it is incorrect to treat UHI as a unitary phenomenon governed by a single driver (Oke et al., 2017). The intensity and spatial structure of UHI emerge from the interaction between city-specific properties and background meteorological controls, acting across scales and through different components of the surface-atmosphere system (Rizwan et al., 2008; Oke et al., 2017; Masson et al., 2020). A widely adopted standpoint is to distinguish between controllable and uncontrollable factors (Fig. 4). The former primarily refers to the urban system itself, namely its materials, geometry, land cover and land use and anthropogenic heat;

whereas the latter include climate and weather conditions such as seasonality, geographic setting, wind, and cloud cover, which modulate incoming radiation and atmospheric mixing (Rizwan et al., 2008; Deilami et al., 2018).

In this thesis, the discussion of drivers is paired with a set of descriptors that can be measured consistently across scales, thereby supporting comparative analysis. Surface thermal conditions are described through Land Surface Temperature (LST). At macro- and mesoscale, the predominant explanatory descriptors are vegetation and built-up proxies (primarily NDVI and NDBI) and land-use/land-cover information, as these variables provide an operational link between physical mechanisms and mappable urban patterns (Zhou et al., 2019).

Furthermore, to obtain a comprehensive description of these links, statistical analysis has been involved. Indeed, statistical analysis constitutes a fundamental pillar in urban climate research, being essential for exploring the complex relationships between land surface temperature and the diverse physical and anthropogenic parameters of cities (Zhou et al., 2019).

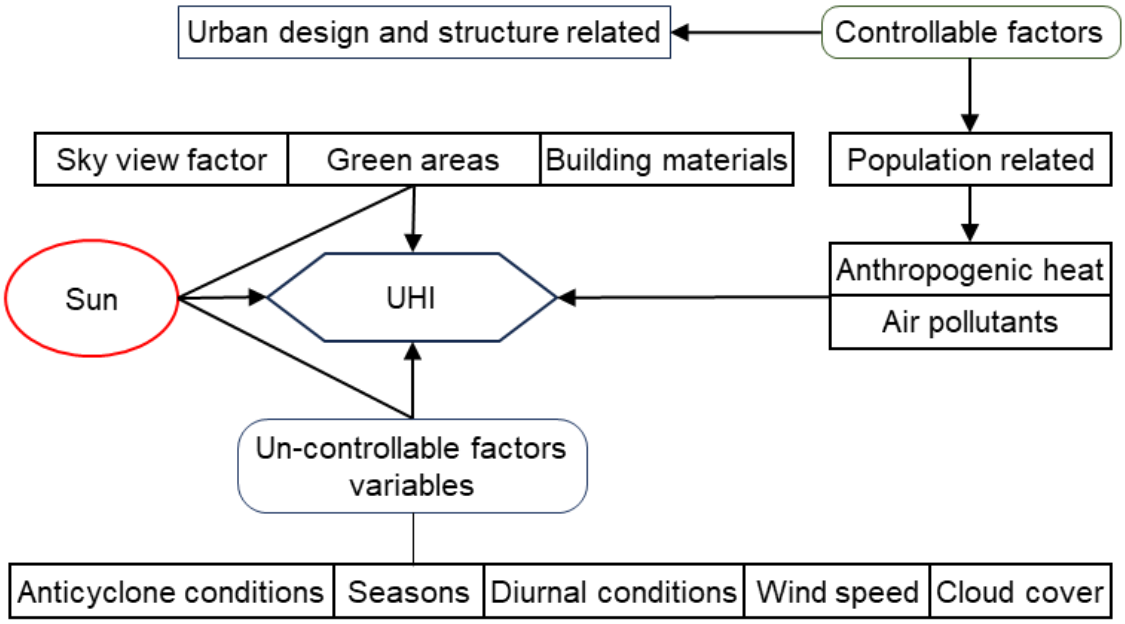

Fig. 4 Schematic view of controllable and uncontrollable factors on UHI (modified by Rizwan et al., 2008)

2.2.1 Surface characteristics: Land cover and land use

Urban growth, as indicated by changes in land cover and land use, is widely acknowledged as a primary cause of UHI. This is due to the replacement of permeable and evaporative

surfaces with mineral and impervious ones, which alters the partitioning of energy at the surface (Oke et al., 1991; Santamouris, 2020). In this context, land-cover patterns, particularly the balance between impervious surfaces and vegetation, are among the key controls on surface temperature fields and, more broadly, on thermal variability related to UHI (Deilami et al., 2018; Zhou et al., 2019). Since the 1970s, research has focused on the role of imperviousness and vegetated fractions as cities expanded with population growth and urbanisation (Oke, 1976; Yuan and Bauer, 2007).

Land use adds an interpretative layer beyond land cover alone because it incorporates the role of human activity and urban functions. In practice, this means that specific functional categories may be associated with recurrent hotspots and distinctive thermal behaviour, which can support planning-oriented interpretation of thermal maps when the aim is not only to describe patterns but also to relate them to urban functions. A multitude of studies have examined relationships between UHI intensity and socio-economic factors (including population and economic activity). However, the role of urban size remains debated: some studies report strong associations between city size and UHI intensity, whereas others do not observe consistent relationships. Overall, city size may explain part of the variability in UHI magnitude but is not generally regarded as a primary physical driver compared to surface composition and meteorological factors (Deilami et al., 2018; Zhou et al., 2019).

2.2.2 Material properties and anthropogenic heat

The thermal response of urban areas depends on how surfaces absorb, store, and release energy. The thermal properties of building and paving materials, anthropogenic heat releases, canyon radiative geometry, and the reduction of evaporative surfaces are consistently highlighted as key mechanisms contributing to UHI formation (Oke et al., 1991; Santamouris, 2020). From a physical standpoint, incoming solar radiation is absorbed, transmitted, and reflected by materials; the relative importance of these processes depends on intrinsic properties. Storage and heat transfer are governed by thermal conductivity and volumetric heat capacity, while radiative behaviour is commonly described through albedo (reflectance) and emissivity (efficiency in emitting longwave radiation; (Giorio and Paparella, 2023). These properties influence heating and cooling rates and contribute to temperature contrasts between adjacent urban surfaces under similar meteorological forcing.

2.2.3 Urban geometry and morphology

Urban geometry, defined as the configuration and arrangement of buildings, streets, and open spaces, affects radiative exposure, wind circulation, and convective and radiative exchanges (Fig. 5; (Andreou, 2014). A common representation in the literature characterises urban geometry through three descriptors: sky view factor (SVF), aspect ratio (H/W), and street-canyon orientation (Han et al., 2023). SVF measures the fraction of the sky hemisphere visible from a given point; aspect ratio describes the degree of enclosure of street canyons; and canyon orientation modulates the timing and intensity of direct solar exposure and, in some contexts, ventilation pathways.

Within the framework of this thesis, these morphological descriptors are acknowledged as important controls of local heterogeneity, particularly relevant for canopy-layer processes (Oke et al., 2017; Han et al., 2023). However, they are treated as contextual drivers rather than the main comparative descriptors at macro- and mesoscale, where land cover/land use and spectral proxies remain the primary explanatory layer here.

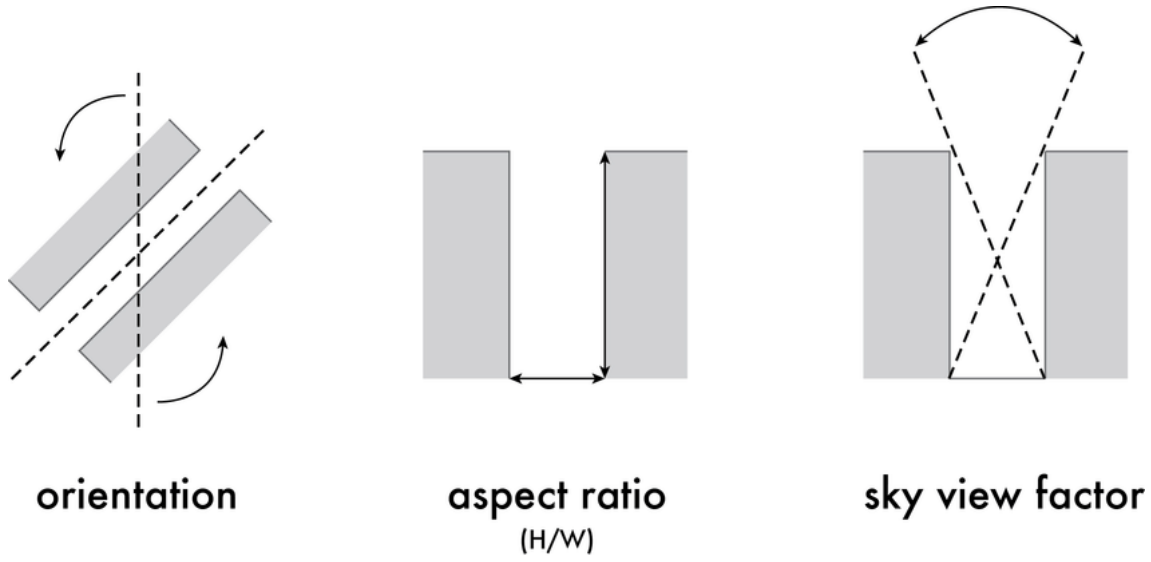

Fig. 5 Urban geometries variables affecting UHI (Boeters et al., 2012)

2.3 Spatial scales, observation methods and emblematic applications

The study of the UHI phenomenon requires a multiscale approach, given the significant variations in thermal dynamics across ranges from the micro to the macro-scale. These units can be categorised by meteorological scale, ranging from individual surface elements and street canyons to entire cities (Lietzke et al., 2015; Kim and Brown, 2021). Furthermore, as Masson et al. (2020) have highlighted, the selection of the investigation scale is also a determining factor for the data collection methods.

The present thesis employs a nomenclature that delineates between macroscale, mesoscale and microscale, with the former referring to urban and regional contexts, the second to district contexts, and the latter to square and single building contexts (Fig. 6).

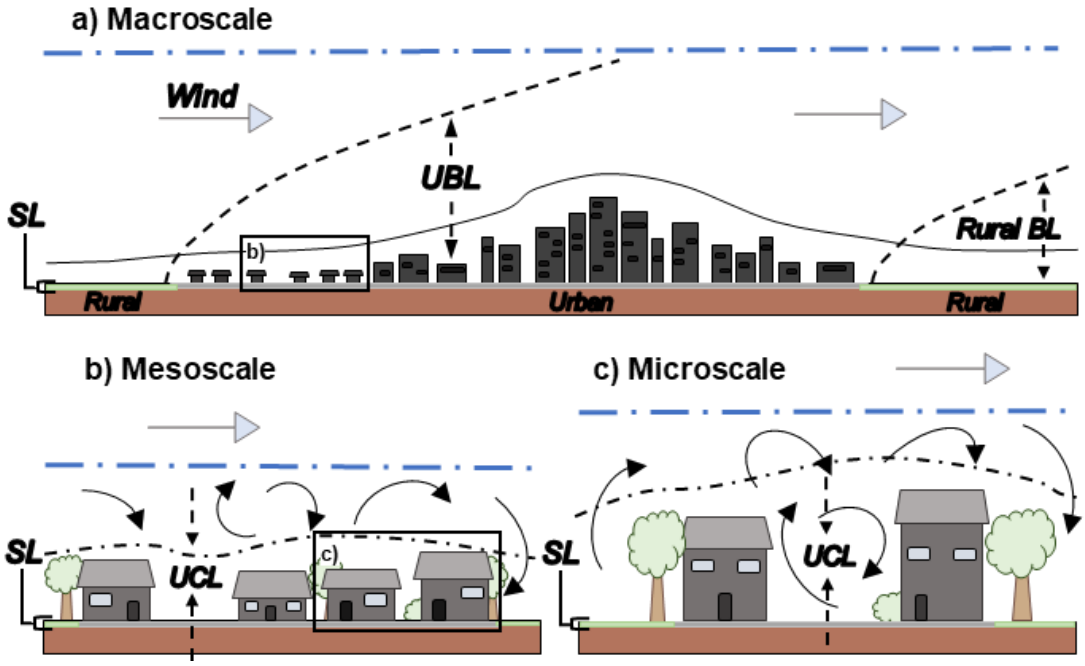

Fig. 6 General representation of different spatial scales for UHI study. This thesis uses different terms for different levels of measurement namely Macroscale a), Mesoscale b) and Microscale c). UBL = Urban Boundary Layer, UCL = Urban Canopy Layer and SL = Surface Layer

2.3.1 Macro- and mesoscale

At the macroscale (Fig. 6a), UHI investigations typically rely on spatially continuous diagnostics capable of representing the city as a system. This level of analysis is strongly associated with the Surface Urban Heat Island phenomenon, because satellite thermal remote

sensing provides broad spatial coverage and repeated observations of LST thus supporting consistent mapping of surface thermal patterns and their seasonal or interannual variability (Voogt and Oke, 2003; Zhou et al., 2019). Landsat sensors are the most prevalent in SUHI applications, followed by MODIS, reflecting the common trade-off between spatial detail and revisit frequency across thermal missions (Zhou et al., 2019). In addition to the availability of data, the macroscale SUHI literature emphasises two recurring observational properties: it has been demonstrated that daytime SUHI intensities frequently exceed nighttime values, and directional and anisotropic effects can influence apparent SUHI magnitude (Zhou et al., 2019).

At the mesoscale (Fig. 6b), the focus shifts from city-wide pattern recognition to the thermal characterisation of heterogeneous districts or sub-regions within the urban fabric. In this context, the objective is typically to quantify intra-urban variability through spatial sampling strategies. This intermediate scale is frequently employed to translate synoptic thermal evidence into spatial units that are more aligned with planning interpretation, while maintaining the analysis's anchoring to comparable surface descriptors derived from remote sensing and spatial urban datasets (Voogt and Oke, 2003; Zhou et al., 2019).

Urban-rural areas comparisons provide a clear example of how macroscale SUHI magnitude varies with background climate, ecological context and surface composition. Utilising the MODIS satellite in conjunction with impervious-surface stratification for 38 major U.S. cities, Imhoff et al. (2010) assert that the most pronounced average summer daytime SUHI amplitudes occur in forested biomes (7 to 9°C). In contrast, lower-biomass contexts exhibit more moderate amplitudes (4 to 6°C). For all cities combined, the impervious surface area is reported as a dominant explanatory factor, accounting for approximately 70% of the variance in LST. The same study reports an annual average urban and rural difference of about 2.9°C and a strong seasonal asymmetry. Within a forest sample, a marked increase in summer daytime SUHI was reported to occur in correlation with city size (1.5°C for urban areas <10 km² vs 10°C for urban areas >1000 km²; Imhoff et al., 2010).

A further methodological result at macro scale is that estimates of SUHI and inferred trends can be highly sensitive to the definition of the non-urban reference. In a comparison of seven non-urban reference delineation methods across 281 Chinese cities, Liu et al. (2023) report that 74% of cities show discrepant SUHII values across methods; the mean SUHII can shift

from about 4.9°C to about 2.7°C. The same study reports that 23 cities (8%) flip the sign of the surface thermal island depending on reference selection, and that trend estimates are also affected: A significant proportion of cities (41%) demonstrate discrepancies in their significant trends across the various methods, while a further 21% exhibit reversals in the direction of statistically significant trends (Liu et al., 2023).

The LCZ classification approaches provide an operational bridge between mesoscale structure and macroscale comparability. In a multi-city LCZ application over 21 Chinese cities, SUHI intensity is reported to differ systematically across LCZ classes, with the largest values being associated with dense built-up typologies, reaching 5.5 to 8.5°C (Hu et al., 2025). Within the same theoretical framework, the relative importance of drivers varies across cities. Impervious surface-related indicators contribute on the order of 13% to 45%, and the single most influential factor differs among cities (Hu et al., 2025).

2.3.2 Microscale

At the microscale (Fig. 6c), investigations of UHI address the thermal environment at the level of streets, blocks and public spaces, where temperatures are shaped by local morphology, shading patterns, surface materials and ventilation constraints. At this scale, the most salient atmospheric manifestation is the Canopy Layer Heat Island, given that near-surface air temperature within the urban canopy is directly linked to pedestrian exposure and to the spatial heterogeneity induced by urban form (Oke et al., 2017). Consequently, microscale observation strategies place strong emphasis on *in-situ* monitoring, typically through fixed sensors deployed at representative points and through mobile transects (mounted on bicycles or vehicles) that allow high spatial coverage at a height of pedestrian competence (Oke et al., 2017; Pena Acosta et al., 2023). Whilst mobile approaches can be powerful for capturing small scale variability, they also require careful protocols because factors such as speed and sampling frequency can affect data quality and interpretability (Makido et al., 2016; Vieira Zezzo et al., 2023).

A recurring empirical finding is that microscale CLHI patterns can vary markedly over short distances, especially in dense and morphologically complex settings. For instance, in a Hong Kong pocket-park campaign based on 195 measurement points, the UHI (defined against a rural reference station) ranged from 2.6°C to 4.2°C across points and times; the mean daytime

intensity was low (0.1°C), whereas the mean early-night intensity was much higher (2.4°C) and increased from 1.7°C (7 PM) to 3.1°C (9 PM) consistent with nocturnal radiative trapping and reduced ventilation in deep urban canyons (Lin et al., 2017).

Microscale studies also frequently integrate surface observations using InfraRed Thermography (IRT), since surface temperatures provide direct evidence of material behaviour, shading effects, and local heat-storage dynamics. This information is complementary to air-temperature monitoring and facilitates the interpretation of CLHI patterns (Voogt and Oke, 2003; Kim and Brown, 2021). This is of pertinence when the objective is to establish a correlation between air temperature exposure and hot surfaces that can drive local radiative loads. In microscale applications, interventions targeting surface properties can yield strong surface temperature responses, especially in highly exposed courtyards or open paved areas. For instance, cool paving and material strategies have been associated with decreases of surface temperature up to 11°C, with peak reductions reported around 16.3°C in the most exposed courtyard locations, while reductions in adjacent street-canyon points can be substantially smaller, reflecting the modulation by geometry and shading (Makropoulou, 2017).

Since microclimatic processes are determined by the coupled behaviour of radiation, turbulence, and surface energy exchange, numerical simulations are extensively utilised to interpret observations and evaluate different design scenarios. The extant literature typically differentiates between mesoscale urban climate models and high-resolution microclimate models (Fig. 7). The latter represents local interactions within complex geometries and are utilised to assess the potential effects of interventions on thermal conditions and comfort (Lobaccaro et al., 2021; Vieira Zezzo et al., 2023). A fundamental methodological consideration is that the added value of modelling at the microscale is contingent on the existence of observational evidence for calibration and validation. The range of reported performance is extensive, with developers and validation studies noting that deviations of a few degrees can be commonplace in practice (2 to 4°C). Conversely, well-constrained case studies have been observed to achieve substantially smaller temperature errors (Makropoulou, 2017).

In addition to air temperature, physically based urban energy-modelling frameworks underscore the importance of validating the radiative and storage terms that govern surface–

air coupling. In the study by Yang et al. (2013), energy-model evaluation was employed to determine the average (and maximum) hourly difference between predicted and measured ground surface temperature. The results showed that this difference was approximately 0.5 °C for bare soil and asphalt in experimental validation.

Field- and model-based microscale studies are frequently utilised to quantify the magnitude of thermal changes that are associated with specific interventions, and which can be considered as actionable. In an urban setting, a case study of a street block revealed that integrating vegetation and surface material changing resulted in pedestrian level air temperature reductions ranging from approximately 0.5–1.0°C in street canyons to 1.2–1.6°C in courtyards. Concurrently, relative humidity increased by up to approximately 4.3% in the most sheltered courtyard, indicating that the most significant benefits can be highly dependent on the specific spatial conditions (Makropoulou, 2017).

Complementary evidence from cool-pavement experiments demonstrates comparable surface responses: cool paving has been associated with mean surface-temperature decreases of approximately 8°C for asphalt and a few degrees for concrete in a monitored application (Kyriakodis and Santamouris, 2018).

Concurrently, modelling studies underscore the context-dependency of outcomes, emphasising that single level modifications may not translate into uniform near-surface cooling across diverse land-use categories. For instance, an assessment revealed that increasing green space diminished the ambient temperature by approximately 0.49°C, while increasing surface reflectivity was associated with ambient-temperature increments in multiple land-use categories. This underscores the necessity for coupled design and evaluation, as opposed to the assumption of universally monotonic effects (Song and Park, 2015).

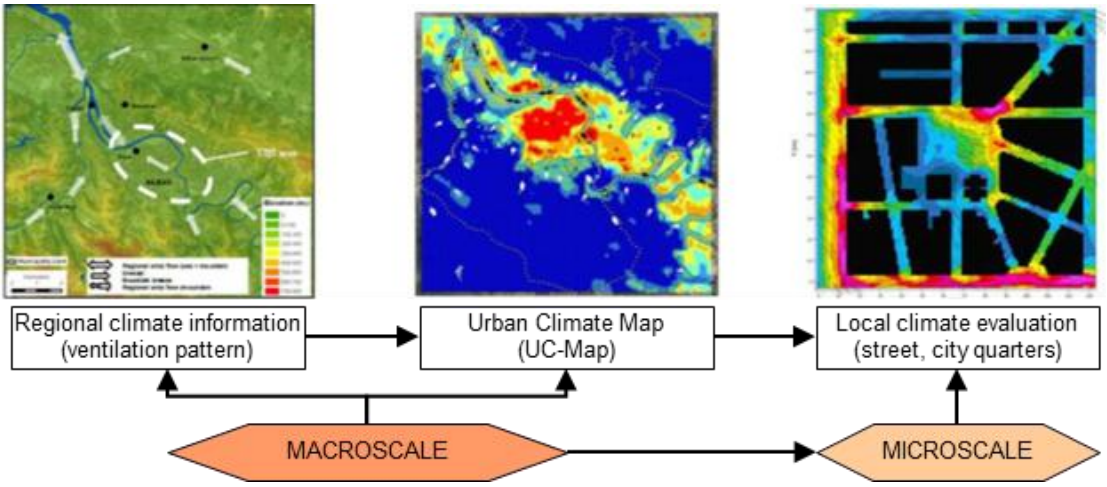

Fig. 7 Multiscale model-based approach for urban climate evaluation (modified by Lobaccaro et al., 2021).

2.4 Impacts

Urban overheating and UHI affect meteorology, infrastructure, and public health through interacting feedback, for instance, when higher temperatures increase cooling demand and can indirectly amplify emissions and local pollution. These impacts are expected to intensify under a warming climate and in association with more frequent or severe extreme summer events such as heat waves (Seto et al., 2012; Stocker, 2014; Santamouris, 2020; Kim and Brown, 2021).

2.4.1 Impacts on climate, local meteorology and the urban water system

Evidence indicates that urbanisation and processes related to UHI can influence local climate trends, although attribution remains complex and context dependent (Masson et al., 2020). For instance, considering rainfall in Rome, an urban versus rural contrast has been reported with annual averages of +70 mm in precipitation and +0.9°C in air temperature at the urban site relative to the rural reference (Salvati et al., 2019). At a season time scales, UHI has been shown to interact with extreme summer conditions and to contribute to heat-wave exposure (Luber and McGeehin, 2008; Santamouris, 2020; Kim and Brown, 2021).

Urban overheating also affects water systems through thermal pollution: warm stormwater runoff can induce rapid temperature shifts in receiving waters, creating stress conditions for aquatic life. Brook trout, for instance, have been reported to be sensitive to sudden changes, with an increase exceeding 2°C within 24 hours potentially inducing thermal stress or shock

(Jabbar et al., 2023). In addition, interactions between UHI and local circulations can contribute to cloud formation and thunderstorms (Vemado and Pereira Filho, 2016; Yamato et al., 2017). When coupled with the high imperviousness of urban surfaces, such dynamics can exacerbate flood impacts during intense rainfall events (Masson et al., 2020).

2.4.2 Impacts on energy demand and urban services

Rising urban temperatures are strongly associated with increased demand for cooling (Fig. 8; Santamouris, 2015, 2020). Reported estimates indicate that peak cooling load may increase by 0.5% to 8.5% for each 1°C rise in outdoor temperature, depending on context and building stock (Guattari et al., 2018). At the buildings level, UHI has been linked to an average of 12% increase in cooling energy demand across building types. The magnitude of the associated "energy penalty" is reported to vary widely worldwide (0.1 to 20 kWh/m²/year/°C), with an average of about 2.3 kWh/m²/year/°C (Santamouris, 2020).

Evidence in specific city also highlights the relevance of intra-urban variability for energy assessments. In Rome, Guattari et al. (2018) showed that using urban versus rural meteorological data can yield differences in estimated cooling demand up to +66.8%, with mean values around +30% for cooling demand and 11% for heating demand (Guattari et al., 2018). This supports the planning value of spatially explicit overheating diagnostics in contexts where thermal loads are unevenly distributed within the city.

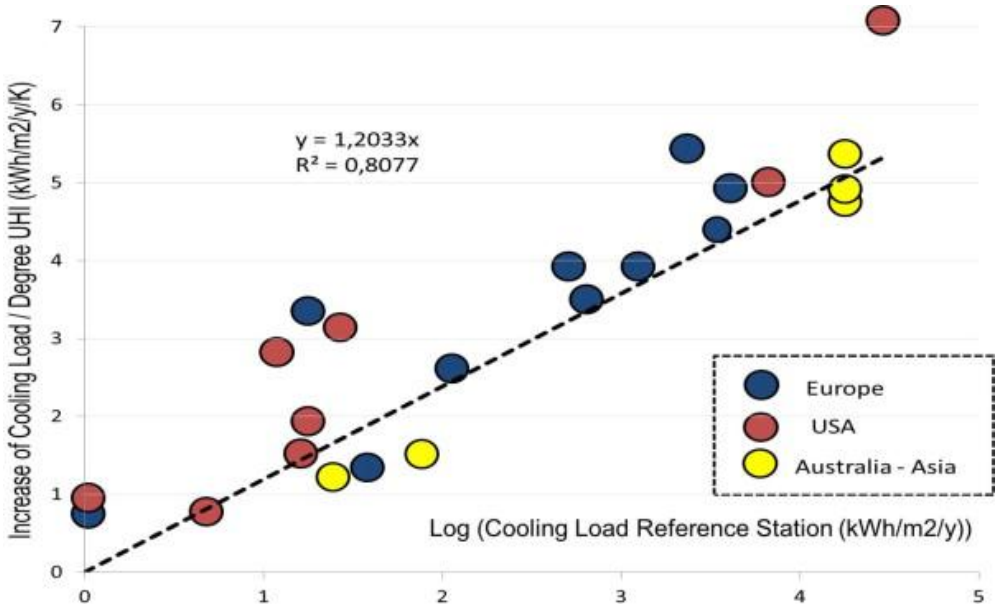

Fig. 8 The relationship between how much cooling a building needs and how much extra cooling is needed due to the heat island effect (Santamouris, 2014b).

2.4.3 Impacts on air quality

Urban overheating influences air quality via two distinct mechanisms. Firstly, the chemical composition of the atmosphere is affected. Secondly, energy-related emissions also impact air quality. The relationship between tropospheric ozone and high temperatures is well-documented; increased photochemical reaction rates under warm and sunny conditions have been shown to be a contributing factor (Jenkin and Clemitshaw, 2000; Sarrat et al., 2006). This linkage between temperature and ozone is also synthesised in the broader UHI literature as a recurring pathway through which heat amplifies exposure to secondary pollutants (Santamouris, 2020). During periods of extreme heat, there have been reports of increased ozone levels, with a documented 20% increase observed in U.S. cities (Diem et al., 2017). In Athens, higher temperatures have been associated with an 18% increase in the number of days exceeding the ozone threshold (Stathopoulou et al., 2008). Projections have also suggested substantial future increases in high-ozone levels, including estimated rises of 50% and 80% by 2050 and 2080 in Canada (Cheng et al., 2010) and a projected 400% rise in high-ozone levels in Arizona (Wise, 2008).

Concurrently, elevated cooling demand during periods of high temperature can increase emissions from power generation and contribute to higher concentrations of pollutants such as SO_2, NOx, and particulate matter, contingent on the energy mix (Meier et al., 2017). The interplay between energy demand and emissions, driven by climate change, is also examined as systemic feedback in UHI impact assessments (Santamouris, 2020). In the eastern United States, during the summer seasons of 2007 to 2012, Meier et al. (2017) reported that a 4% increase in electricity generation was associated with a 3% rise in air pollutants. Under a projected warming of 1 to 5°C, the estimated increases in SO_2 and NOx were approximately 16% and 18%, respectively (Meier et al., 2017).

2.4.4 Impacts on thermal comfort and health

A significant consequence of urban overheating is the deterioration of outdoor thermal comfort, which directly impacts the usability of streets, squares, and semi-open spaces. It is important to note the distinction between thermal comfort and thermal sensation. Thermal comfort reflects an overall thermoregulatory and perceptual state (i.e. whether the individual experiences it as comfortable or uncomfortable), rather than a hot or cold sensory response.

In contrast, thermal sensation indicates how the thermal condition is perceived by the individual, typically along a continuum from cold to hot. Thus, thermal sensation reflects the perceived thermal state, whereas thermal comfort expresses the overall subjective appraisal of that condition (Pantavou et al., 2011). As such, it is commonly assessed through biometeorological indices that combine air temperature with radiation, humidity, and wind (Pantavou et al., 2011).

A review of microscale studies consistently indicates that radiation exposure, frequently represented by mean radiant temperature (MRT), exerts a substantial influence on perceived heat stress. This suggests that factors such as geometry (i.e. shading), vegetation, and surface characteristics can generate significant disparities in comfort levels, even when there are only minor fluctuations in air temperature (Oke et al., 2017;Mutani et al., 2022). In Turin, for instance, a comparison of two courtyard geometries typical of the city (H/W = 0.7 vs 1.2) yielded a difference of approximately 15°C in PET, attributed to the stronger shading in the deeper canyon; the same analysis also highlights material effects, with greener surfaces yielding lower PET than Scenario-based microclimate assessments demonstrate comparable radiation-driven effects (Mutani et al., 2022). In the study of (Piselli et al., 2018), an increase in pavement albedo (to 0.8) resulted in a reduction of surface temperature by up to 10°C at 2 PM., while the addition of trees led to a decrease in air temperature of up to 0.9°C at midday. Significantly, the vegetation scenarios reduced MRT by more than 20°C in areas with a high presence of greenery, which is the type of change that most directly translates into improved pedestrian comfort (Piselli et al., 2018).

Comfort analyses consistently demonstrate that variations in shading levels can result in a shift in the frequency with which a location falls within a PET range considerable comfortable. One study reports that, during summer, a location receiving more shade spent approximately 50% of daytime within PET 26 to 30°C, whereas a location receiving only a little shade remained below 20%. Unshaded sites also exhibited notably high cumulative discomfort loads during summer asphalt under the same day (Mutani et al., 2022).

The impact of urban heating on the health of the population is a significant concern, given its correlation with mortality (Fig. 9). A body of epidemiological evidence has been published which suggests a link between exposure to elevated temperatures and an increased risk of adverse cardiovascular and respiratory outcomes. The evidence indicates that this link is

particularly pronounced among susceptible groups, such as older adults and individuals with pre-existing conditions (Anderson and Bell, 2011). Furthermore, severe or prolonged heat exposure has been demonstrated to be associated with an increased risk of heat stroke and excess mortality (Heaviside et al., 2017). Because vulnerability is shaped by local acclimatisation and baseline climate, many studies identify threshold temperatures above which mortality and morbidity increase. For the Mediterranean region, a threshold around 29.4°C has been reported, above which mortality increases by approximately 3.2% (Baccini et al., 2008). Green and blue infrastructure has been demonstrated to function as both mitigation mechanisms and modifiers of the health risks associated with heat. This integration of thermal diagnostics, land cover descriptors, and mitigation planning within public health and urban regeneration frameworks is a significant development (Stone et al., 2010; Kim et al., 2017; Schinasi et al., 2018; Kim and Brown, 2021).

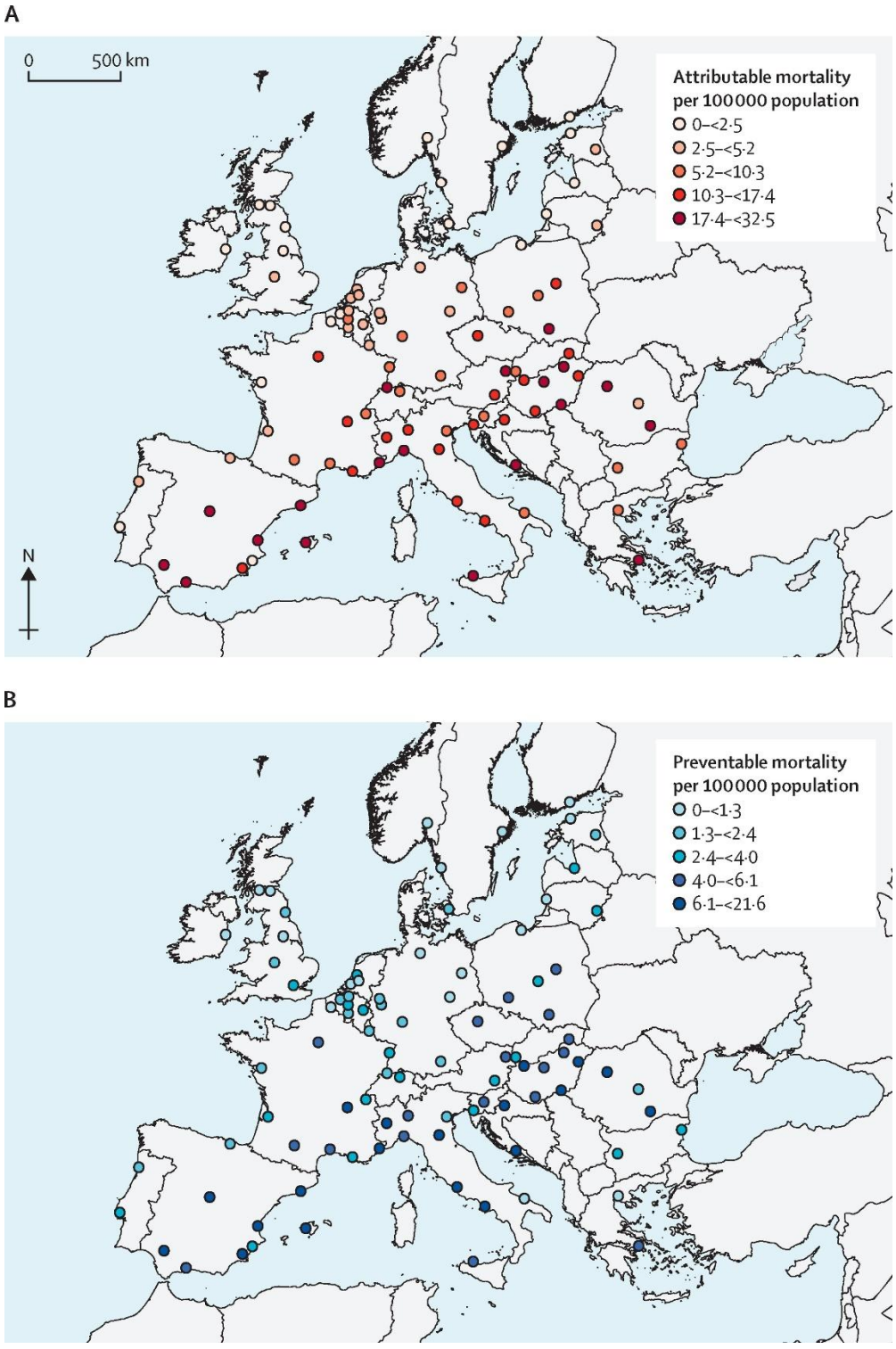

Fig. 9 Average number of deaths caused by the UHI effect a) and the average number of deaths that could have been prevented by increasing tree coverage to 30% b) per 100000 residents in European cities (Iungman et al., 2023).

2.5 Mitigation strategies

Urban heat mitigation is defined as a range of interventions that aim to reduce the net accumulation of heat in urban systems. These interventions act on radiative gains, heat storage, and the pathways through which heat is released to the atmosphere (Fig. 10). The overarching goal of these interventions is to lower surface and near-surface air temperatures and limit heat exposure. In practice, measures are commonly organised into three broad categories: nature-based solutions (e.g. vegetation and water-related interventions), material-based strategies (notably cool roofs and cool pavements), and urban-form strategies that modify radiative exposure and ventilation patterns (Han et al., 2023). The evaluation of their performance typically involves a combination of field measurements and numerical simulations. The extant literature generally emphasises that the most significant and durable benefits are achieved when measures are implemented in combination rather than as isolated actions (Arrau and Peña, 2010; Deilami et al., 2018; Han et al., 2023).

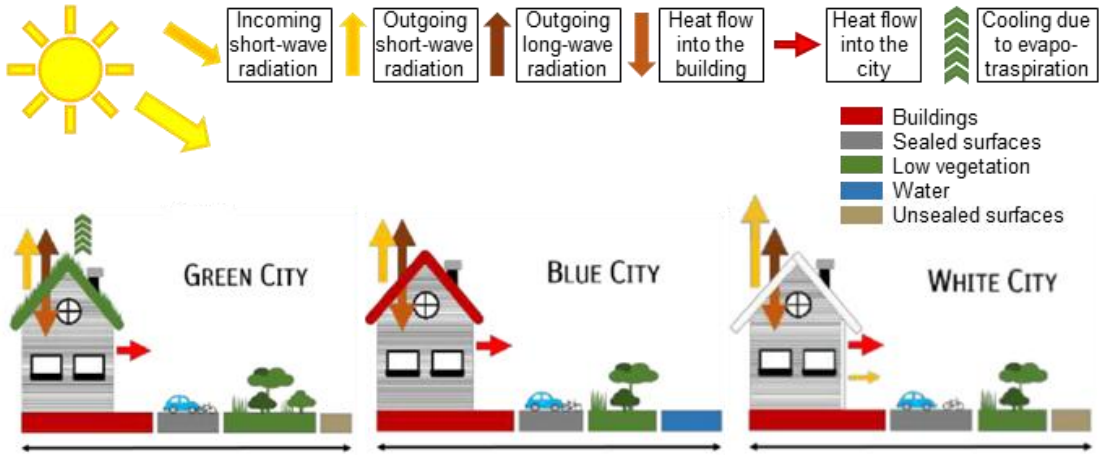

Fig. 10 Illustration of different urban heat mitigation strategies (World Bank, 2020).

2.5.1 Nature-based solutions

Nature-based solutions mitigate urban overheating primarily through shading and evapotranspiration. Reported average air temperature reductions using greening and blue typologies are 2.05°C, 1.75°C, 1.4°C, 1.92°C and 2.58°C for parks, street trees, green walls, green roofs and water bodies respectively (Han et al., 2023). For instance, 1°C decrease in urban temperatures has also been associated with achieving at least 16% tree cover (Marando et al., 2022; Ciacci et al., 2023;).

At neighbourhood scale, parks and green spaces can generate Park Cool Island effects, with substantial temperature differences relative to surrounding built-up areas; even smaller gardens have been reported to exhibit temperature variations of about 7°C compared to adjacent zones (Oliveira et al., 2011). Reported cooling effects generally decay with increasing distance from the park boundary, which is relevant when interpreting how far benefits extend into surrounding streets (Han et al., 2023).

Street trees extend greening benefits along circulation corridors by combining radiative cooling (shade) with latent-heat exchange through evapotranspiration. Reported reductions in air temperature along paved roads range from 0.5°C to 5.6°C. Reductions in building cooling energy demand, reported at around 10% in the cited evidence, are also discussed as co-benefits of street tree deployment (Sawka et al., 2013; Vailshery et al., 2013; Wang et al., 2015; Han et al., 2023).

Greening integrated in buildings, can additionally target vertical and roof surfaces. For green walls (living walls and green façades; Fig. 11), Mediterranean evidence reports surface temperature reductions of 20 to 25°C and near the wall air temperature differences of 1.2°C between greened and conventional façades (Cheng et al., 2010; Mazzali et al., 2013). Green roofs have been associated with 3°C air temperature reductions in U.S. city simulations and a broader reported range of 0.3 to 3°C across studies (Ciacci et al., 2023; Santamouris, 2014b).

Finally, blue infrastructure contributes to cooling through high heat capacity and evaporation. Reported evidence includes a mean decrease of 19°C in surface temperature for water bodies and 2.58°C overall reductions of air temperature, with larger reductions reported for Mediterranean contexts (4.68°C; (Santamouris, 2014a). Urban ponds may reduce air temperature above the water and in surrounding areas, up to about 1.2°C (Manteghi et al., 2015; Taleghani and Berardi, 2018).

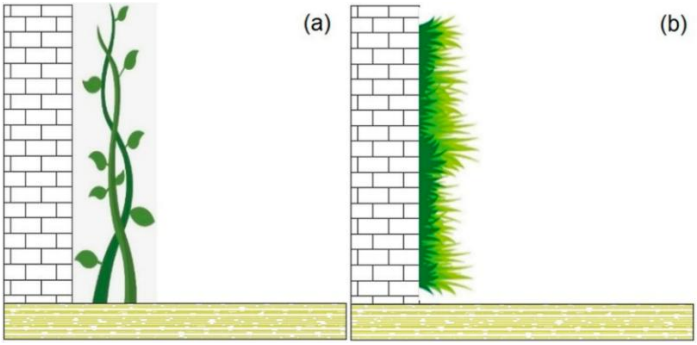

Fig. 11 Example of green facade a) and living wall b) (Han et al., 2023)

2.5.2 Material-based strategies

Mitigation strategies, based on materials properties, focus on the radiative and thermal behaviour of urban surfaces. These strategies primarily act by increasing albedo, thereby reducing the amount of incoming solar energy absorbed and stored. In the context of monitored applications, the temperature differential between the surface and the atmosphere has been documented to reach 35°C in the case of black asphalt, while white asphalt has been shown to be 7°C cooler (Kalinkat and Rall, 2015). At neighbourhood scale, simulations in Padua reported a maximum daily surface temperature decrease of 15°C, corresponding to about a 2°C reduction in air temperature (Giorio and Paparella, 2023). At larger scales, the application of reflective asphalt over 37000 m² has been documented to reduce surface temperatures by up to 11°C and air temperatures by up to 1.5°C (Kyriakodis and Santamouris, 2018).

Regarding cool roofs, where conventional roof surfaces can reach 50 to 60°C, an increase of 0.1 in roof albedo has been associated with an approximately 0.3°C reduction in temperature (Santamouris, 2013, 2014a). In addition to local effects, a large-scale scenario has been documented, which posits that enhancing roof reflectivity by 0.25 and pavement reflectivity by 0.15 would elevate urban albedo to a sufficient extent to potentially curtail global temperatures by approximately 2°C over the ensuing two decades and 3°C over the subsequent two centuries. This scenario is accompanied by estimated annual energy-demand reductions of up to 10 TWh, peak electricity reductions of up to 7 GW, and annual savings approximating $750 million (Akbari and Konopacki, 2005).

The extant literature also highlights the relevant implications that should be considered when focusing on these solutions. Optical degradation due to soiling can be rapid; in the cited study,

reflectivity decreased from 0.33 to 0.17 within six months. Higher reflectivity can also increase shortwave exposure for pedestrians, especially in confined street canyons where multiple reflections occur. In addition, wintertime penalties may occur in contexts where increased reflectance contributes to higher heating demand (Kyriakodis and Santamouris, 2018).

2.5.3 Building layout and geometry

The urban form influences overheating by regulating solar access, longwave heat loss, and ventilation within the urban canopy, so that basic street canyon descriptors (e.g., aspect ratio H/W and orientation) can shift both daytime loading and nocturnal cooling (Oke et al., 2017; Han et al., 2023).

Specifically, the evidence synthesised in Oke et al. (2017) suggests that increasing H/W typically enhances daytime shading but concurrently restricts nighttime radiative heat loss and reduces ventilation (Fig. 12). On this basis, Oke (1988) proposed an intermediate H/W range of 0.4 to 0.6 as a compromise between solar access, wind shelter, and street level dispersion. Measures related to geometry, frequently imply interventions at the level of street layout and built structure; consequently, they are typically framed as guidance for new developments or major regeneration rather than for small, incremental retrofits (Oke et al., 2017). The orientation of the street-canyon provides a clear example of exposure effects: It has been observed that E–W oriented canyons exhibit temperatures that are approximately 3°C higher than those experienced by N–S canyons under high solar irradiance conditions. These differences are attributed to variations in the timing and duration of direct solar input (Chatzidimitriou and Yannas, 2015).

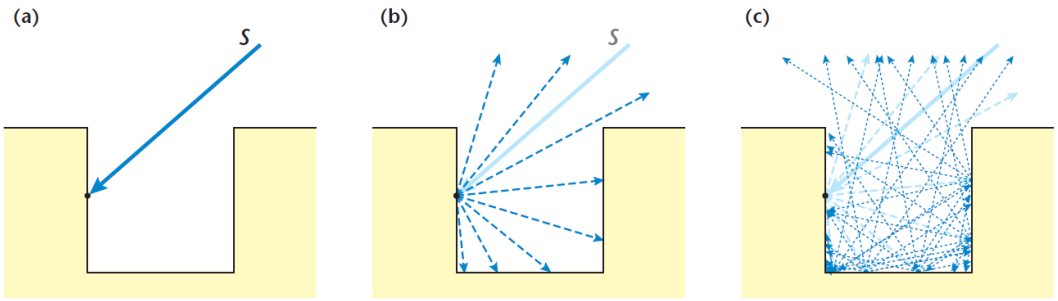

Fig. 12 Impact of the geometric configuration of an urban canyon on radiation exchanges (2D simplification. Solar radiation beam through the urban canyon a). first beam reflection b). Multiple reflection and trapped solar radiation c) (Oke et al., 2017).

Table 1 The following table summarises the main methodological approaches adopted in the literature for the analysis of urban overheating across different spatial scales.

Approach	Spatial scale	Variables / methods	Main findings in literature	References
Remote sensing-based SUHI analysis	Macro	Satellite imagery, urban–rural comparison, spatial analysis of LST and land cover indicators (e.g. NDVI)	Urban overheating patterns are strongly influenced by land cover composition and urban morphology, often resulting in spatially heterogeneous and non-concentric SUHI structures	(e.g., Stewart and Oke, 2012; Oke et al., 2017)
Urban typology-based approaches (e.g. LCZ)	Macro / Meso	Classification schemes, GIS-based analysis, integration of thermal data with land cover and urban form descriptors	Urban typologies enable a more structured interpretation of intra-urban thermal variability and facilitate comparisons across different urban contexts	(e.g., Oxoli et al., 2018; Stewart and Oke, 2012)
District-scale thermal analysis	Meso	Combined remote sensing and in-situ monitoring, using LST, air temperature, land use and urban structure descriptors	Thermal heterogeneity within urban areas is strongly dependent on local surface composition, land use and urban structure, highlighting the importance of intermediate-scale analysis	(e.g., Oxoli et al., 2018; Puche et al., 2023)
In-situ microclimatic measurements	Micro	Field measurements and sensor networks, including air temperature, RH, MRT and wind	Microclimatic conditions can vary significantly over short distances, with shading, vegetation and urban geometry playing a major role in local thermal behaviour	(e.g., Jamei et al., 2016; Oke et al., 2017)
Microclimatic modelling	Micro	Numerical simulations and scenario-based analysis of Tair, MRT, wind and radiation fields	Microclimatic models enable the controlled comparison of design scenarios and mitigation strategies, supporting performance-based evaluation	(e.g., Jamei et al., 2016)

Approach	Spatial scale	Variables / methods	Main findings in literature	References
Mitigation strategies evaluation	Multi-scale	Experimental studies and simulation-based approaches using Tair, Tsurf, MRT and comfort indices	Nature-based solutions contribute to cooling mainly through shading and evapotranspiration, while material-based strategies primarily affect radiative exchanges; combined approaches are often more effective than isolated interventions	(e.g., Santamouris, 2014b; Jamei et al., 2016)

Chapter 3

3 Macroscale: Milan (Italy)

Milan has long been a relevant case for investigating the urban heat island (UHI) phenomenon, due to its rapid urban expansion, high population density and extensive built-up fabric. The earliest existing studies date back to the early 1980s, with seminal work by Bacci and Maugeri (1992). The first demonstration was of the air temperature difference between urban area and rural surroundings, which was found to be approximately 1.4 °C during the overlapping period 1951–1986. Following studies then coupled meteorological observations with surface information derived by satellite, integrating Landsat products within an urban canopy layer modelling framework for Milan and its hinterland (Borghi et al., 2000). More recent research has demonstrated that urban morphology and land cover are decisive factors in local thermal regimes. Pichierri et al. (2012) explored the spatial variability of the UHI by applying algorithms to estimate air temperature at 2 m above the ground via MODIS (Moderate-resolution Imaging Spectroradiometer) sensors. Their study quantified an average CLHI intensity of between 3 and 4 °C during nighttime hours, with peaks reaching 5 °C. Subsequently, Oxoli et al. (2018) utilised multi-sensor satellite imagery to map the LCZs of Milan, identifying an intrinsic connection between land cover composition and air temperature. They found an average thermal difference of approximately 1.5 °C between heavily urbanized and vegetated urban areas.

The analysis of thermal vulnerability in the compact tissues of Milan was further addressed by Palusci et al. (2023), who highlighted that the Building Surface Fraction (BSF) is the morphological parameter with the highest correlation to air temperature, confirming that the urban compactness of Milan prevails over other environmental characteristics, making the UHI effect evident in every season, particularly in winter. Finally, the work by Puche et al. (2023) provided original contributions by comparing Land Surface Temperature with air temperature through the integration of satellite data and Netatmo amateur weather stations. The findings of the study indicate a strong temporal correlation between the two variables, yet the spatial correlation is found to be considerably low. Although the LCZ framework is widely recognised as a fundamental approach and has proven highly effective for detailed

intra-urban characterisation, recent literature often remains concentrated on the city core or on relatively limited surrounding areas. However, metropolitan regions such as Milan necessitate a more comprehensive approach, encompassing not solely the urban fabric, but also the broader regional context in which urbanisation, infrastructure, agricultural matrices and peri-urban settlements interact. This wider framing is important to capture how the surface thermal signal is distributed beyond administrative boundaries and how it relates to the overall structure of metropolitan development.

Furthermore, satellite-based assessments of surface temperature are inherently sensitive to temporal sampling when based on individual acquisitions. Consequently, a temporally extended approach for area characterisation that utilises consistent multi-year datasets is essential to improve statistical robustness and to derive more representative and stable thermal patterns.

Here, the objective of this study is to provide a characterisation of the metropolitan and large buffer area of the summer surface thermal environment in Milan and its spatial heterogeneity. This objective is to be accomplished by leveraging an extensive multiyear Landsat record in combination with open access ancillary datasets. The study proposes an operational thermal-oriented surface classification, which is developed by consolidating land-use/cover information through the joint statistical behaviour of LST, NDVI and NDBI. This enables a structured interpretation of thermal patterns in relation to vegetation, imperviousness and functional land-use categories. This framework is then used to quantify and map the metropolitan structure of SUHI, as well as to establish a baseline for subsequent meso- and microscale analyses.

3.1 SUHI characterization in Metropolitan City of Milan

The Metropolitan City of Milan (Fig. 13) comprises 133 municipalities over an area of approximately 1575 km² and has a resident population of more than three million inhabitants. It is one of the largest and most densely populated metropolitan areas in Europe. This territory is characterised by an extensive network of infrastructures and increasingly functions as a continuous and integrated urban region (Comune di Milano, 2025). Geographically, the Metropolitan City of Milan lies in the central-western sector of the Po Valley, a wide alluvial basin bounded by the Alps to the north and the northern Apennines to the south, a

configuration that favours weak atmospheric ventilation, pollutant accumulation and frequent temperature inversions (ARPA, 2014; ISPRA, 2023). According to the Köppen–Geiger climate classification (Kottek et al., 2006; Peel et al., 2007), Milan has a warm temperate, fully humid climate with hot summers (Cfa), characterized by hot and humid summers and cold winters. Long-term data from the Milano-Brera ARPA weather station (1974–2024) indicate an average maximum temperature of 29.2 °C in July and an average minimum of –0.4 °C in January.

The main municipality, the City of Milan, covers an area of approximately 181 km² and hosts around 1.39 million inhabitants (ISTAT, 2023). Forming the densest and most urbanized core of the metropolitan region, the city has undergone substantial transformation following the decline of manufacturing activities and, more recently, after Expo 2015, which acted as a major catalyst for urban regeneration. Since 2015, large brownfield areas have been progressively redeveloped into mixed-use districts integrating research facilities, housing, public spaces and climate-oriented design strategies (Comune di Milano, 2025).

In this study, to ensure a consistent spatial domain that includes the urban core together with a sufficiently wide buffer of peri-urban and rural areas connected to the metropolitan system, the analysis was carried out over a rectangular window (Fig. 13). This window has a perimeter of 240 km and covers an area of 3562 km^2 and extends eastward toward the Crema-Bergamo sector, westward to the Ticino River corridor, southward toward the Pavia city, and northward to the Como-Brianza sector. The domain exhibits significant variations in topography and land cover from north to south. The northern sectors are proximate to the pre-Alpine belt, where the altitude increases and the land cover becomes more heterogeneous, characterised principally by numerous inhabited centres and industrial areas. The southern sectors remain within the low-altitude Po Valley and are largely characterised by agricultural land and cultivated fields.

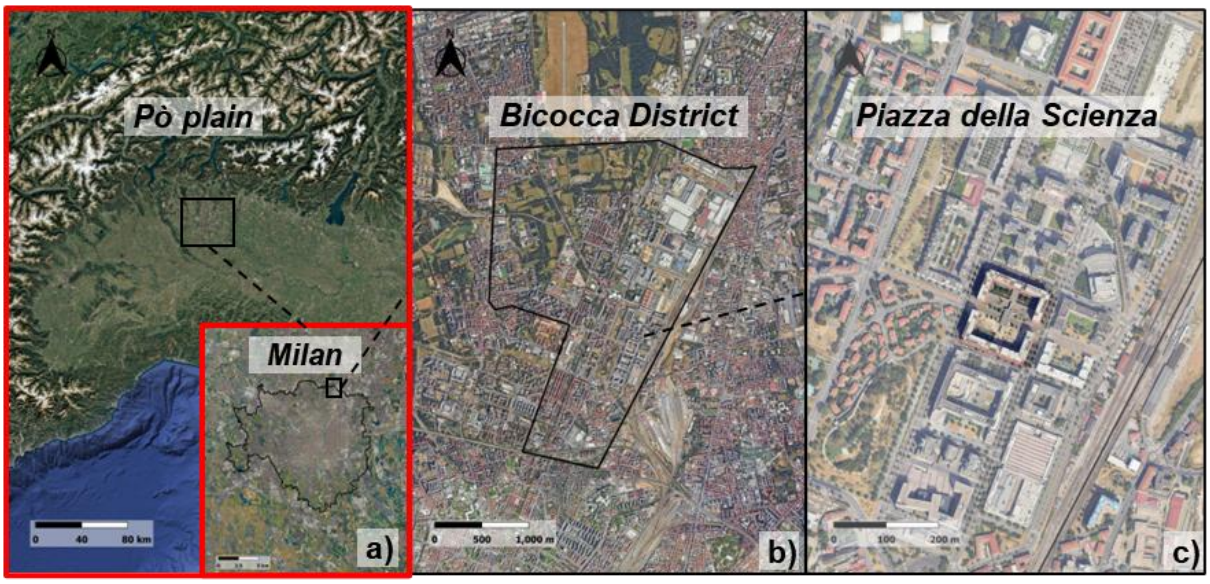

Fig. 13 Study area location. Northern Italy and Milan a) Bicocca District b) and Piazza della Scienza c) (45°30'48" N, 9°12'38" E)

3.2 Remote-sensing based approach: thermal-oriented surfaces classification

The characterisation of SUHI is based on the surface temperatures of the study area. Satellite images, specifically those captured by Landsat 8, were employed in order to obtain this information. The decision to utilise these products was motivated by two factors. Firstly, the images have already undergone a pre-processing stage, as carried out by the suppliers, thereby ensuring the availability of LST data. Secondly, the period from 2013 to the present was sufficiently sampled to ensure the relevance of the images.

Furthermore, two new bands relating to the NDVI and NDBI spectral indices were also calculated on the selected images, which are useful for surface typologies characterisation. In addition to these satellite derived indicators, the surface characterization analysis is supported by the regional land use and land cover database DUSAF (Destinazione d'Uso dei Suoli Agricoli e Forestali), a detailed, multi temporal Land use/Land cover dataset for Lombardy region. DUSAF7.0 is used here as ancillary spatial information to contextualize and discriminate against urban and non-urban patterns. Finally, to obtain a qualitative classification, multivariate statistical analysis (principal components analysis) and a clustering algorithm (K-means) were used.

3.2.1 Landsat 8 satellite products and LST retrieval

Landsat 8 is a NASA–USGS Earth observation mission. It was launched on 11 February 2013 as the Landsat Data Continuity Mission and was renamed Landsat 8 after the commissioning phase and the handover of operations to USGS (Loveland and Irons, 2016). Data became publicly available from 31 May 2013, which defines the start of the usable Landsat 8 record for long-term analyses. The satellite follows a sun-synchronous orbit with 16 days repeat cycle. The nominal equatorial crossing time is around 10 AM at local solar time. Acquisitions over the Milan region therefore occur in late morning (almost 12PM) and at a consistent local time across dates Land Surface Temperature (LST) was derived from Landsat 8 imagery, which combines the Operational Land Imager (OLI) for multispectral reflectance with the Thermal Infrared Sensor (TIRS) for thermal observations. TIRS acquires thermal infrared information on two channels (Band 10 and Band 11), enabling the retrieval of surface thermal conditions at Landsat spatial scale in conjunction with optical descriptors. In this study, LST is obtained from Landsat 8 Collection 2 Tier 1 Level 2 products, where surface temperature is provided as a dedicated surface-temperature layer (ST_B10) distributed on the Landsat analysis grid and accompanied by per-pixel quality information. This configuration allows thermal evidence and optical indices to be analysed consistently over the same spatial domain and acquisition time (Loveland and Irons, 2016). The satellite and sensors main information are reported in Table 2.

Table 2
Landsat8 satellite and sensors information

Item	Specification/value
Optical bands (OLI)	9 bands (VIS–NIR–SWIR) + panchromatic
OLI spatial resolution	30 m multispectral; 15 m panchromatic
Thermal bands (TIRS)	Band 10 and Band 11 (TIR)
TIRS spatial resolution	100 m (resampled to 30 m)
Revisit time	16 days
Product used	Collection 2 – Tier 1 – Level 2

The processing of the images was conducted utilising the online tool Google Earth Engine (GEE), employing Landsat 8 Collection 2 Tier 1 Level 2 data spanning the 2013–2025 period. The selection was restricted to summer scenes (June–August) that intersected the study window. A two-stage cloud screening methodology was implemented to minimise contamination within the area of interest, while ensuring the retention of scenes that exhibited partial cloud cover outside the domain. Initially, scenes were filtered using scene-level cloud-cover metadata (≤ 30%). Secondly, a local cloud and cloud-shadow mask was computed from the QA_PIXEL band, and only scenes with local cloud cover below 5% over the study window were retained. The final dataset comprised 33 cloud-screened summer scenes. A summary of applied filters is reported in Table 3.

To obtain LST values, digital numbers from the surface-temperature layer were converted to physical units using the scale factors provided with the Level 2 product, according to the following method:

$$LST_{Kelvin} = 0.00341802DN + 149$$

The resulting temperature was then converted to degrees Celsius ($LST_{°C} = LST_K - 273.15$).

Table 3
Summary of filters applied to satellite images summarized

Filter	Value
WRS-2 Path/Row	194/028
Time span	2013–2025
Seasonal window	June–August
Scene-level cloud filter	Cloud cover ≤ 30%
AOI cloud filter	Cloud fraction < 5%

In order to obtain a robust representation of recurrent summer surface thermal patterns, the selected LST scenes were stacked and aggregated using per-pixel median statistics, thereby producing a multi-year median LST composite map. The composite map highlights persistent hot surfaces across the metropolitan domain, with higher values typically associated with the

dense urban fabric and other impervious clusters, and lower values prevailing in vegetated and rural surroundings

3.2.1.1 Thermal contrasts and hotspots

The multiyear stack of summer LST was utilised to obtain an initial spatial characterisation of surface temperature conditions in the study area. To this end, a regular grid with 500 × 500 m cells was superimposed on the LST map (Fig. 14 and Fig. 15). The chosen size of the sample arrived at through a compromise between the requirement for detail and the need for spatial interpretability. This compromise was necessitated by the requirement to capture local variations related to urban cover and morphology, while simultaneously ensuring the creation of territorial units large enough to produce statistically robust results. This approach serves to reduce the influence of individual pixels, thus facilitating more comparable patterns across different parts of the city. In summary, the grid functions as an intermediate level of aggregation, consistent with neighbourhood-scale reading (Lietzke et al., 2015; Oke et al., 2017) , useful for analysing thermal heterogeneity without losing local information.

In consideration of the spatial resolution of Landsat surface temperature products (30 × 30 m), it is estimated that each grid cell contains 278 pixels, with slight local variations along the boundaries due to partial coverage. This grid representation facilitates consistent and spatially comparable statistics and supports the extraction of temperature profiles (Fig. 14c and Fig. 15c) covering the entire domain, summarising the distribution of LST within each cell and facilitating a structured assessment of spatial heterogeneity.

The north-south transect (Fig. 14) demonstrates considerable heterogeneity, which is associated with the continuity of urbanisation in the northern portion. The N-S transect traverses the Bicocca district (B), which is the subject of study in the following chapters.

In the northern part, the boxplot (Fig. 14c) medians are frequently elevated (41 to 44 °C), with localized episodes where the upper values reach 50 °C, indicating the presence of particularly hot cells. The area delineated by the dotted lines corresponds to the municipal boundary intersecting the profile. The profile displays a thermal plateau: the medians are around 45 °C and the interquartile range (IQR) is significantly reduced, suggesting less intra-cell variability and therefore more uniform thermal response of the coverage surfaces. In the southern section of the municipal boundary, a pronounced decrease in the LST is observed, with median values typically ranging from 34 to 37 °C and local minima recorded at 31 to

33 °C. In this southern portion, the boxplots become lengthier once more and the whiskers become more irregular, consistent with a more fragmented mosaic, which in turn amplifies spatial heterogeneity. The sequence under consideration highlights how the municipality represents the warmest and most homogeneous core, while the outer areas show greater variability and progressive cooling.

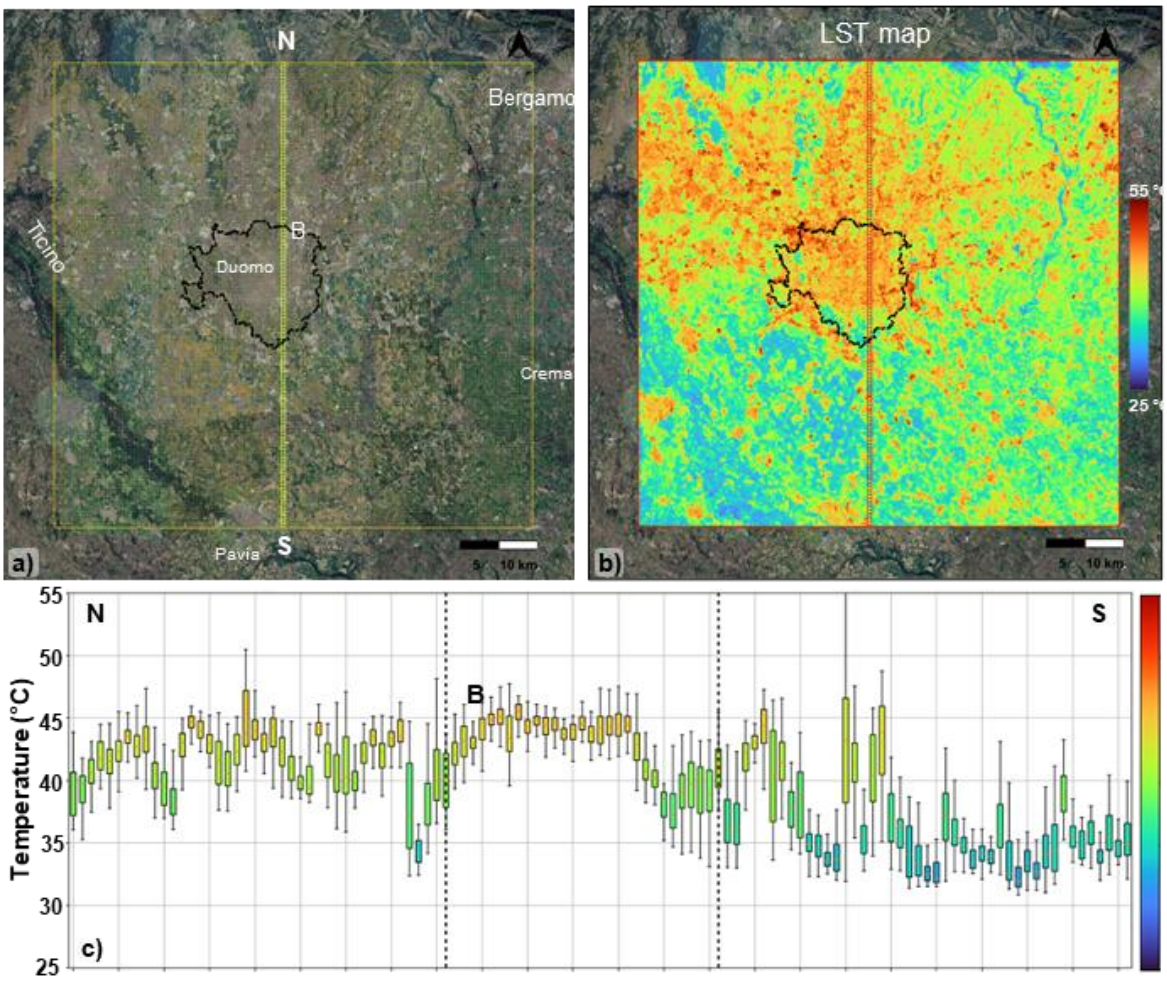

Fig. 14 Satellite-based mapping of the study area with a regular grid and North–South (N–S) transect; the perimeter of the Municipality of Milan is highlighted together with the main reference elements (Duomo and Bicocca "B", and major hydrographic features such as the Ticino River and main cities; a). Map of the multi-year stack summer LST (2013–2025) with the municipal boundary superimposed b). N–S profile of the LST on a grid: the dotted vertical lines indicate the extent of the municipality of Milan c).

In this second case (Fig. 15), the transect was drawn through the centre of the city (Duomo). The analysis of the area with a west-east transect confirms the centrality of the municipal area as the most thermally compact core. However, the results also suggest asymmetries between the two sides, although these are less pronounced than those observed along the north-south transect. A shown in Fig. 15c, in the western sector, the medians initially rise to a range of 42 to 45 °C, subsequently transitioning into a cooler phase with medians declining to 35 - 38 °C. This transition signifies both urban discontinuity and an increased prevalence of permeable coverings. In the vicinity of the initial municipal boundary, a pronounced peak is evident, with boxes attaining medians of 46 to 48 °C, indicative of localized hotspots. Within the municipal boundaries, the profile stabilises at elevated values, with medians ranging from 44 to 45°C and narrower boxes, once more indicating reduced variability and enhanced surface homogeneity. In the east side, a decline in temperature is observed, accompanied by increased variability. The median temperature values typically range from 36 to 40°C, with occasional local minima of 32 to 34°C and sporadic excursions above 43 to 45°C. This phenomenon is indicative of a more heterogeneous and mixed landscape character. In summary, even along the W–E axis, heterogeneity increases with distance from the urban centre, while the municipality emerges as the warmest and most uniform portion of the domain.

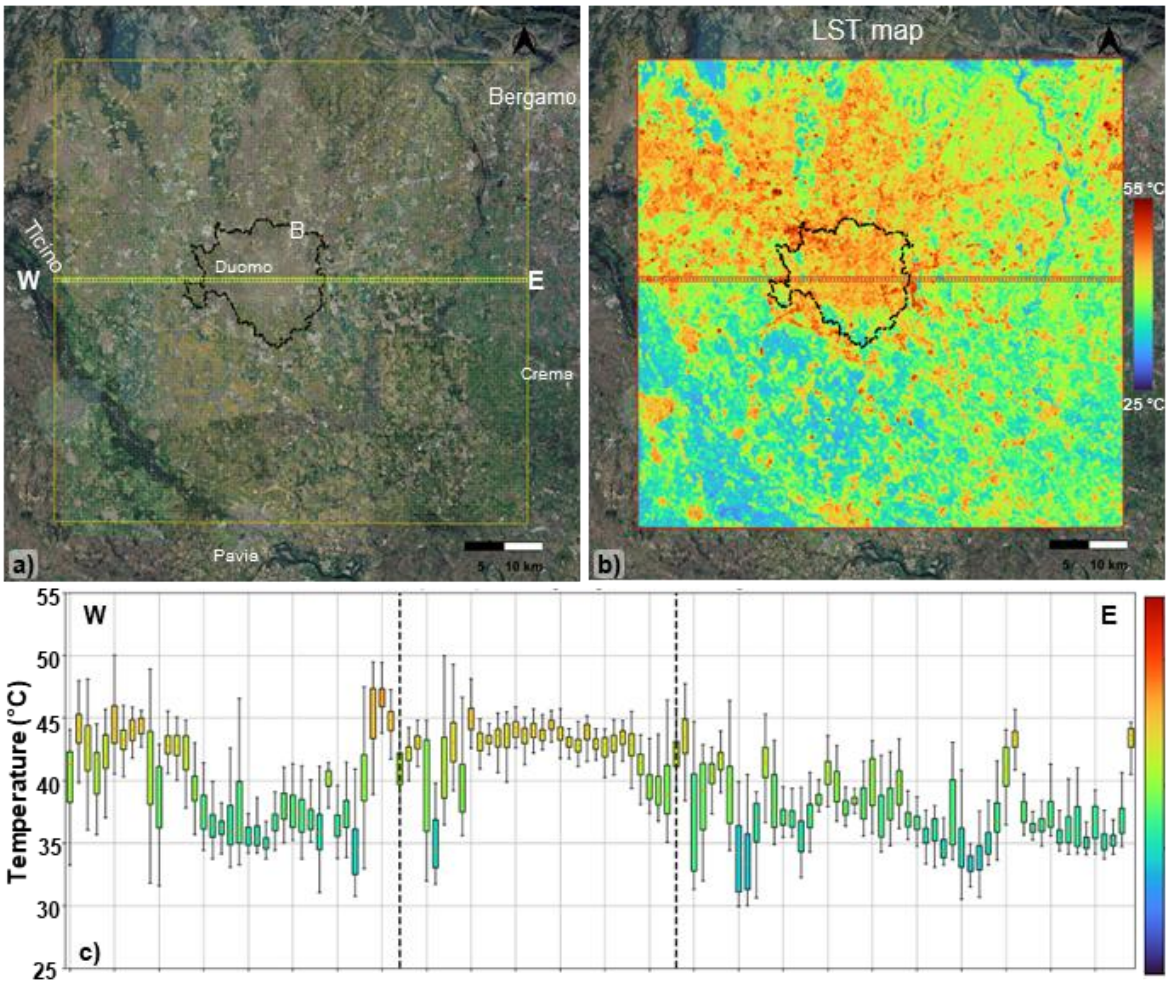

Fig. 15 Satellite-based framing of the study area with a regular grid and West–East (W–E) transect; the perimeter of the Municipality of Milan is highlighted together with the main reference elements (Duomo and Bicocca "B" and major hydrographic features such as the Ticino River and main cities; a). Map of the multi-year stack summer LST (2013–2025) with the municipal boundary superimposed b). W–E profile of the LST on a grid: the dotted vertical lines indicate the extent of the municipality of Milan c).

3.2.1.2 Spectral indices and thematic layers

To support interpretation of the thermal signal through surface composition, NDVI and NDBI were computed from Landsat (Fig. 16) surface reflectance for the same set of selected scenes and aggregated using the same per-pixel stack approach. To identify vegetated cover from impervious and built-up materials across the Metropolitan City of Milan, this study employs the coupled use of the Normalized Difference Vegetation Index (NDVI) and the Normalized Difference Built-up Index (NDBI). The NDVI concept was introduced during the early Landsat/ERTS era by (Rouse Jr, 1974) and subsequently consolidated and popularized for

operational vegetation monitoring by (Tucker, 1979). Using surface reflectance (ρ), NDVI is defined as:

$$\text{NDVI} = \frac{(NIR - Red)}{(NIR + Red)}$$

Eq. [2]

NDVI values typically range from −1 to +1, with higher positive values indicating denser or more vigorous vegetation.

For impervious cover, Zha (2003) originally proposed NDBI as an automated method to map urban built-up areas from Landsat TM imagery. Its standard form is:

$$\text{NDBI} = \frac{(SWIR - NIR)}{(SWIR + NIR)}$$

Eq. [3]

For Landsat 8 OLI, these bands correspond to Red (Band 4), Near InfraRed (NIR, Band 5), and SWIR (Band 6).

NDVI is among the most established and widely used vegetation metric in optical remote sensing. It leverages the characteristic spectral behaviour of green vegetation, with low red reflectance and high NIR reflectance through a normalized difference formulation (Eq. [2]; Jiang et al., 2006). Complementarily, NDBI is designed to highlight built-up surfaces by exploiting the tendency of many urban materials (e.g., concrete, asphalt, rooftops) to exhibit comparatively higher reflectance in the ShortWave InfraRed (SWIR) than in the NIR enabling built-up extraction from Landsat imagery, through a normalized difference formulation (Eq. [3]; Zha, 2003).

This produces three mutually consistent cumulative layers (LST, NDVI and NDBI) defined over the same spatial extent, season, and filtered acquisition set, thereby enabling a coherent comparison between surface temperature patterns and vegetation and built-up proxies at Landsat scale. At urban scale and 30 m Landsat resolution, the NDVI–NDBI pair provides a robust and reproducible way to distinguish pixels dominated by vegetation, from areas dominated by impervious and built-up cover, while remaining methodologically stable for multi-year comparisons. The image Fig. 16 shows the relationship between urban structure and vegetation cover on a metropolitan scale: compared to a highly urbanized core, the NDVI (Fig. 16a) shows a gradual increase in vegetation towards the outskirts, while the NDBI (Fig.

16b) shows higher values in compact and rich of infrastructure areas. Overall, the two indices indicate a clear gradient from centre to periphery and significant spatial heterogeneity, which is instrumental in interpreting the subsequent variations in surface temperature patterns, further supporting the interpretations outlined in the preceding paragraph (Par. 3.2.1.1).

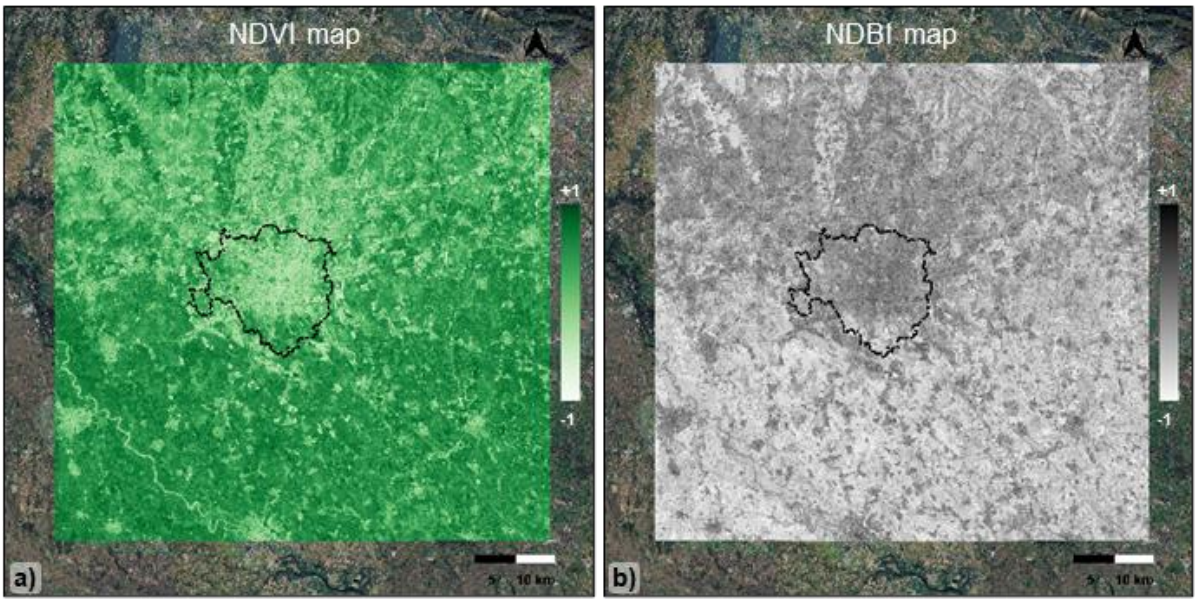

Fig. 16 Map of the multi-year stack NDVI in the study area a), and map of the multi-year stack NDBI in the study area b).

3.2.2 Open-source data land use classification

The regional land use and land cover database DUSAF (Destinazione d'Uso dei Suoli Agricoli e Forestali) was used as ancillary information on surface cover and land use. DUSAF is provided by Regione Lombardia as an open-access dataset and is produced through photointerpretation of high-resolution orthophotos. The latest release (Regione Lombardia, 2023) refers to colour orthophotos acquired in 2021. The DUSAF legend is organised into five hierarchical levels. The first level includes five macro categories (artificial surfaces, agricultural areas, forest and semi natural areas, wetlands, and water bodies). These categories are progressively detailed at levels 2 and 3, which follow the CORINE Land Cover nomenclature, while levels 4 and 5 provide additional local detail. The dataset is distributed as a polygon layer and adopts a reference scale of 1:10000. At this scale, the minimum mapping unit for areal classes is 1600 m², and the minimum linear dimension of polygons is 20 m. The DUSAF dataset is a fundamental tool for territorial analysis, as it provides detailed

vector layers at a scale of 1:10000, representing a homogeneous reference for monitoring land cover and land use that directly influences urban heat flows (Oxoli et al., 2018).

The regional DUSAF polygon layer was clipped to the study window. Within this area, 68 distinct DUSAF classes were represented. In the DUSAF layer, the spatial distribution of the polygons exhibits a marked contrast between the urban core and the peripheral areas (Fig. 17b). Within the municipality of Milan, land cover types associated with urbanized and infrastructural areas prevail, exhibiting a relatively continuous distribution that reflects the compactness of the built fabric. Moving outwards, particularly in the southern and southeastern quadrants, the land cover becomes more uniform and organized over extensive areas, which is consistent with the presence of both agricultural and peri-urban areas. Conversely, in the northern and northeastern regions, a more fragmented configuration emerges, characterized by the alternating presence of different land use classes in proximity. This suggests a greater degree of morphological complexity in these landscapes.

Here, the clipped DUSAF polygons were used as spatial units to extract satellite derived values from the he stacked satellite layers LST, NDVI and NDBI maps. Subsequently, the extracted pixel values were grouped according to their corresponding DUSAF class. This ensured that each of the 68 classes was associated with an aggregated distribution of values, representing the total of all pixels falling within polygons belonging to that class.

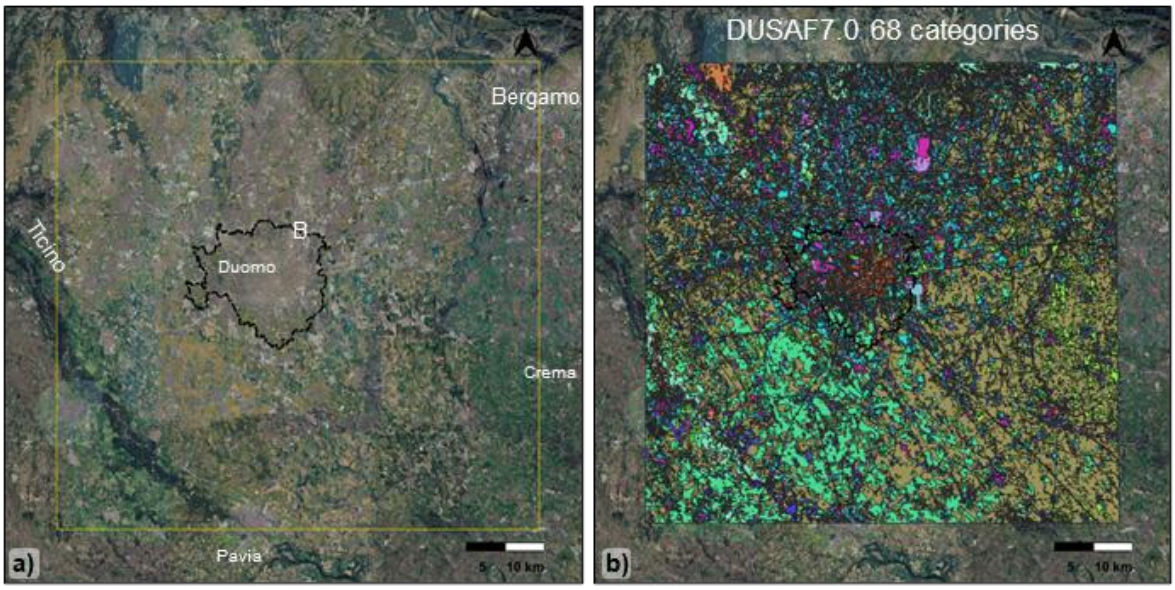

Fig. 17 Overview of the study area and distribution of land use/land cover classes: satellite image showing the perimeter of the Municipality of Milan and reference to the Duomo and Bicocca (B, a); DUSAF 7.0 classification (68 categories) across the entire domain of analysis, highlighting the contrast between the central urbanized fabric and agricultural and peri-urban land cover in the outer areas b)

3.2.3 Multivariate analysis and clustering

Principal component analysis (PCA) is a multivariate technique used to reduce the dimensionality of a dataset made of correlated variables (Abdi and Williams, 2010). It transforms the original variables into a new set of uncorrelated components. Components are ordered so that the first components retain most of the total variance. PCA was introduced by Pearson (1901) and later developed by Hotelling (1933). Its computation is based on an eigenvalue–eigenvector decomposition of a covariance or correlation matrix.

In this study, PCA was applied to a set of statistics derived from the extracted LST, NDVI, and NDBI, namely median and quartiles Q1 and Q3 and, for LST only, also minimum and maximum (Fig. 18a), for each of the 68 categories. The 68 feature vectors (one per class) constituted the input dataset for the multivariate analysis. Prior to the implementation of PCA, a process of standardization of features was conducted with the objective of ensuring the comparability of variables and statistics. PCA was employed to reduce collinearity and dimensionality while preserving the majority of the information content. A total of four principal components were retained, as they accounted for more than 98% of the total

variance (Fig. 18). The retained component scores were subsequently utilized as the input space for clustering.

To obtain discrete thermal-oriented surface groups, k-means clustering (MacQueen, 1967) was performed on the retained PCA scores. Different values of K were tested, solutions with K = 3 and K = 5 were investigated. The result of setting K to 3 was an excess of aggregation, which caused the merging of land cover types that exhibited clearly divergent thermal-spectral behaviour. Conversely, the setting of K to 5 yielded a more refined partition, which primarily resulted in the division of internally similar classes. This process served to reduce interpretability without concomitantly enhancing meaningful explanatory power. Finally, the solution with K = 4 was selected because it provided a clear separation of surface types while avoiding excessive fragmentation. The resulting clusters (Fig. 18c) were used to re-aggregate the original 68 DUSAF classes into 4 broader categories. The K = 4 solution provided the optimal compromise between separability in PCA space and thematic coherence, yielding four groups that can be interpreted as two vegetated signatures, one impervious or paved group and a water related group, consistent with both the PCA clustering structure and the DUSAF legend hierarchy.

Indeed, the scatter plots obtained from PCA (Fig. 18) demonstrate a clear tendency for the 68 classes under consideration to cluster together, with separation primarily occurring along PC1, the component that accounts for the predominant proportion of overall variability (71.9%). Samples associated with paved surfaces tend to be located on positive PC1 values, while vegetated classes are mainly distributed on negative PC1 values, thus highlighting a consistent gradient between artificial surfaces and vegetated coverings. The subsequent components contain information that facilitates a comprehensive description of the internal structure of the groups. The vegetated classes exhibit a propensity to organise themselves into two subgroups, with differences in position and dispersion in the component space. This suggests variability that is linked to different conditions of density, composition of the cover. The Water class, although less numerous, appears more isolated than the others, especially along PC2. This is consistent with a distinct spectral and thermal signature, and therefore less prone to erroneous identification as vegetated or artificial surfaces. In seeking a more simplified representation, with a view to accentuating the four groups respective

characteristics, the following nomenclature has been adopted: Paved, Vegetated1, Veghetated2 and Water (Fig. 18c)

PCA	Min	Med	Max	Q1	Q3
LST	✓	✓	✓	✓	✓
NDVI	×	✓	×	✓	✓
NDBI	×	✓	×	✓	✓

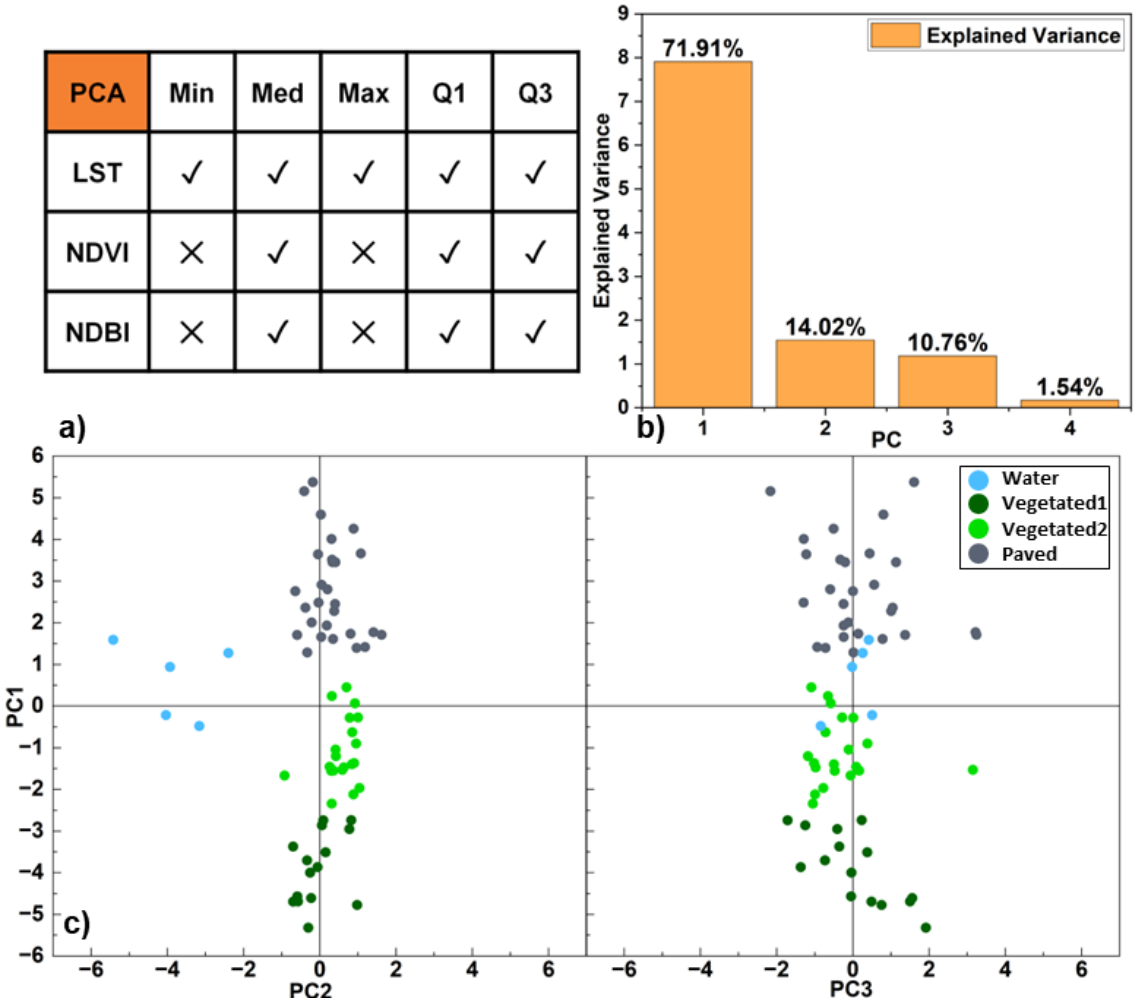

Fig. 18 Summary statistics derived from LST, NDVI, and NDBI and used as input variables for PCA a). Variance explained by the first four principal components b). Projection of samples in the principal component space (PC1–PC2 on the left; PC1–PC3 on the right) c)

3.2.4 Thermal-oriented classification

The clustering results obtained allow for the reduction of the 68 DUSAF classes to a reduced set of typologies of surfaces and thermally coherent groups, thereby improving the readability of the centre-periphery structure of the domain (Fig. 19). The map (Fig. 19a), categorized into four distinct categories, offers a clear visual representation of the impervious core, which is concentrated within the municipal boundary and along the primary infrastructure corridors that extend northward and north-westward (Paved). Outside this core,

two distinct vegetated signatures dominate most of the metropolitan territory, yet with different spatial organisations: one is more continuous and prevalent in the southern and south-eastern sectors (Vegetated1) while the other is more fragmented and interspersed with artificial areas toward the north and north-east (Vegetated2), where the coexistence of settlements and vegetation covers suggests higher morphological complexity. The last category (Water), though less extensive, displays a linear pattern associated with major water bodies and the river network, remaining distinctly separated from the other covers. To further support interpretation and operational use in the subsequent analyses, the four categories were additionally aggregated into a binary map (Fig. 19b), synthesizing the information as vegetated versus artificial and impervious surfaces. The classification of the vegetated area passes from Vegetated1 and Vegetated2 to Vegetated while the impervious surfaces remain classified as Paved.

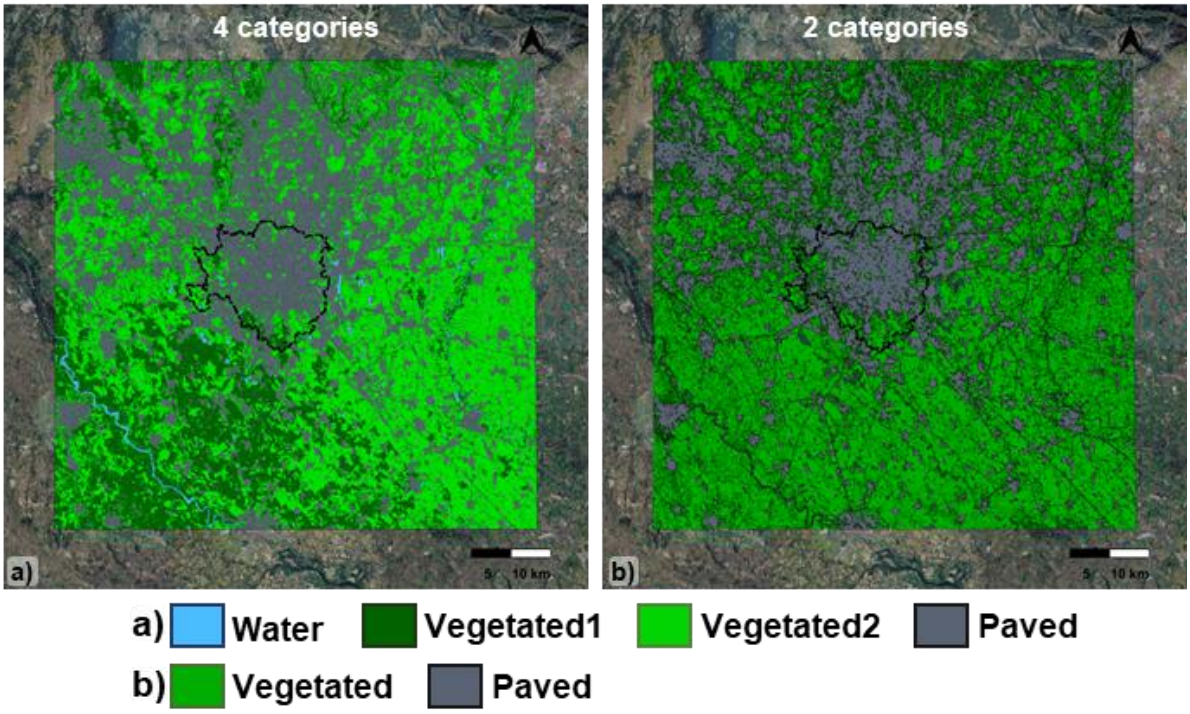

Fig. 19 Four-category reclassification map a) and its further aggregation into two categories: vegetated vs paved surfaces b)

3.3 The spatial component: patterns, land use/land cover dependencies, heterogeneity

Fig. 20 provides a schematic representation of the workflow adopted for the derivation of thermal-oriented surface classes and the reference layers utilized in the SUHI analysis. The DUSAF 7.0 polygons (68 classes) were overlaid with the multi-year summer composites of LST, NDVI and NDBI in order to extract pixel values and compute class-wise summary statistics. These descriptors were then reduced through PCA and used as input for a k-means clustering, producing four coherent surface groups. These groups were subsequently aggregated into a binary partition to support the spatial interpretation of thermal patterns and the SUHI contrast analyses.

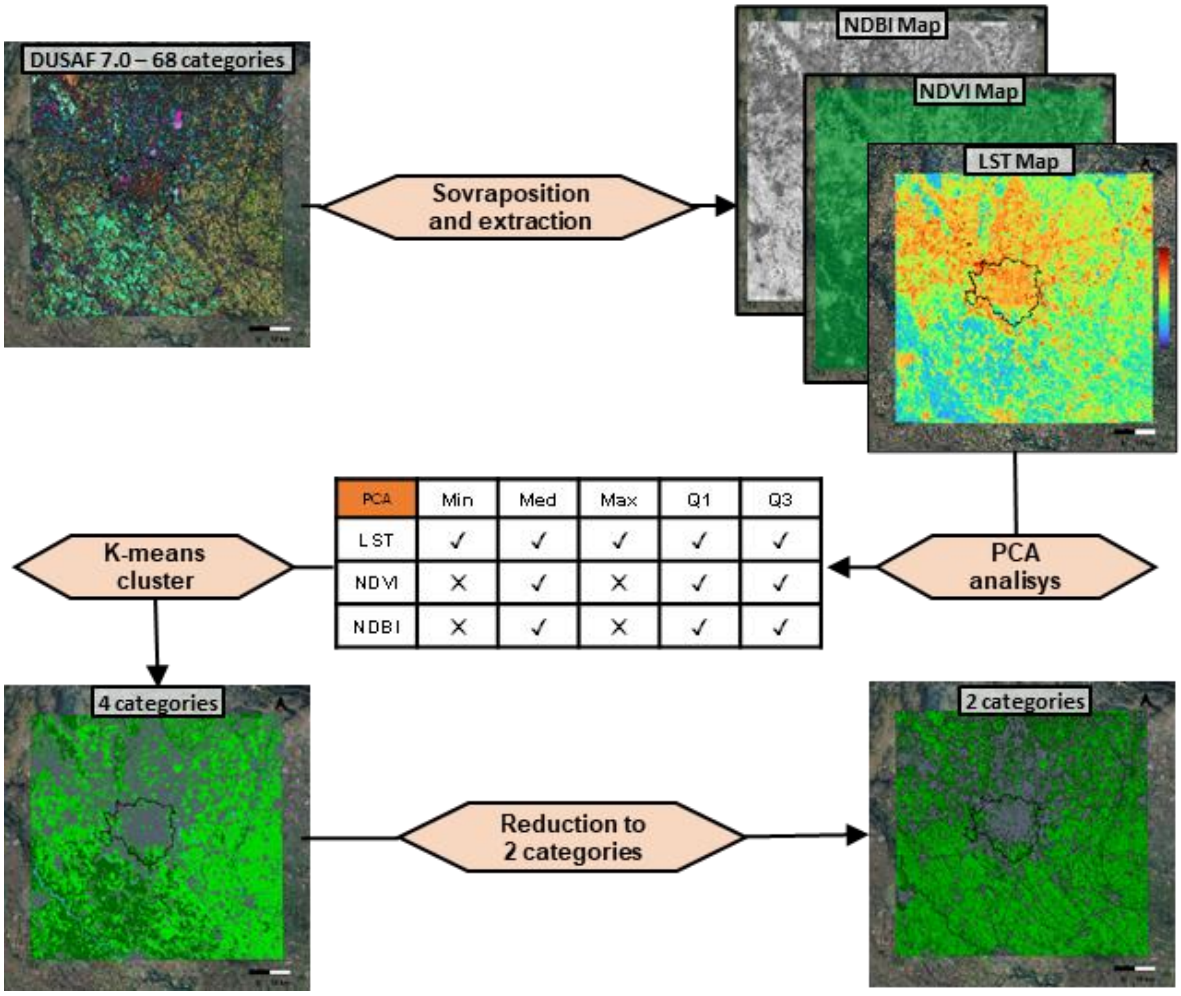

Fig. 20 Schematic representation illustrates the process of obtaining reduced surface characterisation.

3.3.1 Transect-based thermal heterogeneity

By overlaying the 500 × 500 m grid on the temperature maps and the derived classification map, each cell was attributed, together with its LST, the percentages of paved and vegetated surfaces (Fig. 21 and Fig. 22). These metrics are used to interpret the thermal signal in relation to surface composition.

Along the north-south profile (Fig. 21c), LST variability can be interpreted as a direct response to changes in cell composition. Sectors with a high proportion of artificial or impervious surfaces consistently correspond to higher LST, whereas an increase in vegetated cover is associated with lower temperatures. In the northern part of the transect, cells often have a mixed composition, with a moderately high percentage of paved surfaces (60 to 80%) and a comparatively lower percentage of vegetation (20 to 40%). Within the interval delimited by the dashed vertical lines (the municipal boundary), the pattern becomes more compact: strongly impervious cover dominates, with the percentage of paved surfaces frequently around 70 to 95%, and a reduced percentage of vegetated surfaces (5 to 30%). This corresponds to a thermal plateau and smaller oscillations, suggesting greater surface homogeneity at the cell scale. Moving southwards, a clear transition towards vegetation-dominated cells is observed, with percentage of Vegetated class often exceeding 70 to 90% and percentage of Paved class frequently dropping below 10 to 30%. In this sector, LST decreases and local discontinuities appear, coinciding with increases in percentage of Paved, which can be interpreted as infrastructure nuclei embedded within an agricultural matrix.

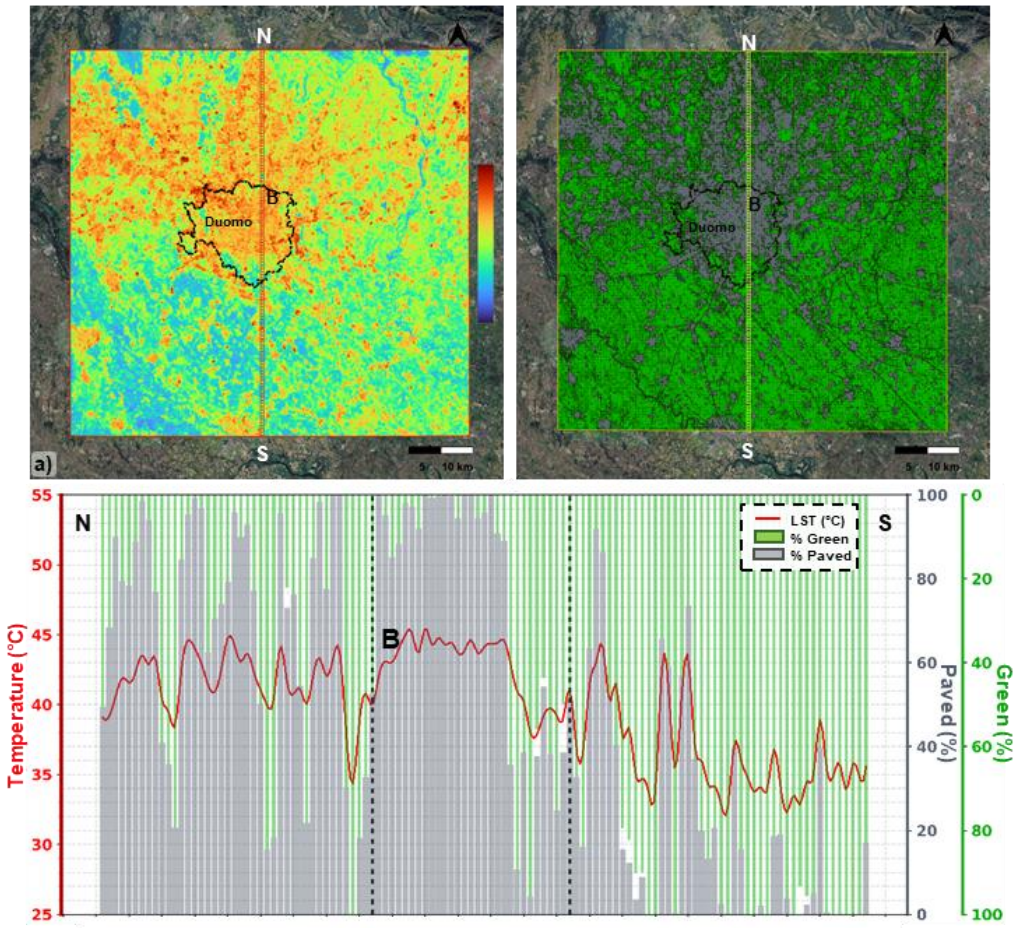

Fig. 21 Map of the multi-year average summer LST with the municipal boundary superimposed and the main features Duomo and Bicocca (B, a). Aggregation into two categories: vegetated vs paved surfaces with the municipal boundary superimposed and the main features Duomo and Bicocca (B, b) N–S profile of the LST, percentage of Paved classes and Vegetated class on a grid (boxplot per cell): the dotted vertical lines indicate the extent of the municipality of Milan c). The white areas in the map correspond to water bodies, which were excluded from the classification.

A coherent relationship is also evident along the west-east transect (Fig. 22c): relative LST peaks align with cells characterised by a higher percentage of paved surfaces while cooler phases correspond to cells where vegetated spaces dominate. In the western sector, prior to entering the municipality, cells alternate between a high percentage of paved surfaces (50 to 90%) and more vegetated areas (>70 to 90% green cover), and this alternation is reflected by successive decreases and increases in LST. Within the municipal limits, the cover becomes predominantly artificial again, with percentage of Paved class close to 80–100% and low percentage of Vegetated class (0 to 30%); accordingly, LST stabilises at a high, uniform level. Moving eastward, vegetation-dominated cells prevail once more (often >70 to 90% Vegetated

and <10 to 30% Paved), accompanied by decreasing LST. The isolated thermal peaks that persist in the eastern sector coincide with local increases in percentage of paved surfaces indicating that the impervious component can generate hotspots even outside the urban core at a sub-metropolitan scale.

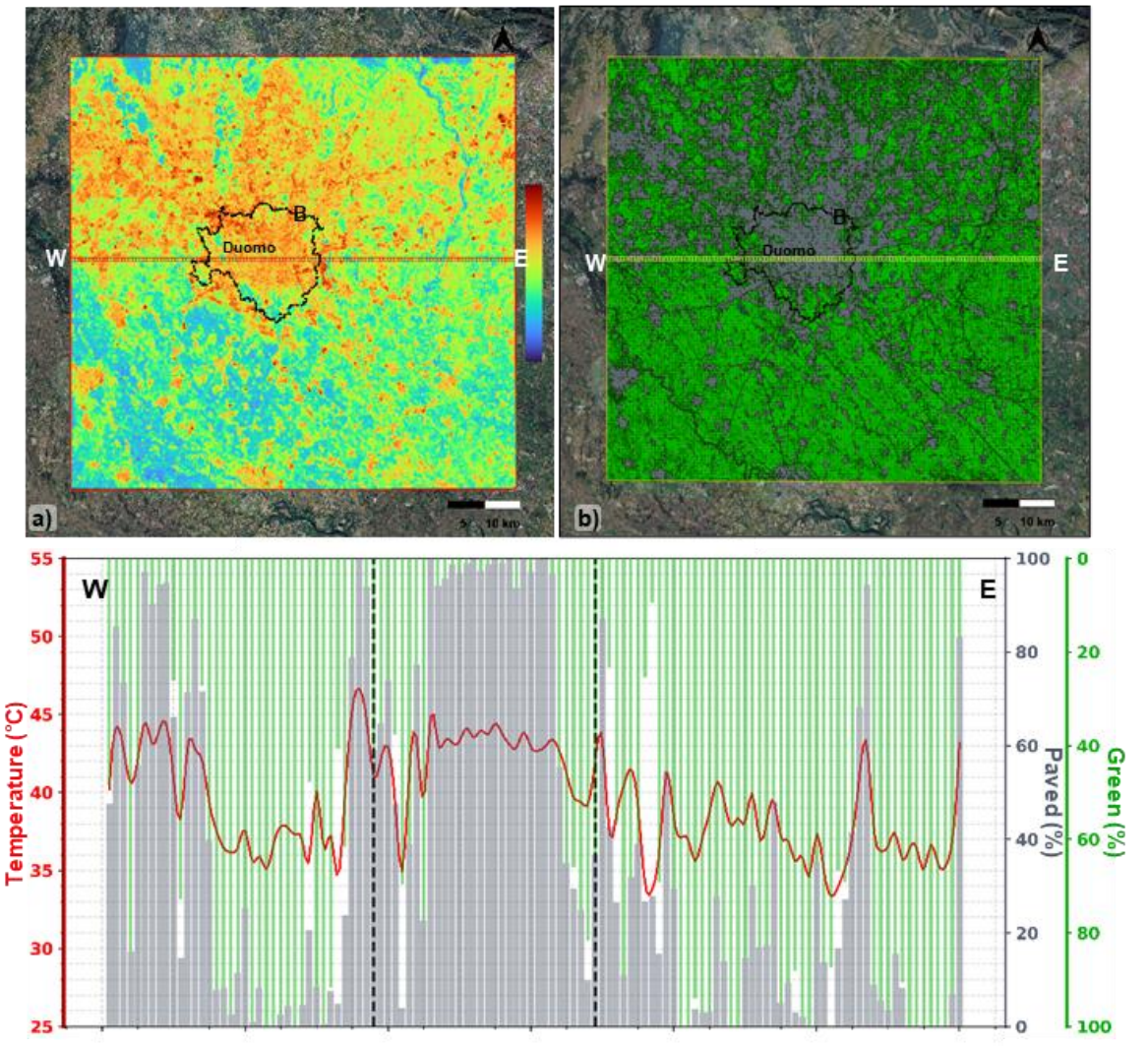

Fig. 22 Map of the multi-year average summer LST with the municipal boundary superimposed and the main features Duomo and Bicocca (B, a). Aggregation into two categories: vegetated vs paved surfaces with the municipal boundary superimposed and the main features Duomo and Bicocca (B, b) W–E profile of the LST, percentage of Paved classes and Vegetated class on a grid (boxplot per cell): the dotted vertical lines indicate the extent of the municipality of Milan c). The white areas in the map correspond to water bodies, which were excluded from the classification.

3.3.2 Radial-based thermal heterogeneity

To complement the transect-based analysis with a radial perspective, the domain was discretised into concentric rings centred on the urban core (Duomo) and angular sectors at constant intervals (Fig. 23). The rings are defined by progressively increasing distance thresholds from the centre and extend outward at a width of 4.5 km each up to a maximum radius of 27 km, covering almost the entire study area. Within each ring, the azimuthal subdivision uses N = 16 equal sectors, giving an angular width of 22.5° per sector. Orientation is defined starting from 0° = North (Fig. 23a).

The results show a clear gradient from the centre to the periphery. Considering the mean values for each ring, LST decreases progressively from the centre to the edge of the area. Specifically, the temperature decreases by 6°C, from 43.5°C to 37.4°C, while the proportion of impervious surfaces decreases markedly (Paved: 89.7% to 27.3%), and vegetated cover increases (Vegetated: 10% to 71.8%).

Beyond the radial gradient, the concentric LST map (Fig. 23b) reveals a distinct directional pattern. In the northern and north-western sectors, relatively high temperatures persist outside the municipal boundary, remaining comparable to those in the central rings. This suggests that the thermal signal is not confined to the administrative core, but follows the continuity of urbanised, impervious surfaces extending towards the north and north-west, maintaining elevated LST at increasing distances. By contrast, moving towards the eastern quadrants, LST decreases more markedly with distance, indicating a faster transition towards cooler, more vegetated surfaces. In the southern sectors, finally, the decrease is more systematic and spatially coherent: most directions show progressive cooling from the centre outwards, which is consistent with the extensive presence of vegetated and agricultural land in the south of the area (Fig. 23c).

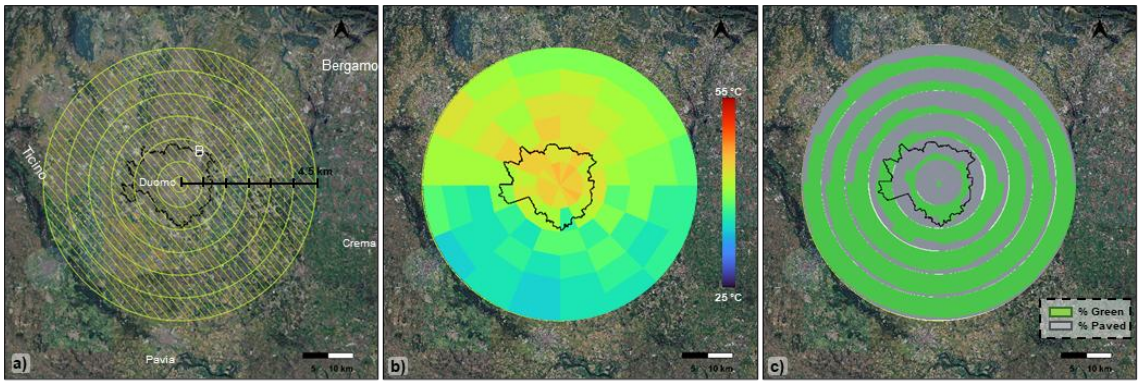

Fig. 23 Radial discretisation centred on the Duomo. The study domain is partitioned into 6 concentric rings and 16 equal-angle sectors a). Polar representation of mean summer LST by sector × ring, with the Municipality of Milan boundary overlaid b). Polar representation of surface composition by sector × ring with the municipal boundary overlaid c).

3.4 Extent and intensity of the SUHI

In order to calculate SUHI intensity in accordance with the standard urban-rural definition (Oke, 1982), only paved surfaces within the Municipality of Milan were considered as urban, while the rural reference was defined as vegetated areas outside the municipal boundary (Fig. 24a). To achieve precise isolation of the urban thermal effect, the analysis was conducted with the exclusion of water bodies and rural areas situated at elevations more than 150 m.. Water bodies were excluded from the classification and subsequent analyses, not because of their negligible role in influencing land surface temperatures, but due to methodological and scope-related considerations. One of the objectives of this study is to assess the SUHII by comparing urban areas with representative non-urban reference surfaces. In this context, vegetated rural areas were selected as the reference baseline, as they provide a consistent and widely adopted benchmark for SUHII estimation. In contrast, water bodies exhibit fundamentally different thermal behaviours, which are not directly comparable with those of built-up or vegetated surfaces, and could therefore affect the consistency of the comparison. This choice is also consistent with established methodologies in the literature, where water bodies are commonly excluded from both urban and non-urban references in SUHII calculations, together with areas characterized by extreme elevations, to reduce biases in the estimation of urban-induced thermal effects. As highlighted by Liu et al. (2023), the delineation of non-urban reference areas plays a critical role in determining SUHII values and trends, and the inclusion of heterogeneous or thermally unstable surfaces may lead to

misinterpretation of the results. Furthermore, within the scope of this research, nature-based solutions are investigated primarily in terms of vegetation and material-related strategies, without explicitly considering water-based interventions. Nevertheless, water bodies can locally contribute to temperature mitigation, as also suggested by some LST patterns observed in the maps. While their influence is not explicitly quantified in this study, it is acknowledged that their exclusion may affect the local thermal representation, although it does not compromise the overall objective of comparing urban and vegetated reference conditions. This methodological choice is particularly relevant for the interpretation of the SUHII results presented in the following section, where maintaining a consistent and comparable non-urban reference is essential to ensure the robustness of the analysis. Moreover, the exclusion of elevated regions (Fig. 24b) is necessary to mitigate natural thermal variability introduced by topography and relief (Liu et al., 2023).

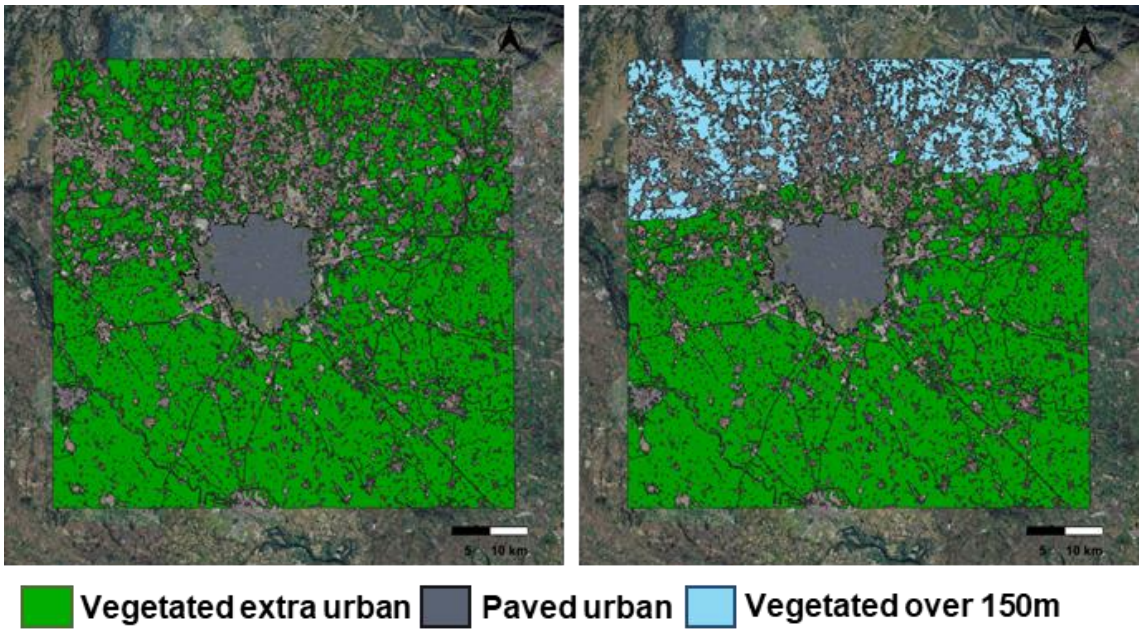

Fig. 24 Urban and rural reference masks for SUHI computation. Urban mask derived from paved polygons within the Municipality of Milan and rural reference from vegetated polygons outside the municipal boundary a); water bodies and vegetated areas above 150 m a.s.l. were excluded to reduce non-urban thermal variability b)

After the delineation of the two final masks, multiyear summer LST values were extracted over each class. SUHI intensity was subsequently calculated as the difference between the mean LST of the urban impervious mask and the mean LST of the extra-urban vegetated

reference. The results demonstrate a significant disparity between the two surface contexts, with a temperature difference of $\Delta T = 7.64$ °C (Urban = 45.57 °C; Vegetated = 37.93 °C) and a maximum excess of 17.2 °C. This metric provides a compact and interpretable estimate of the average summer surface thermal penalty associated with the impervious urban fabric relative to a vegetated background.

The spatial implications of this contrast are illustrated by the SUHI excess map (Fig. 25), which shows the continuous distribution of surface thermal anomaly with respect to the extra-urban green reference across the metropolitan domain. The observed pattern indicates that the strongest excess is not confined to the municipal boundary; high-anomaly areas extend well beyond the administrative core, delineating a metropolitan-scale structure consistent with the continuity of impervious surfaces and major infrastructure corridors. Moreover, this pattern is characterised by a high level of fragmentation, with elevated temperatures observed both within and surrounding the urban core, and in areas exhibiting high levels of urbanisation and impervious surfaces. It is evident that excess values manifest themselves in a more extensive and persistent manner within the northern sector. Concurrently, notable concentrations have been observed in the north-western region, where localised higher anomalies are observable. Conversely, southern sectors exhibit comparatively weaker and less continuous excess, in line with a more vegetated and agriculturally dominated landscape.

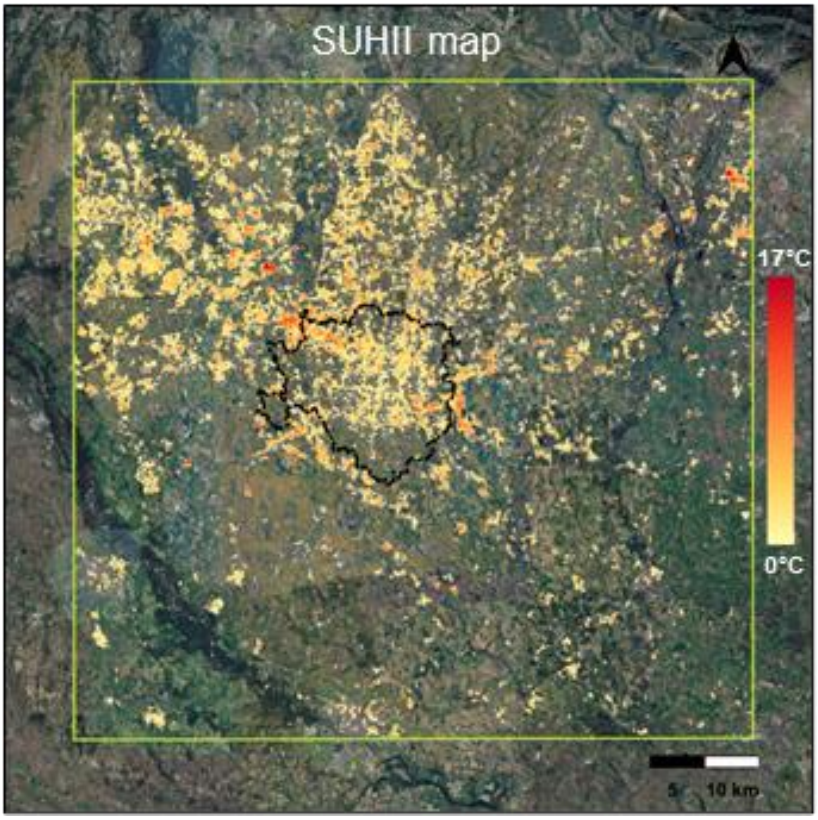

Fig. 25 SUHI excess map. Spatial distribution of surface thermal anomaly relative to the extra-urban vegetated reference, highlighting that the highest excess values extend beyond the municipal boundary and are more persistent in the northern sectors, with notable concentrations toward the north-west.

3.5 Discussion and conclusion

The macroscale results suggest that the surface thermal field in Milan during the summer season is characterised by significant heterogeneity. A gradient from the centre to the periphery is evident, and this is repeatedly modulated by the metropolitan land surface mosaic. In this fragmentation, compact impervious fabrics, infrastructures, and agricultural matrices alternate in space. This produces a directional heterogeneity in which the thermal signal propagates preferentially along urbanised and infrastructural corridors, persisting beyond the municipal boundary and generating extended warm areas that are consistent with the broader development structure of the city. Conversely, sectors characterised by more continuous vegetation and agricultural cover exhibit an earlier and more persistent attenuation of LST, reinforcing an asymmetric metropolitan pattern rather than a purely

concentric one. Consequently, the emergence of SUHI is not merely a comparison signal between the city core and the surrounding rural area, but rather a metropolitan-scale pattern. The thermal-oriented surface characterisation employed in this study offers a concise method for correlating LST patterns with broader surface contexts across the entire domain. This framing assumes particular importance as the analysis progresses towards finer scales, where the emphasis shifts from pattern description to local controls and mechanisms.

Recent studies have demonstrated the value of detailed urban typologies, such as Local Climate Zones (LCZs), in understanding intra-urban thermal variability (Oxoli et al., 2018; Puche et al., 2023). However, the thermal-oriented classification employed in this study is intentionally more simplified. The objective of this study is not to compete with LCZ schemes in terms of classification or statistical relevance. Instead, the aim is to provide a reproducible and operational characterisation of surface contexts over a large metropolitan domain that is more prompt. In practice, this approach is comparatively straightforward to update and manage over time: the satellite composites can be updated as new Landsat scenes become available, and the thematic component can be updated by incorporating revised DUSAF releases, without requiring the full construction and calibration effort typically associated with LCZ mapping (Stewart and Oke, 2012). This renders the framework particularly adapt to produce consistent, large-area descriptive evidence across extended temporal windows, and for the establishment of a robust background interpretation against which subsequent, finer scale analyses can be developed.

The macroscale analysis provides a baseline characterisation of the metropolitan thermal environment, intended not only to describe the overall SUHI intensity of Milan, but also to frame and contextualise the finer-scale investigations developed in the subsequent chapters. By adopting the traditional urban-rural contrast and a spatially explicit representation of thermal anomalies, this section outlines the dominant gradients and directional asymmetries that structure the thermal field at the macroscale. This establishes the reference setting against which district- and microscale dynamics can be interpreted.

Chapter 4

4 Mesoscale: Bicocca district

In the Milan context, as pointed out in the previous chapter, recent studies have utilised LCZ-based approaches to interpret urban thermal patterns in relation to the local urban fabric, rather than treating the city as a spatially uniform thermal field. For instance, Oxoli et al. (2018) relate air-temperature observations from meteorological stations to the surrounding land-cover composition by describing the local context through station-centred buffers, while Puche et al. (2023) combine LCZ mapping with Landsat-derived LST and in-situ air-temperature data to characterise thermal patterns across different urban typologies over the Milan metropolitan area. The contributions on Milan study area under discussion are referenced here not to reframe UHI in Milan at a finer resolution, but to support the rationale for analysing thermal variability through locally representative units and typologies.

The present chapter is built on this perspective by focusing on a district scale and investigating the Bicocca district through high-resolution thermal characterisation. Bicocca is not regarded as a statistically representative subset of Milan; rather, it is approached as an urban laboratory shaped by decades of redevelopment and regeneration, where multiple urban fabrics and surface conditions coexist within a limited area. This renders it especially adapt to the objective of the present study, namely mesoscale thermal characterisation in the context of long-term urban transformation. Moreover, Piazza della Scienza, situated within the university campus, exemplifies the transformation that has occurred in this district. The square was the subject of a regeneration intervention, the details of which are described and analysed in the following chapter.

4.1 Study area

In the northern suburbs of Milan lies the Bicocca district (Fig. 26b), which since 1998 hosts the university campus of University of Milano-Bicocca. Over the past century, the Bicocca district has undergone a profound transformation. For centuries it remained a rural area, structured around agricultural land and the fifteenth-century Arcimboldi villa. However, this condition changed radically in the early twentieth century, when major industries such as Breda and Pirelli established large manufacturing complexes in the area. In the 1990s, the

district experienced a major shift in land use, marking the emergence of one of Milan's principal cultural and academic hubs. This new direction was defined primarily by the construction of the Arcimboldi Theatre and the establishment of the University of Milano-Bicocca. The urban regeneration of the former industrial area was conceived and led by Gregotti Associati, whose design philosophy envisioned the district as a "Città di Pietra" ("City of Stone"; Nuvolati, 2018). As a result, both the neighbourhood and the university campus are characterised by a predominance of mineral, paved and impervious surfaces. Specifically, the eastern part of the neighbourhood has historically been predominantly commercial and industrial, with more recent development including the university campus and residential areas. On the other hand, the western part of the region is predominantly vegetated, a feature attributable to the presence of Parco Nord and residential areas.

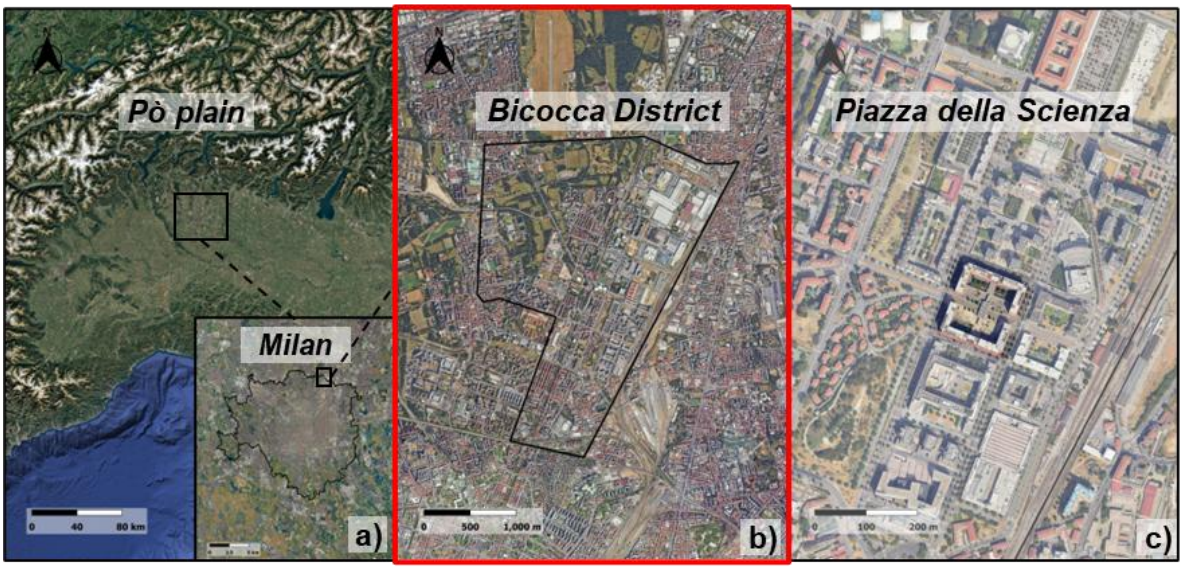

Fig. 26 Study area location Bicocca District. Placed in northern Italy and Milan a) there is Bicocca District b) and Piazza della Scienza (University campus square, c)

4.2 Spatio-temporal thermal characterization at district scale

The workflow follows the approach introduced at the macro scale and adapts it to a finer scale thermal characterization (See Chapter 3, Par. 3.2). In addition, to complement this analysis, near-surface air temperature was monitored at selected sites representing contrasting spatial configurations within the neighbourhood. As a first step, a qualitative, map-based inspection of Landsat-derived LST imagery was carried out over the designated study area (Fig. 27). This visual assessment enabled the identification of recurrent hotspots and comparatively cooler sectors within the Bicocca district, providing an initial indication of pronounced intra-district heterogeneity. The subsequent analysis is based on these qualitative observations.

Fig. 27 presents a qualitative illustration of the spatial heterogeneity of surface thermal conditions within the Bicocca district. The LST map is derived from the stack summer image (2013 to 2025), which has been clipped on to the study area. The procedures employed for the retrieval and pre-processing of satellite data are documented in the preceding chapter (See Chapter 3, Par 3.2.1), and the fundamental processing steps are briefly reviewed in the following methodological paragraph. Fig. 27a shows the district boundaries over an optical basemap, with dashed circles highlighting representative sub-areas. The corresponding LST field is displayed in (Fig. 27b), where near red colours delineate hotspots and near green colours identify cooler sectors within the same compact domain. The most evident hotspot is located in the eastern and north-eastern portion of the district, where extensive impervious and roofed surfaces dominate, producing persistently higher surface temperatures. It is evident that additional warm anomalies are present in other mineralised and built-up sectors across the district. Conversely, cooler patches emerge in areas where vegetation is more continuous and spatially aggregated, particularly in the western and north-western sector, associated with major green spaces. Fig. 27 (c–g) provide close-up views of selected areas and facilitate the visual interpretation of the thermal patterns. High LST values correspond to large industrial or commercial buildings and heavily paved surfaces, whereas lower LST values coincide with vegetated areas and, more generally, with surface configurations characterised by a higher fraction of permeable and shaded cover. Furthermore, the presence of liquid basins at the wastewater treatment plant is associated with a distinctly cooler surface thermal response compared to the surrounding built environment (Fig. 27d). The stack under

consideration supports the evidence that Bicocca does not behave as a thermally uniform district. Instead, distinct hotspots and cooler sectors coexist for short distances.

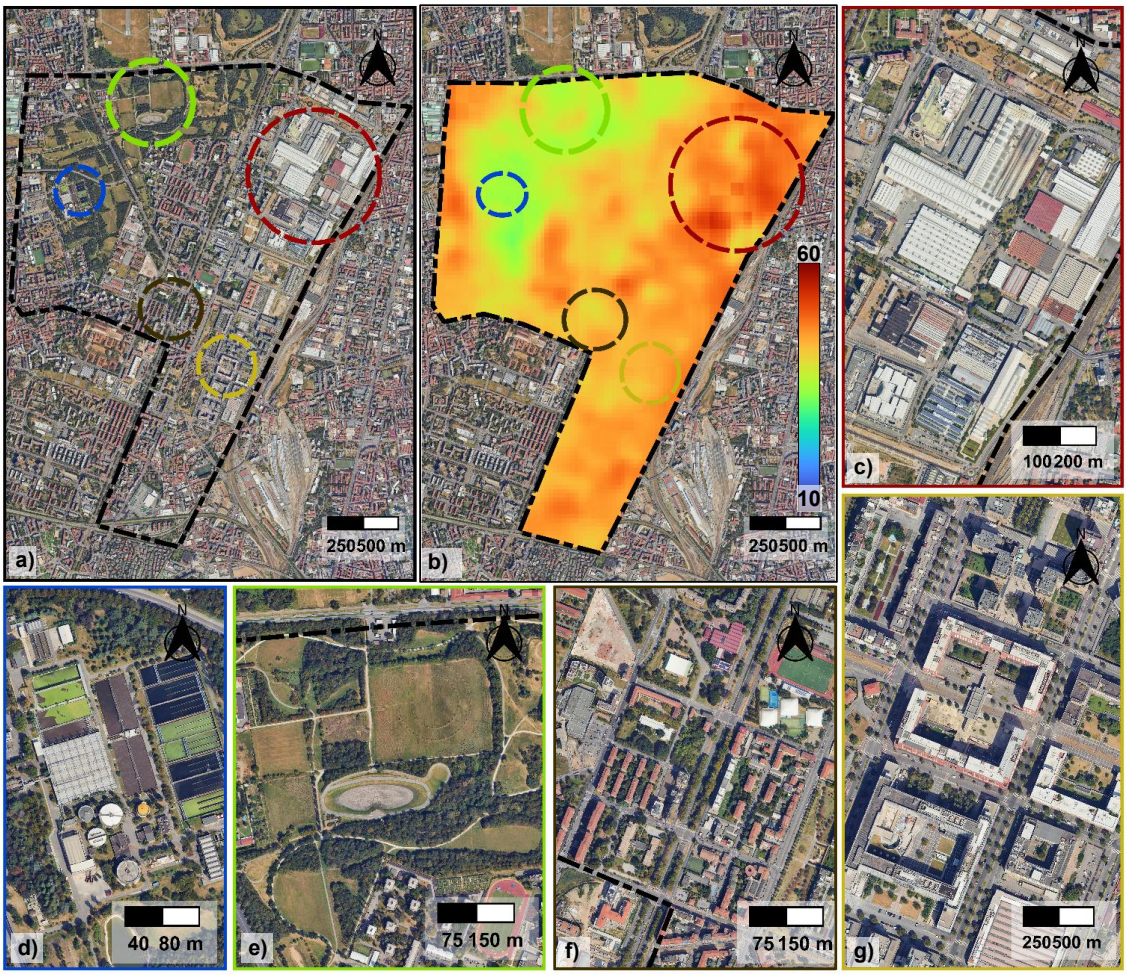

Fig. 27 District boundary over optical basemap with the locations of selected sub-areas a). Corresponding stack LST map highlighting hotspots and cooler sectors b). Focus on a highly impervious and industrial sector (hotspot, c). Focus on the wastewater treatment plant, including liquid basins d). Focus on a vegetated area e). Focus on a residential fabric f) Focus on the university campus area g).

4.2.1 Satellite and statistical analysis approach

The regional multipolygon DUSAF dataset has been cropped to the extent of the Bicocca neighbourhood, covering an area of 5.3 km^2. The study area is characterised by the presence of various Land Use/Land Cover units, which are classified into 26 distinct DUSAF categories.

Subsequently, a set of Landsat 8 satellite scenes was selected and their pixel values stacked for the purpose of deriving surface temperature and spectral information over the same area. From the image, land surface temperature was retrieved, while two spectral indices were computed: The Normalised Difference Vegetation Index (Rouse Jr, 1974; Tucker, 1979) employed as a proxy for vegetation presence and the Normalised Difference Built-Up Index Zha, 2003)Zha, 2003) utilised to characterise built-up and paved surfaces (Fig. 28b). The selection and processing of scenes was conducted utilising Google Earth Engine, employing standard cloud cover screening criteria (less than 5% over the area) and implementing radiometric scaling factors. Following this processing and the restriction of the dataset to the summer season (June–August), a total of 33 valid products were suitable for the analysis. The clipped DUSAF layer was then overlaid with the Landsat-derived raster. Pixel values of LST, NDVI and NDBI were extracted within each DUSAF polygon and subsequently grouped according to the 26 DUSAF Land Use/Land Cover categories, thereby producing class-specific distributions for each variable. For each distinct class sample, a set of descriptive statistics was derived (including median and interquartile ranges Q1 and Q3; for LST also minimum and maximum).

To this dataset, a Principal Component Analysis (PCA; Hotelling, 1933; Pearson, 1901) was applied (Fig. 28c) in order to reduce dimensionality and mitigate redundancy across indicators and summary statistics. As shown by the histogram in Fig. 28c, the first five principal components provide an adequate low-dimensional representation of the dataset, as indicated by the explained variance investigation. The resulting PCA scores were then subjected to clustering analysis using the K-means method (MacQueen, 1967). The number of clusters was selected to maximize physical interpretability and spatial coherence, with qualitative controls conducted within a Geographic Information System (GIS) environment. For the Bicocca district, the most significant partition corresponds to K = 4, resulting in four mesoscale thermos-oriented groups (Fig. 28d).

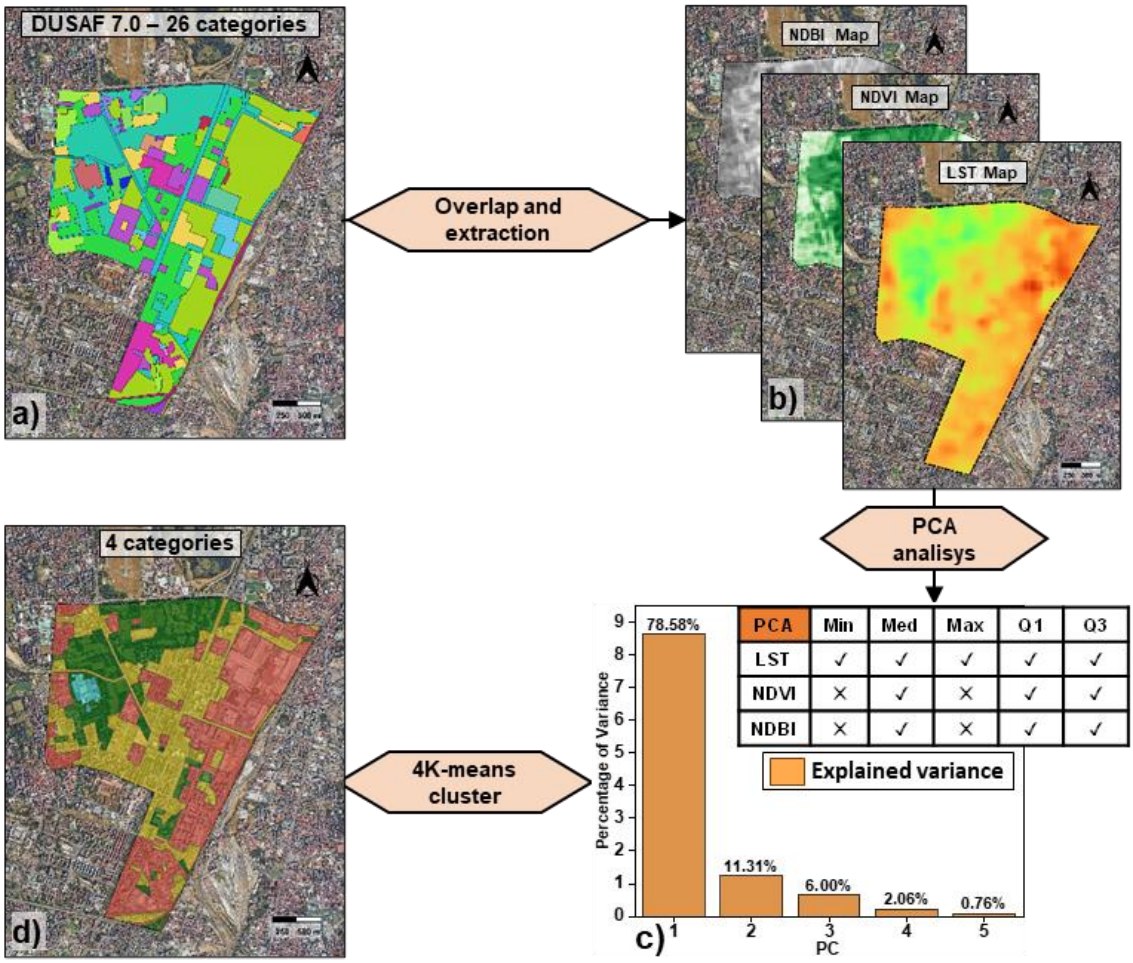

Fig. 28 Schematic process to obtain 4 thermo-spectral typologies. DUSAF7.0 polygon clipped on the study area a). LST, NDVI and NDBI maps clipped on the study area b). Statistics involved in PCA analysis and variance histogram c). Four categories as a result of the process d).

4.2.1.1 Surface thermal response characterization

The procedure of combined PCA and K-means analysis employed has generated four macro-typologies that have been nominated as Water, Vegetated, Mixed, and Paved (Fig. 28d). Their spatial distribution highlights a marked intra-district heterogeneity, with compact vegetated areas, strongly impervious sectors, and intermediate fabrics where impervious and vegetated elements coexist at fine scale. The derived classes are intended and interpreted as thermo-spectral typologies, i.e. groupings that summarise both spectral properties (NDVI and NDBI) and thermal response. Consequently, the LST patterns discussed below should be read as a characterisation of the obtained typologies.

For each group (Fig. 29, top left), LSTs have been extracted from the 33 Landsat8 products selected, and these have been summarised as boxplots to highlight their distribution within each class. Moreover, to provide a concise visual overview of the LST spatial patterns, six scenes (Fig. 29, labels 1-6) Fig. 1were selected from the full dataset of 33 images. The selection of these scenes had no impact on the results of the analysis, which were based on the entire dataset. However, it was chosen for illustrative purposes, as displaying all 33 scenes would have been superfluous and beyond the scope of this section. The selected scenes were distributed approximately every two years across the available time span. Furthermore, they were chosen within a similar period of the year to ensure temporal consistency in the visual comparison. The LST maps consistently highlight persistent hotspots in the eastern and north-eastern sectors, whereas lower surface temperatures are more frequently observed towards the northern and north-western portions of the district.

The boxplots (Fig. 29a-d) demonstrate stable thermal ordering among typologies when analysed across the multi-year sample. Water surfaces (Fig. 29a) have been found to be among the coolest typologies in median terms (32 to 48 °C), although their distributions can still shift upward during the hottest acquisitions, depending on the specific water-related infrastructure included in the class. Vegetated areas (Fig. 29b) typically exhibit a lower median LST in comparison to paved and mixed zones (generally ranging from 33 to 52 °C), characterised by a cooler distribution in less extreme conditions and partial convergence during periods of extreme heat. Mixed surfaces (Fig. 29c) occupy an intermediate position (38 to 53 °C). However, they demonstrate a larger dispersion, consistent with their compositional variability (impervious matrix with distributed vegetation). Paved surfaces (Fig. 29d) have been found to exhibit the highest median LST (40 to 55 °C), with upper tails that can reach 60 °C during the hottest scenes.

Focusing on the six representative scenes highlighted in Fig. 29 (labels 1-6), the median values obtained from the box plots indicate that: with a high thermal response (e.g., 25/07/2022, label 5), the median LST reaches 54 °C for Paved, 53 °C for Mixed, 51°C for Vegetated, and 47°C for Water, with Paved showing the most pronounced upper tail (up to 60 °C) and Vegetated area with the largest variability. Meanwhile, during a thermally milder acquisition (e.g., 19/07/2020, label 4), the median LSTs are lower and more separated, around 45 °C (Paved), 41-42 °C (Mixed). Temperatures of 39 °C and 36 °C were recorded in areas

with green vegetation and water bodies, respectively. An analysis of the median difference between surface types for the six representative images reveals a variation in temperature ranging from 2 to 7 °C, depending on the acquired thermal response, between the Paved and Vegetated areas. The contrast between the paved and water surfaces can be substantially greater, with a maximum observed difference of 19 °C in the selected scene from 2015.

During the warmest acquisition (25/07/2022, label 5), the types partially converge in median terms, however, Paved maintains the highest values and the upper tails remain more pronounced.

Finally, the dotted trend lines suggest an increase in the median LST over the course of the acquisition sequence for all categories. The ranges within which the LST varies for the individual categories are significantly different, with Water trending from 34.8 to 40.0 °C, Vegetated from 36.7 to 41.3 °C, Mixed from 40.7 to 44.7 °C, and Paved from 42.8 to 46.9°C. In consideration of the lack of uniformity in sampling over years and the dependence of LST on the specific weather conditions at the time of acquisition, this investigation is reported here as a descriptive trend rather than a formal trend attribution.

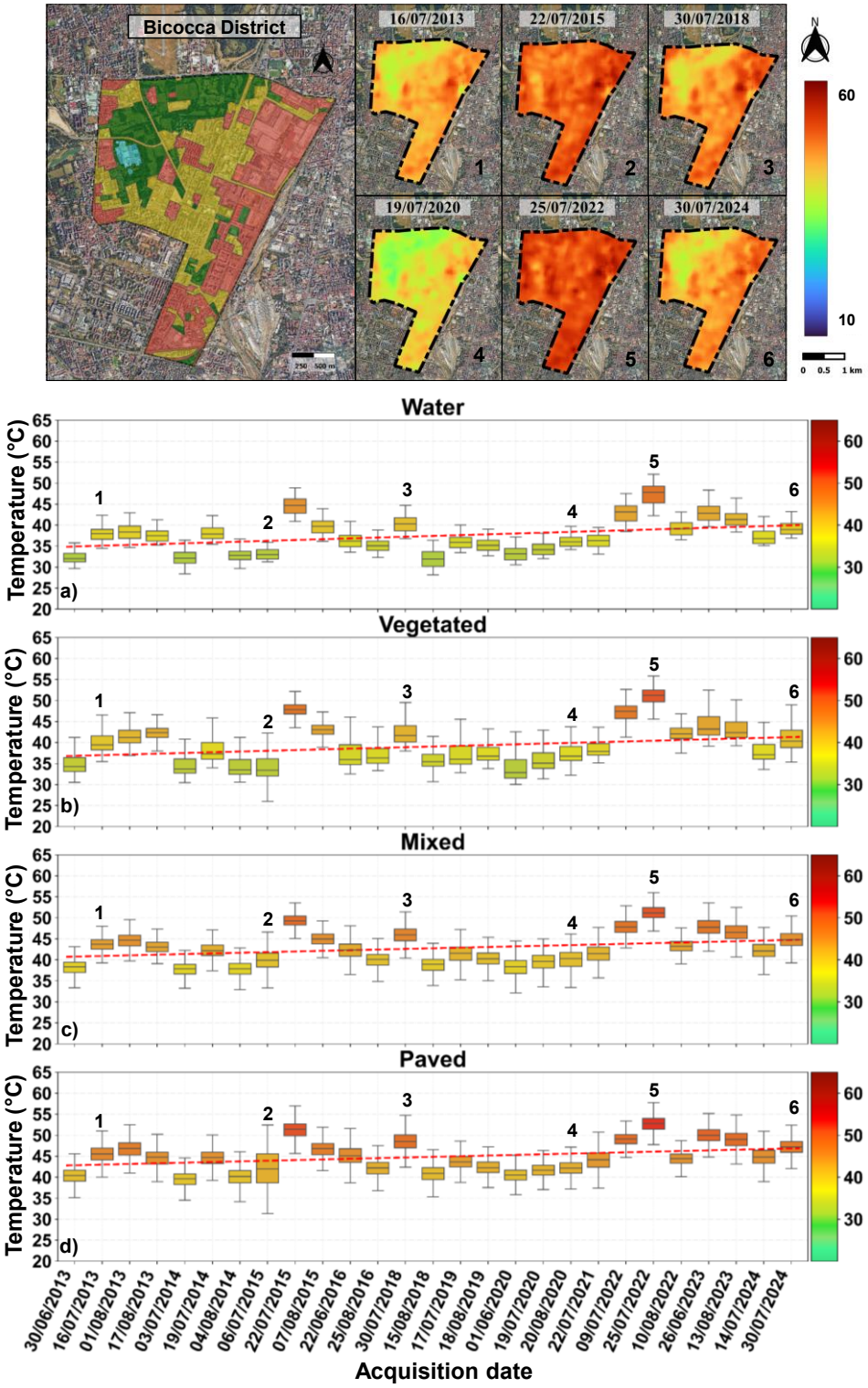

Fig. 29 The map shows the four polygons from which surface temperatures were extracted (top left). Examples of Landsat 8 LST maps for six representative summer acquisition dates (labelled 1-6, top right) are provided herewith. The boxplots of LST distributions were extracted from all available summer scenes (June-August; n = 33) and grouped into the four polygons (Water, Vegetated, Mixed, Paved; a-d). The dotted red line suggests a temporal trend.

In order to provide a complementary climatic context for the Landsat acquisitions, monthly near-surface air temperature data (Fig. 30) were retrieved for the same time window from three ARPA Lombardia meteorological stations located in the proximity of the Bicocca district: V. Feltre, V. Marche and Cinisello Balsamo Parco Nord (ID station 869, 501 and 147). The location of the stations varies, with some being situated in residential areas, specifically in the municipalities of Feltre and Marche, while others are located in vegetated areas, such as Parco Nord. The series demonstrates the anticipated seasonal cycle, characterised by consistent summer maxima and winter minima across all stations, with only a marginal long-term signal observed during the analysed period. It is notable that Marche has been observed to exhibit slightly higher summer peaks than the other stations, while Parco Nord typically shows lower peak values. This discrepancy is plausibly attributable to the contrasting local land-cover contexts around the stations. Although a slight upward tendency can be inferred, interannual variability remains dominant, and no robust trend attribution is attempted here.

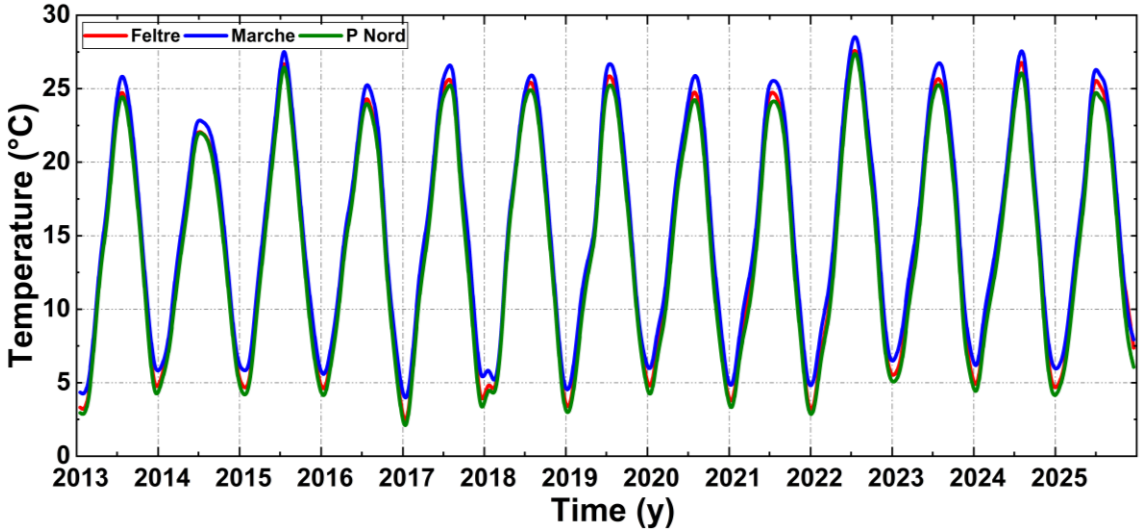

Fig. 30 Monthly near-surface air temperature time series for the period corresponding to the Landsat acquisition window (2013-2025). Data is derived from three ARPA Lombardia meteorological stations located in the vicinity of the Bicocca district. V. Feltre (ID 869), V. Marche (ID 501) and Cinisello Balsamo–Parco Nord (ID 147)

4.2.2 Air temperature monitoring in the Bicocca district

To complement the district scale remote sensing characterisation with air temperature measurements, four Onset HOBO MX2301A sensors (sensor details in the following chapter. See Chapter 5, Par. 5.1.2.2) were deployed at representative locations within the Bicocca district (Fig. 31). The monitoring span between October 2023 to December 2025. The selection of sites was driven by the necessity to include a range of contrasting land-cover settings, thereby ensuring a diverse and informative sample for the analysis. This approach was adopted to establish a foundation for interpreting local air temperature behaviour across the neighbourhood.

Specifically, the sensors were installed in: U6, a mixed setting characterised by extensive paved surfaces combined with planted trees (Fig. 31a); two in Piazza della Scienza (U2–U4; Fig. 31b), a predominantly paved public square that is the focus of the regeneration intervention and is analysed in detail in the following chapter; Vivaio Bicocca, a plant nursery used as a highly vegetated reference (Fig. 31c). Although the selection of monitoring sites was not informed by remote sensing results, they can be interpreted retrospectively within the context of mesoscale thermo-spectral types. This enables a qualitative comparison between surface thermal models and the behaviour of near-surface air temperature in contrasting urban contexts. Indeed, the three sites fall into distinct types previously identified: Piazza della Scienza (U2-U4) is representative of the Paved class, U6 of the Mixed class and Vivaio Bicocca of the Vegetated class. The mean monthly air temperatures (Fig. 31, right) demonstrate a consistent seasonal cycle across all sites, with the winter months exhibiting similarly low values and the late spring and summer months showing the greatest difference between locations. Due to the proximity of the sensors, a median has been calculated between the measurements obtained from the two sensors installed in Piazza della Scienza. This site has been found to demonstrate consistently elevated mean temperatures during the summer months, whilst the Vivaio Bicocca site has been observed to exhibit a tendency towards cooler conditions; the U6 site, by contrast, generally occupies a median position.

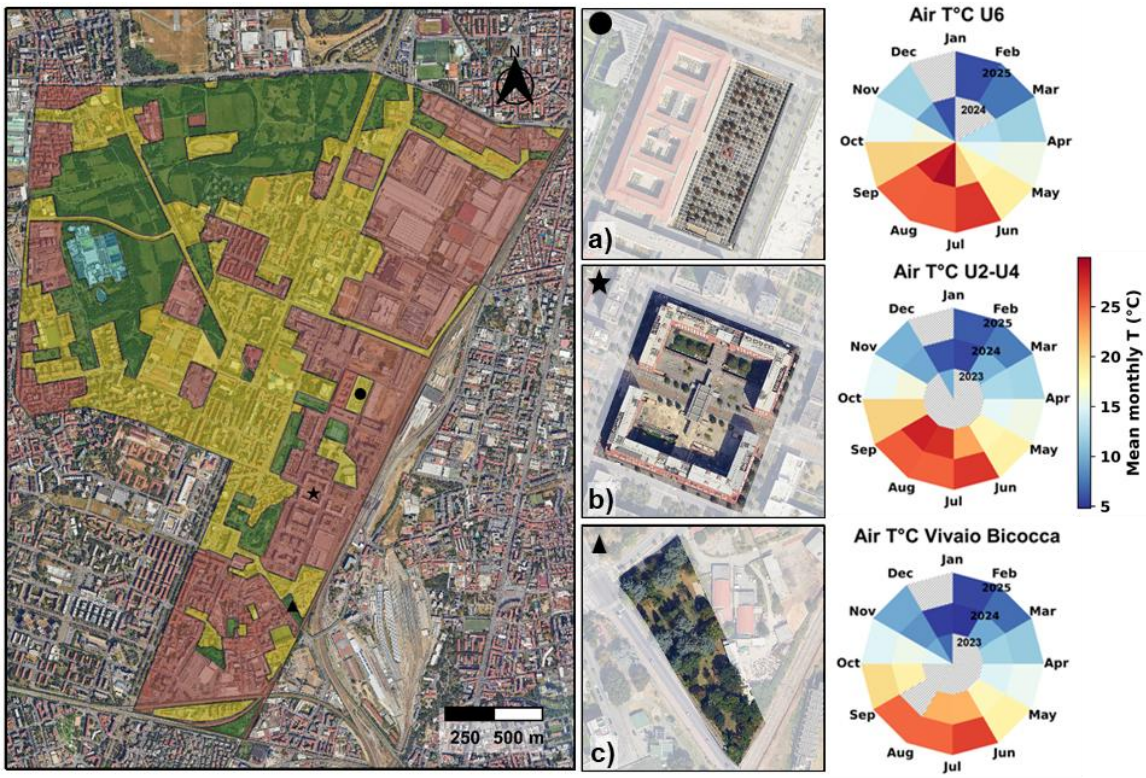

Fig. 31 Location and near-surface air temperature characterisation of the three monitoring sites in the Bicocca district (Left). Detailed orthophotos of the three sites: U6 a), two sensors in Piazza della Scienza (U2–U4; b) and Vivaio Bicocca c). Radial plots mean monthly air temperature (°C) at 3 m height for each site over the monitoring period (years indicated), highlighting the seasonal cycle and the systematic differences among sites (Right)

The analysis of the time series of the mean daily air temperature during the monitoring period (Fig. 32a) shows that the three locations follow similar seasonal and meteorological patterns, although there are minor yet systematic differences between them. A detailed analysis, with a particular focus on the summer of 2025 (Fig. 32b), when simultaneous measurements are available for all three locations, reveals that the variations become more pronounced during periods of high temperature. Temperatures during this period are consistently above 19 °C, with occasional readings reaching 32 °C. On multiple occasions during this period, the Vivaio Bicocca site has been observed to exhibit lower temperatures in comparison to the paved sites, within a range of 0.4 to 0.8 °C of difference. The location of U6 square is typically situated between the green and paved sites. During the most intense and protracted periods, there is intermittent partial convergence with the U2-U4 curve, indicating that local contrasts in average daily temperature may be diminished under conditions of intense atmospheric forcing in the two predominantly paved areas. However, the most significant disparities

between paved and vegetated sites tend to occur during periods of relatively low temperature, with fluctuations ranging from 20 to 26 °C.

In conclusion, the behaviour of the monitored air temperature is consistent with that observed among the previously constructed categories. The variations in surface types are reflected, although to a lesser extent, in the differences in air temperature at the three sites that were monitored.

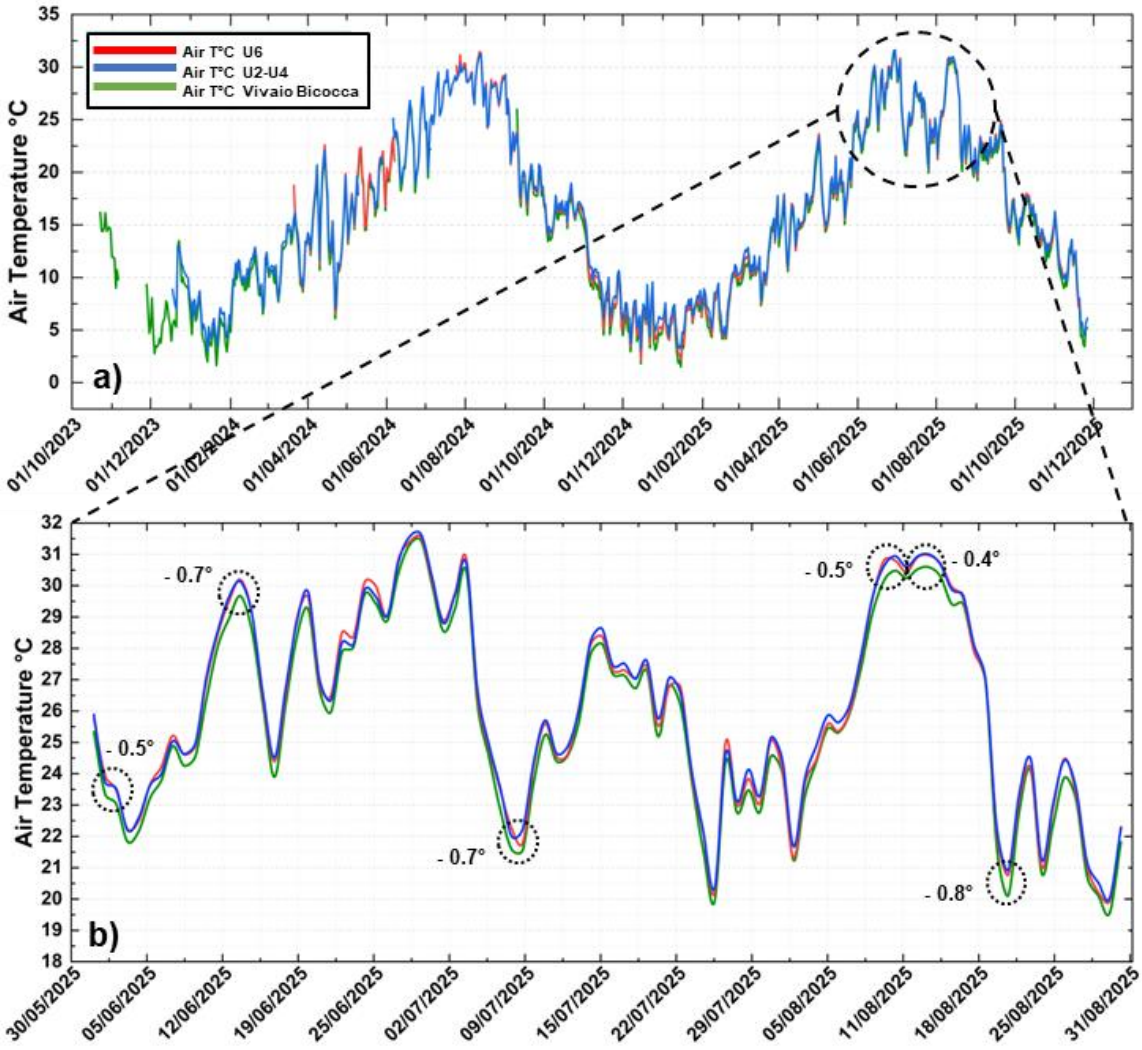

Fig. 32 Mean daily air temperature time series. Air temperature full record (October 2023 - December 2025; a), highlighting the common seasonal evolution and short-term meteorological variability across locations. Focus on summer period (June - August 2025, b)

4.3 Discussion and conclusion

The district scale analysis confirms that Bicocca exhibits a pronounced intra-urban thermal heterogeneity even within a relatively compact neighbourhood, indicating that urban overheating cannot be treated as spatially uniform when moving from the city background to the meso scale. This observation is consistent with the remote-sensing literature on surface urban heat islands, which documents significant heterogeneity in LST across urban areas, driven by variations in land cover, imperviousness and vegetation patterns, and urban form resulting in the occurrence of persistent hot spots and cooler (Puche et al., 2023; Zhou et al., 2019).

Based on this evidence, the classification workflow adopted aims to describe the spatio-temporal variability of thermal behaviour within the district using an approach based on satellite analysis and monitoring. The developed statistical process resulted in the classification of four surface types, which capture distinct thermal responses between acquisitions. The most significant and consistent contrast is observed between paved and vegetated surfaces, with a median LST difference of approximately 5-6 °C in the summer scenes analysed. This is comparable to the difference reported by Puche et al. (2023) between the hottest built-up and vegetated LCZs in Milan ($\Delta T°C = 6.7$). It is important to note that the heterogeneity observed is not only spatial but also temporal: the separation between classes is more evident during milder acquisitions and is partially reduced during warmer scenes, while preserving the overall thermal ranking.

Finally, the air temperature monitoring shows that the differences between sites are smaller than the LST contrasts yet remain systematic.

In this regard, Bicocca functions as a substantial experimental site on a mesoscale, and, notably, the context in which Piazza della Scienza is located. The latter is the subject of a detailed characterisation and microscale analysis of the impacts of regeneration in a predominantly paved environment.

Chapter 5

5 Microscale: Piazza della Scienza

In the context of urban regeneration, increasing the albedo of surfaces, depaving to increase soil permeability, and introducing vegetation or blue bodies (Oke, 2002) are key in mitigation process. Highly reflective materials are commonly considered to obtain “cool surfaces” for pavements and roofs (Giorio and Paparella, 2023). The impact of these solutions is twofold: they influence outdoor temperatures as well as indoor temperatures. Indeed, these solutions result in a decrease in the consumption of energy for the purpose of cooling, which consequently leads to a reduction in greenhouse gas emissions (Santamouris, 2020).

The mitigating effect of increased vegetation cover has been observed on both urban and local scales. Starting from the creation of city parks that form “Cool Islands” in cities, to street trees and vegetation applied to various surfaces either horizontally, ground and roofs or vertically such as building walls. It has been demonstrated that the efficacy of these solutions in reducing temperatures is attributable to three factors: evaporation, transpiration and shading (Han et al., 2023).

The efficacy of mitigation strategies is typically analysed during the design stage and validated during implementation through a combination of experimental observations and numerical simulations, which together provide a fundamental basis for assessing the potential of individual or combined interventions (Crank et al., 2018; Aleksandrowicz et al., 2023; Krayenhoff et al., 2021). Numerical simulations based on Computational Fluid Dynamics play a central role in representing and predicting urban climate processes, with different tools developed for mesoscale and microscale applications. Mesoscale analyses often rely on models such as the Weather Research and Forecasting model (Skamarock, 2024) the Urban Climate Map (UC-Map; Ng, 2015) or UrbClim (De Ridder et al., 2015) whereas microscale studies typically use SOLWEIG (Lindberg et al., 2008), RayMan (Matzarakis et al., 2007) or PALM-4U (Maronga et al., 2020; Lobaccaro et al., 2021; Vieira Zezzo et al., 2023). SOLWEIG efficiently estimates Mean Radiant Temperature (MRT) but has limited flexibility for complex or dynamic urban settings, while RayMan rapidly calculates MRT and comfort indices such as (Predicted Mean Vote) PMV and SET* (Standard Effective Temperature), using default parameterizations that reduce computational effort but at the cost

of lower spatial accuracy (Meng et al., 2025). PALM-4U, a LES-based system, is increasingly adopted for its ability to explicitly resolve turbulence and incorporate detailed urban-physics modules; however, its implementation requires extensive parameterization and substantial computational resources, which limits its applicability in real-world urban projects where many input data are difficult to quantify (Matzarakis et al., 2007; Vogel et al., 2022)

Among microscale models, ENVI-met (Bruse and Fleer, 1998) is considered one of the leading tools for fine-scale urban climate modelling (Lobaccaro et al., 2021). Its application has been employed in a wide range of climatic and urban contexts, including the Mediterranean Area and Italy. In Lombardy region in Italy, existing studies reflect these broader tendencies. Perini and Magliocco (2014) employed idealized block models driven by meteorological inputs representative of different Italian cities, while Ciacci et al. (2023) analysed the retrofitting of a single industrial building using a proxy structure due to limited local information. These contributions provide valuable insights but do not address ongoing regeneration processes or incorporate in-situ microclimatic measurements.

Despite the extensive use of field observations and numerical simulations in urban-climate research, a persistent gap remains between research assessments and real, feasible regeneration projects. Several studies rely on idealized scenarios, whereas interventions in dense urban fabrics are typically constrained by planning requirements, budgets and construction phasing. In such circumstances, the anticipated benefits may be negligible, thus necessitating the employment of optimization of mitigation solutions, in addition to the requirement for reliable, site-specific evidence to inform design decisions.

In this context, the present study combines dense, high-resolution environmental monitoring with microscale simulations to quantify the microclimatic effects of a real urban regeneration intervention. By examining a compact public space across different regeneration phases, the study assesses how changes in surface materials and vegetation establishment affect key microclimatic variables and outdoor thermal comfort. Furthermore, it discusses practical implications and limitations relevant to similar constrained projects.

5.1 Methodology

5.1.1 Microscale urban regeneration: Piazza della Scienza

Piazza della Scienza (Fig. 33, right), situated in the central-eastern sector of the Bicocca district, was constructed between 1990 and 2000. The square is framed by four university buildings hosting scientific departments, which together define a square layout. The C-shaped buildings are oriented approximately 21 degrees east of true north and extend over eight floors in total, with five above ground and three underground, reaching a height of approximately 32 m. The buildings are separated at their eastern and western ends to allow tram circulation along the east–west axis, while they are connected along the north–south axis by an elevated bridge beginning at the second floor. At each of its four corners, lowered courtyards located 4.5 m below street level contain limited green areas with grass and three mature trees per courtyard. These, together with twelve Magnolia trees along the tramway, constitute the only substantial vegetated elements within the square (Fig. 34). Indeed, the square consisted almost entirely of self-locking concrete pavers.

Since 2023, the square has been included in a new urban-regeneration project promoted by MUSA (Multilayered Urban Sustainability Action) initiative (part of the National Recovery and Resilience Plan - PNRR – Next Generation EU). Thus, Piazza della Scienza has been undergoing extensive urban regeneration since June 2023. Of the square's total surface of approximately 10000 m², the project currently covers about 8000 m², focusing exclusively on interventions at ground level.

The project involved the complete removal and replacement of the previous pavement with the introduction of new paving materials and landscaped areas composed of shrubs and trees. The new pavement includes gneiss cubes (Luserna stone) and granite slabs. The latter delineate the edges of the Luserna stone paving and form a continuous pedestrian path connecting the two newly created green spaces. The trees planted are mainly *Acer Campester* and *Acer Cissifolium*, deciduous trees that can reach heights of over 10 m with an oval, rounded crown (Nagy, 2004; Podaras, 1996), while the shrubs are various species that reach heights of 50 cm.

Since the initial phase of work commenced in June 2023, the existing pavement has been entirely removed, a process that was completed in September 2023. Concurrently, the new

paving was laid, starting from one quadrant at a time, with work concluding in September 2024.

This intervention, aimed at improving environmental, social and aesthetic conditions, also provides a valuable opportunity to test an integrated methodology combining on-site monitoring and microclimate modelling to support the design of UHI mitigation strategies within the broader framework of urban regeneration. Although the regeneration project had been defined prior to the start of this study, the ongoing transformation of Piazza della Scienza offers a unique opportunity to assess its microclimatic implications. The findings can inform future adjustments and complementary design actions, strengthening the development of climate-responsive strategies within the evolving regeneration process.

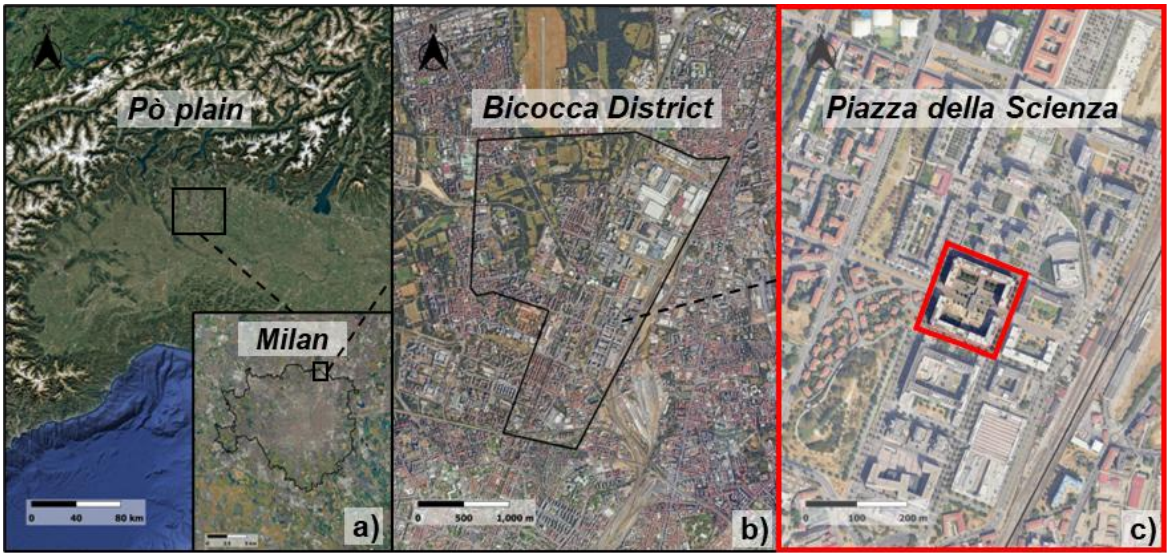

Fig. 33 Study area location Piazza della Scienza. a) northern Italy and Milan b) Bicocca District and c) Piazza della Scienza (45°30'48" N, 9°12'38" E) located in Bicocca District, Milan (Italy).

5.1.2 Experimental characterization and long-term monitoring

Since the present study aims at evaluating the impact of an urban regeneration project through a quantitative approach integrating monitoring data and numerical modelling, a microscale monitoring network was designed to evaluate the local expression of the Urban Heat Island and its forcing and controlling factors measure in space and time throughout the urban regeneration project (Fig. 34). To characterize UHI intensity, we measured both land surface temperature (T_{surf}) and near-surface air temperature (T_{air} at pedestrian height). These

variables are complemented by incoming solar radiation, relative humidity, and wind speed and direction, which act as forcing variables controlling the surface energy balance and represent the main input of the ENVI-met model. Finally, air temperature measured above roof level provides an upper boundary condition for the urban canopy layer and a reference for interpreting near-surface observations.

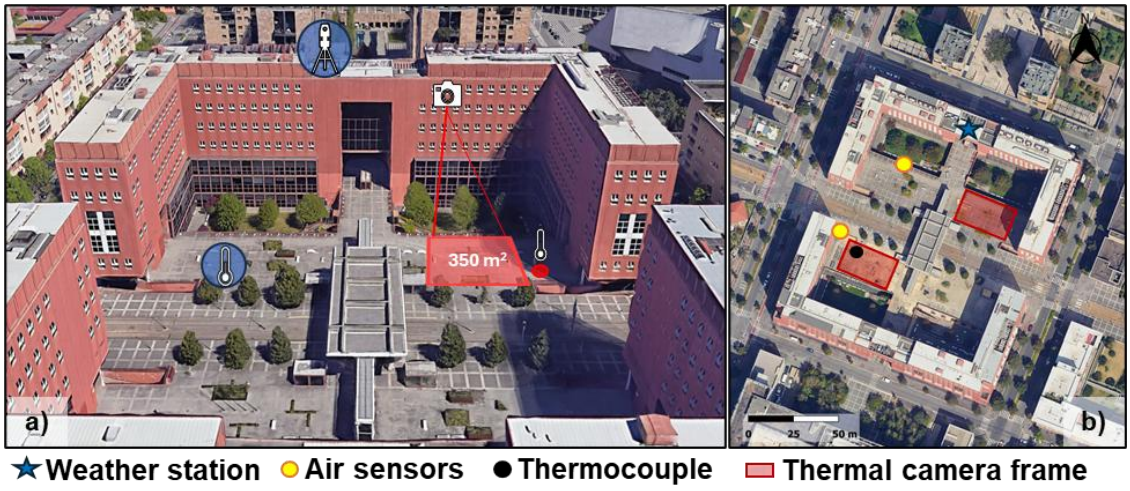

Fig. 34 Visual representation of the network of monitoring devices placed in Piazza della Scienza a). Thermal camera shots of the two diametrically opposite sides of the square (red rectangles) and layout of the air temperature sensors (yellow dots) and surface temperature sensors (black dot) b)

Fig. 34b shows the instrumentation position forming the field monitoring network, consisting of portable sensors strategically located across various points in the square. Throughout the regeneration process, the monitoring strategy followed a multi-temporal and multi-sensor approach (Fig. 35). Near surface air temperature was continuously recorded at fixed stations and with HOBO data loggers, providing long-term time series at selected locations. At daily and sub-daily scales, time-lapse InfraRed Thermography (Vollmer and Mollmann, 2008) was used to monitor T_{surf} over the study area. Furthermore, T_{surf} has been recorded with thermocouple fixed to the ground surface. The technical specifications of all instruments used are summarized in Table 4. This combination of measuring devices provided data with complementary temporal resolution and spatial coverage, which were jointly used to measure surface and air temperature, the relevant forcing variables, and the boundary conditions of the site. Fig. 35 reports spatial and temporal characteristics of various instruments involved.

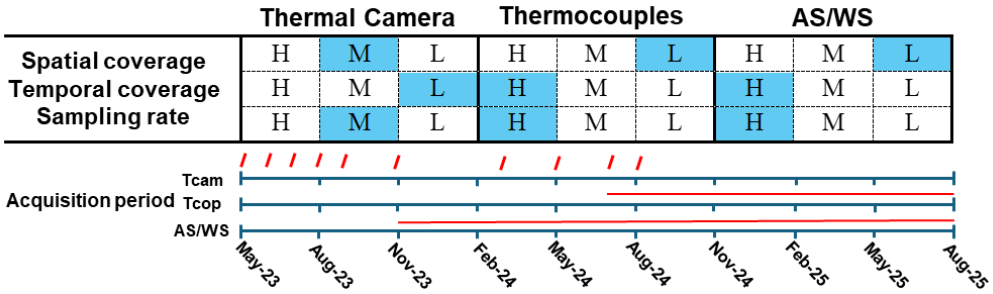

Fig. 35 Instruments' temporal and spatial coverage characteristics. H = High, M = Medium, L = Low

5.1.2.1 Material characterization

The square pre- and post-regeneration characteristics are defined by the presence of three distinct types of impermeable materials and permeable areas. Specifically, prior to the regeneration, the square was predominantly paved with interlocking concrete pavers (Fig. 39a), alongside small patches of permeable soil covered with grass. Following the intervention, the surface was replaced with Luserna stone cubes (Fig. 39b) and granite slabs (Fig. 39c). The latter are primarily distributed between two landscaped areas, creating a pedestrian path connecting them. These materials differ significantly in their thermophysical properties. When solar radiation reaches a surface, it is partially absorbed, transmitted, and reflected, depending on the optical and thermal properties of each material. The material properties that most directly influence transmission and absorption are surface albedo, thermal conductivity and volumetric heat capacity. A portion of the absorbed energy is eventually released as sensible heat. The fraction of energy not stored or transmitted depends on the surface's ability to reflect and emit radiation. The reflectivity of a material is described by its albedo, expressed as a value between 0 (fully absorbing) and 1 (fully reflective). High-albedo materials reduce heat storage and are thus associated with lower surface temperatures (Doulos et al., 2004; Tsoka et al., 2018). Emissivity refers to the ability of a material to release energy as thermal radiation into the atmosphere. This property ranges from 0 to 1, where 1 corresponds to a perfect emitter (a black body), and 0 indicates a fully reflective surface (Vollmer and Mollmann, 2008). Emissivity and broadband albedo of the materials were retrieved, utilising two different methods. Other properties, useful for the modelling, such as thermal conductivity and volumetric heat capacity, were adopted from the database of the software.

Surface Albedo

Broadband albedo (α) was derived from measurements obtained using a portable spectrometer (Fig. 36) and following the formulation proposed by Aoki et al. (2011).

$$\alpha = \frac{\int_{\lambda_1}^{\lambda_2} r(\lambda)F(\lambda)d\lambda}{\int_{\lambda_1}^{\lambda_2} F(\lambda)d\lambda}$$

Eq. [4]

where $r(\lambda)$ represents the spectral reflectance of the surface and $F(\lambda)$ is the incident spectral solar flux at the surface.

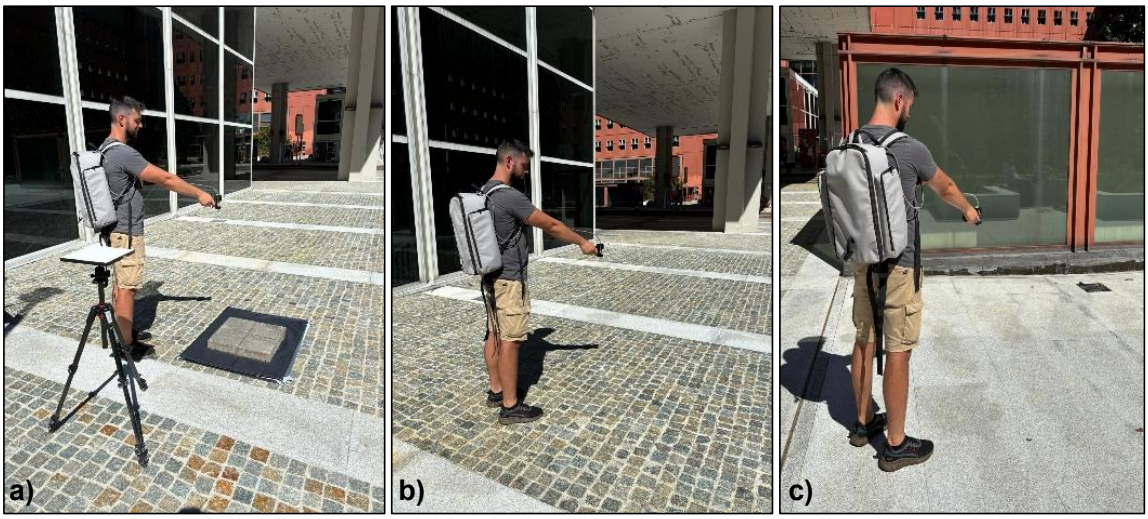

Fig. 36 Measurement of spectral radiance on samples of the paving that covered the square before the intervention a). The image also shows the white panel used as a reference for radiance

Field radiance measurements (Fig. 36) were collected on 26 September 2024 at 12 PM under clear sky conditions, using the Spectral Evolution SR-3500 (Haverhill, MA, USA), which covers the visible to shortwave infrared spectrum (300 – 2500nm). Spectral radiance measurements were obtained over the surfaces under investigation, including both newly installed and pre-existing pavement materials (Fig. 37). The granite spectral signatures (Fig. 37, orange) are the most elevated among the various surfaces, while the lowest are those of the old block pavers (Fig. 37, grey). This finding suggests a higher reflectance of granite and Luserna stone (Fig. 37, light blue) in comparison to the existing paving. Radiance data were referenced to a white calibration panel to derive surface reflectance, which was subsequently converted to broadband albedo following the previous formulation. Broadband albedo values

are 0.15, 0.25 and 0.47 for concrete Block-pavers, Luserna cubes and Granite slabs respectively.

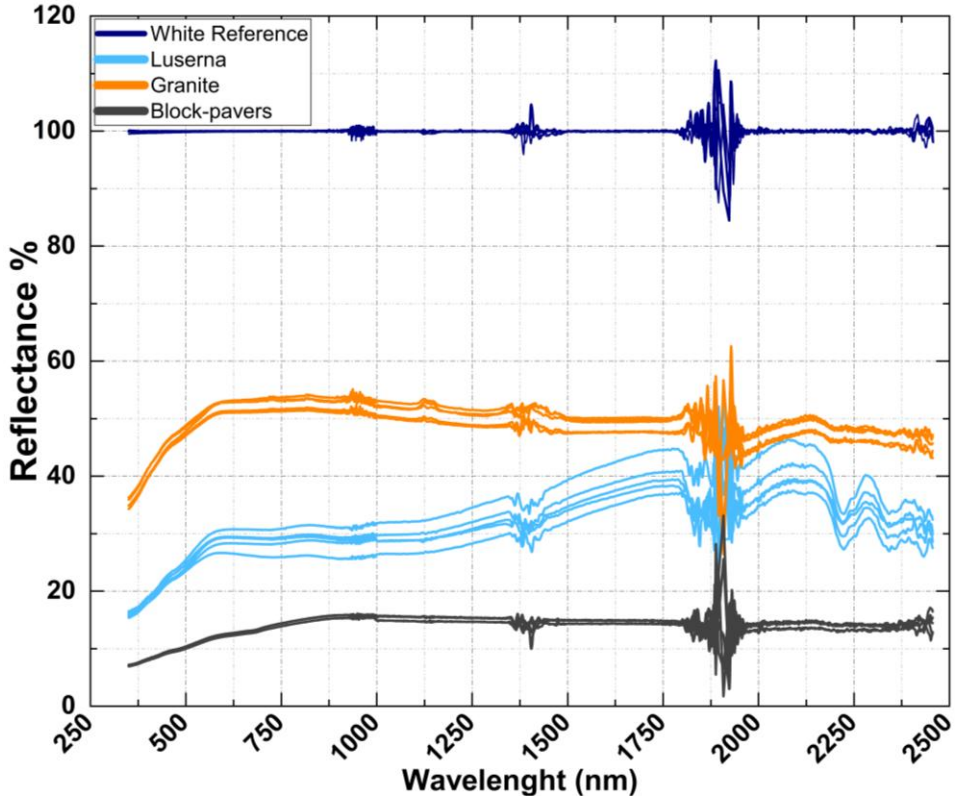

Fig. 37 Spectral signatures for the various impervious surfaces in the square, both those prior to intervention (grey) and those after intervention with Luserna stone (light blue) and granite (orange). The 100% curve (purple) represents the white reference panel for calculating broadband albedo.

Surface Emissivity

The surface emissivity was derived indirectly (Datcu et al., 2005; Vollmer and Mollmann, 2008; Mineo and Pappalardo, 2021) by using the FLIR T1020 thermal camera (Fig. 37d). Infrared thermography (IRT) is based on radiometry. A thermal camera does not directly measure the real surface temperature of the object (T_{obj}) in the frame; rather, it measures the infrared radiance that reaches its detector within a given spectral band. This radiance is then converted into an apparent temperature (T_{app}) through calibration. The physical basis of this conversion is blackbody radiation. Planck's law describes the spectral emission of an ideal blackbody as a function of wavelength and absolute temperature. This provides the reference model used in radiation thermometry (Vollmer and Mollmann, 2008).

In practical thermography, however, only a portion of the spectrum is detected, meaning the measured signal corresponds to band-integrated radiance rather than full-spectrum emission. For many building- and urban-scale applications, surfaces can be approximated as opaque grey bodies (Vollmer and Mollmann, 2008). In this case, the emitted radiant exitance (M_{obj}) is commonly summarized by the Stefan–Boltzmann law:

$$M = \sigma T^4.$$

Eq. [5]

However, the camera receives not only the object's emission, but also a reflected contribution (M_{refl}) from the surroundings. The magnitude of this contribution is controlled by the surface emissivity ε (with reflectivity r = 1 − ε). This apparent reflected temperature is a key input for radiometric correction. Neglecting atmospheric attenuation and measuring a surrounding temperature (T_{env}), the recorded signal (M_{rec}) can be idealized as (Fig. 38):

$$M_{rec} = M_{obj} + M_{refl} \Rightarrow \sigma T_{app}^4 = \varepsilon \sigma T_{obj}^4 + (1 - \varepsilon)\sigma T_{env}^4$$

Eq. [6]

which yields the following relation:

$$T_{app} = \left(\varepsilon T_{obj}^4 + (1 - \varepsilon) T_{env}^4\right)^{1/4}.$$

Eq. [7]

Rearranging to estimate the true object temperature gives:

$$T_{obj} = \left(\frac{1}{\varepsilon} T_{app}^4 + \left(1 - \frac{1}{\varepsilon}\right) T_{env}^4\right)^{1/4}.$$

Eq. [8]

In real measurements, the radiometric chain is further affected by atmospheric transmittance and path radiance; therefore, accurate temperature retrieval requires at least ε, reflected apparent temperature and T air (Vollmer and Mollmann, 2008).

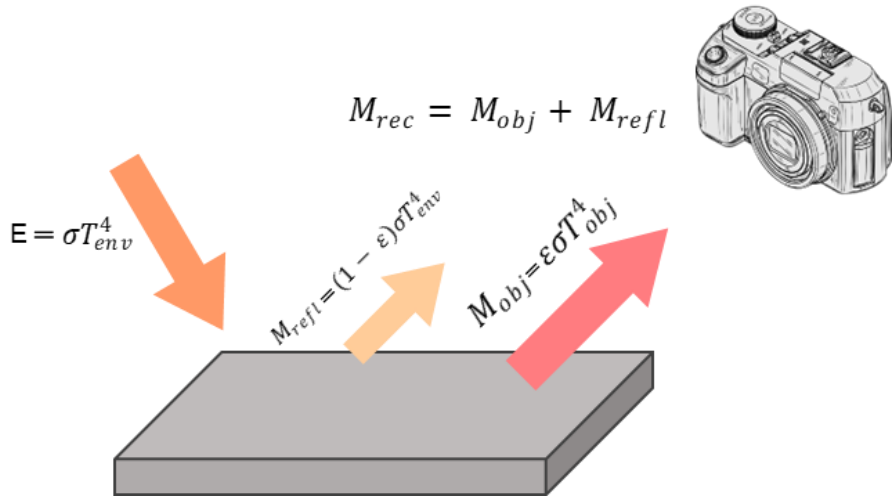

Fig. 38 Schematic representation of how the signal is recorded by the thermalcamera (E represents the environmental irradiance)

For surface emissivity retrieval, three representative surface samples, corresponding to the different types of impermeable materials in the square, were analyzed. Each sample was heated in a laboratory oven to a known temperature of 70 °C. A piece of black insulating tape with known emissivity of 0.97 (Mineo and Pappalardo, 2021) was applied to the surface of each sample. By comparing the measured radiative temperatures of the samples with the reference tape, and adjusting for ambient and reflected temperatures, the emissivity of each material was determined.

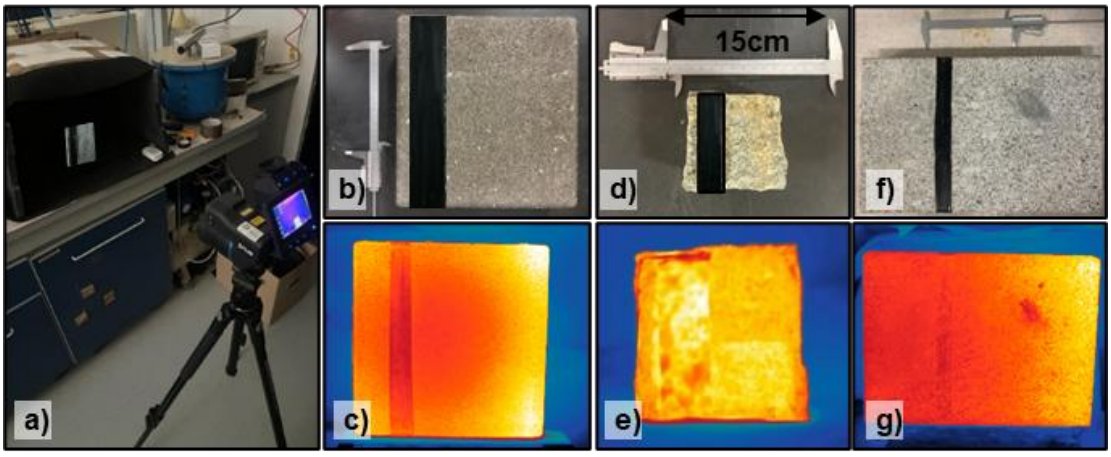

Fig. 39 Thermalcamera and sample placed in a laboratory at a controlled temperature and protected from light a). Old pavement material, interlocking concrete block-pavers b) and corresponding thermal image c). New pavement material, Luserna cubes d) and corresponding thermal image g)

5.1.2.2 Meteo-climatic variables

A Davis Vantage Pro2 weather station (WS) was employed to record environmental atmospheric parameters. The instrument is located on the roof of the university building, at an elevation of 32 meters (Fig. 34). The Integrated Sensor Suite (ISS) measures air temperature (T_{air}, °C), Relative Humidity (RH, %), wind speed (m/s), wind direction (deg) and Global Horizontal Solar Radiation (GHI, W/m2). The sensor has been installed since June 2022 and acquires data every ten minutes. Additionally, two Onset HOBO MX2301A dataloggers were installed to monitor Ta and RH. The sensors were positioned at a height of 3m above ground (Fig. 34- yellow dots) and equipped with radiation shields to prevent direct solar exposure from affecting the accuracy of the readings. In accordance with WS data, the sensors have been collecting data at 10-minute intervals since November 2023. The technical specifications of all instruments used are summarized in Table 4.

5.1.2.3 Surface temperature

Surface temperature was measured using IRT technique, specifically with a FLIR T1020 thermal camera operating in the 7.5-14um spectral range. The camera was positioned on the fourth floor of the university building at an elevation of 28 m to capture thermal images of a portion of the square, at an angle as close to nadir to the ground as possible (Fig. 34 – red areas). The field of view was maintained at a static position, thereby encompassing a single, representative sector of the square (U2), capturing area corresponds to approximately 350 m², within which all target surface types were present concurrently. This methodological approach facilitated a consistent comparison of materials acquired within the same session. The acquisition of images was conducted over the course of several months, from June 2023 to August 2024. Specifically, the images were collected at frequency of 20 minutes over 24-hour periods, to document both diurnal heating and nocturnal cooling phases, for a total of 10 acquisitions in 10 months.

Radiometric parameters were set to retrieve surface temperature from the recorded signal. The previously derived emissivity values for each surface class were adopted for the corresponding areas in the thermal images. The reflected apparent temperature was estimated in situ using a highly reflective aluminium reference panel placed within the scene. Given its very low emissivity, the panel acts as a near-mirror in the LWIR (Long-Wave InfraRed, range

8-14μm; (Vollmer and Mollmann, 2008), so its measured radiometric temperature was used as a proxy for the surrounding reflected contribution. Finally, air temperature and relative humidity were obtained from the sensors that had been deployed at ground level in the square. Furthermore, a T-type sensor was installed on a HOBO UX120-014M datalogger within the thermal camera frame (Fig. 34; black dot). The contact measurements were obtained during the first week of July 2024 and employed to validate the data acquired by the thermal camera. As demonstrated in Fig. 40, a robust correlation exists (RMSE = 1.35, MAE = 0.9) between the data obtained directly by the thermocouple and the indirect data obtained by the thermal camera. This positive correlation serves to strengthen the thermal camera data, which was subsequently utilized to validate the model outputs. The technical specifications of all instruments used are summarized in Table 4.

Table 4
Air temperature and Surface temperature instruments specifications.

FLIR T1020 thermal camera	
Spectral range	7.5 to 14 μm
Operating range	- 40 to + 50°C
T_{surf} Accuracy	± 1 °C
T_{surf} Sensitivity	0.02°C
Onset HOBO - UX120-014M / Type-T Thermocouple	
T_{surf} Sensitivity	0.02°C
Operating range	-20° to 70°C
T_{surf} accuracy	±0.6°C / ±1,0°C
Weather Station Davis Vantage Pro2	
T_a/RH Resolution	0,1°C / 1%
Wind speed/direction Resolution	0.1 m/sec / 1°
Operating range	-40 to +65°C
T_a/RH accuracy	0,5°C / 3%
Wind speed/direction accuracy	1 m/s / 3°
Onset HOBO - MX2301A	
T_a/RH Resolution	0.02°C / 0.01%
Operating range	-40° to 70°C
T_a/RH accuracy	± 0.25°C / ± 2.5%

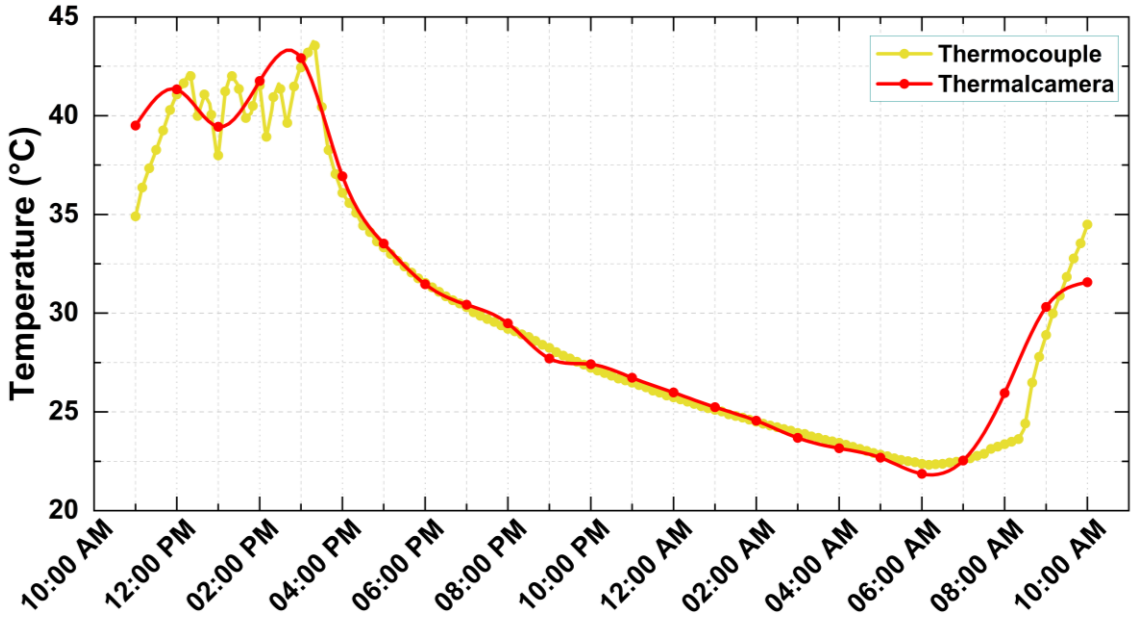

Fig. 40 Comparison between thermal imaging camera and thermocouple data over a day (26 July 2024)

5.1.2.4 Vertical Tair profiles: drone-based approach

To characterize the vertical structure of near-surface atmospheric conditions over Piazza della Scienza, dedicated field campaigns were carried out to acquire vertical profiles of air temperature and relative humidity using an approach based on UAV (Unmanned Aerial Vehicle). Although the microscale monitoring strategy was primarily designed to support and interpret the modelling framework, these profiles are reported here because they were collected within the same experimental setting and provide complementary information on vertical stratification that cannot be captured by fixed sensors alone.

The measurements were conducted utilizing an iMet-XQ2 package (International Met Systems) mounted on a DJI Mavic Pro UAV (Fig. 41a). The iMet-XQ2 is equipped with a PTU sensor suite, which incorporates sensors for air temperature, relative humidity, and barometric pressure. Additionally, it fits with a GNSS module. The data are sampled at a rate of 1 Hz and include timestamps to the second, together with GNSS coordinates and GNSS altitude above mean sea level (MSL). The vertical profiling procedure comprised three repeated ascents and three repeated descents from two take-off locations (Fig. 41b) within the square, each with a nadir to ground angle.

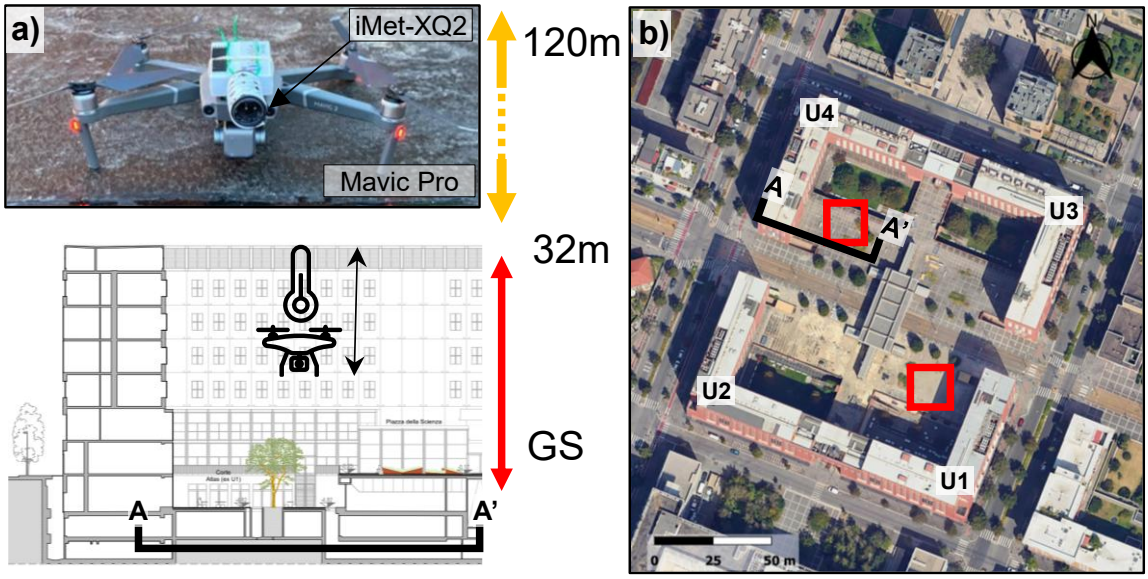

Fig. 41 Mavic Pro used for flights with the iMet-XQ2 sensor mounted on top a). The red squares on the square indicate the drone's take-off points b). GS = Ground Surface

Each profile followed a vertical trajectory up to the regulatory limit of 120 m above ground level, with a vertical speed of approximately 1m/s, resulting in a profiling time of approximately 120 seconds per ascent (and a comparable duration for the descent). The selected vertical speed represents an operational compromise between flight stability and sampling density. Since the sensor logs at 1 Hz, an ascent at 1m/s results in an effective vertical resolution of approximately one measurement per meter.

To facilitate profile reconstruction, the 1s timestamps provided by the iMet-XQ2 were utilized to align each Tair and RH sample to the corresponding flight time. Utilising a methodical approach with regulated vertical velocity ensured the consistent allocation of $T_{air}(z)$ and RH(z) throughout the ascension and descent phases. In order to ensure consistency between profiles, GNSS altitude (MSL) and barometric pressure were maintained as verification variables. All flights were conducted between 12 PM and 1 PM under sunny conditions and with weak winds to maximize repeatability and to sample the vertical structure during the central hours of daytime heating. A total of three acquisition campaigns were conducted between November 2023 and August 2024, capturing vertical profiles under diverse seasonal and meteorological conditions. Table 5 reports the specification of the iMet-XQ2 sensor.

Table 5
iMet-XQ2 sensor specification

Component	Range	Resolution	Response time	Accuracy
Temperature	-95 to 50 °C	0.01 °C	< 1 s, 5 m /s	±0.3 °C
Relative humidity	0–100%	0.1%	0.6 s, 25 °C	±5% RH
Pressure	1200–10 hPa	0.02 hPa	< 1 s	±1.5 hPa
GNSS	40 km / altitude res. 0.01 m	0.01 m	1 s update	Horizontal 8 m; vertical 12 m

In the May campaign (27 May 2024), the three repeated soundings collected at both take-off locations (U1 and U4, Fig. 42 and Fig. 43 respectively) show a similar temperature range and a clear difference between ascents and descents. T_{air} (solid lines) ranges approximately between 21 and 24 °C across all profiles. As observed in the ascents presented in Fig. 42a and Fig. 43a, there is a general decrease in temperature with height, with the most pronounced gradient evident in the third ascent at U1, where T_{air} exhibits a decrease from 23.3 °C at the surface to 21 °C at 120 m height. A comparable vertical structure is reflected in the humidity field (dashed lines), with RH ranging approximately between 36% and 48% and exhibiting a tendency to vary in a consistent manner with the temperature decrease along the ascent.

Conversely, the descent profiles (Fig. 42b and Fig. 43b) manifest a marked overall smoothness and regularity, exhibiting diminished short-scale fluctuations even in lowest part of the flight. The vertical gradient remains evident during descent, with the most pronounced case corresponding to the descent profile, which shows a decrease from 24 °C near the surface to about 21 °C at the top of the profile. It is evident that the ascending legs are more susceptible to short-term variability and fluctuations in the lower layer, while the descending legs offer a more precise representation of the mean vertical structure for this campaign.

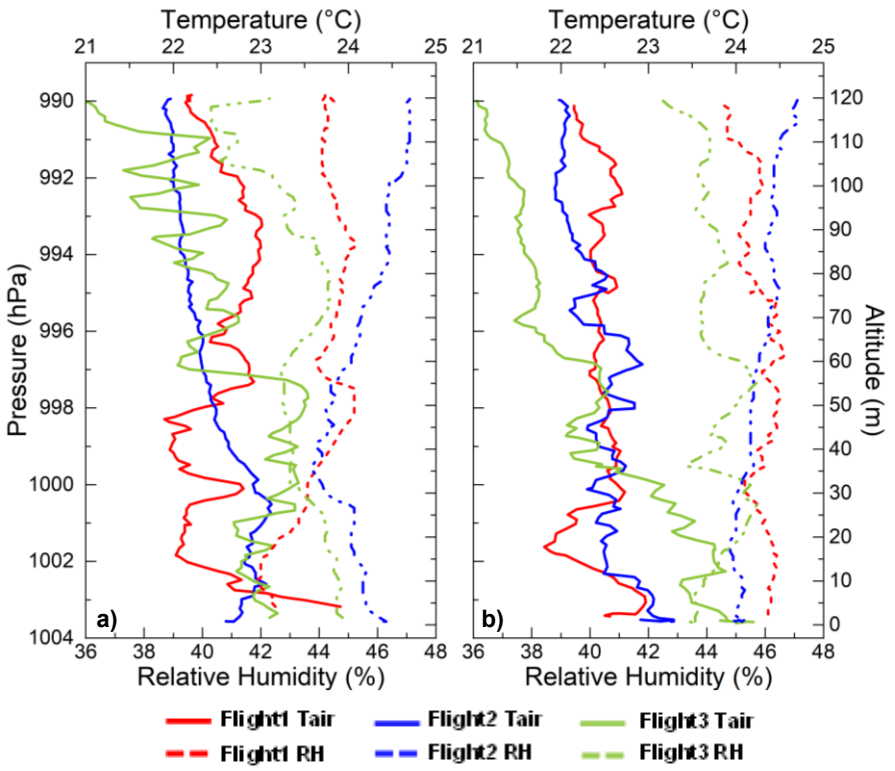

Fig. 42 Upward flights departing from quadrant U1 a) and corresponding downward flights b) on 27 May 2024

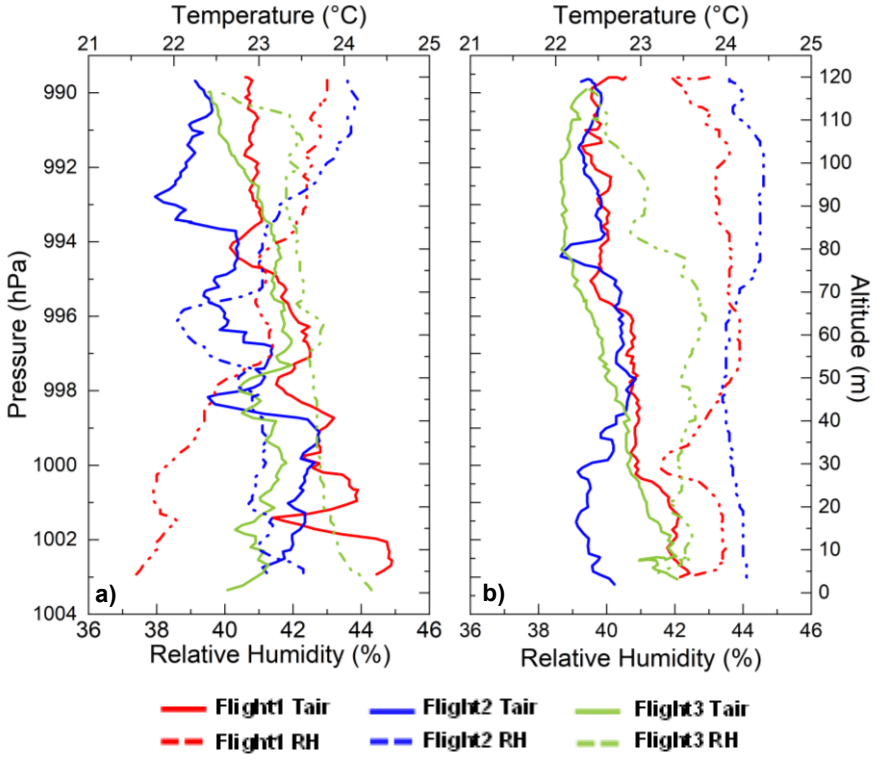

Fig. 43 Upward flights departing from quadrant U4 a) and corresponding downward flights b) on 27 May 2024

The June campaign (02 June 2024) was distinguished by significantly elevated temperatures in comparison with May. The range of air temperature was between 27 to 32 °C, while relative humidity remained predominantly within the range from 32 to 44%. During the ascending flights at both U1 (Fig. 44a) and U4 (Fig. 45a), a general decrease in temperature with height up to 120m is observed. However, the profiles demonstrate increased variability in the lowest part of the sounding (a phenomenon more pronounced at U1; Fig. 44). The relative humidity is observed to vary in a coherent manner with the thermal structure, exhibiting a tendency to be slightly higher in the upper atmosphere.

During the descending flights (U1, Fig. 44b; U4, Fig. 45b), the profiles appear to be more regular and smoother, with fewer abrupt oscillations even at low altitudes. Consequently, the vertical thermal gradient is more readily identifiable, and the decrease in temperature with height is more consistently expressed across repetitions. Relative humidity shows a comparatively gradual vertical variation, consistent with the more stable structure observed during the descents.

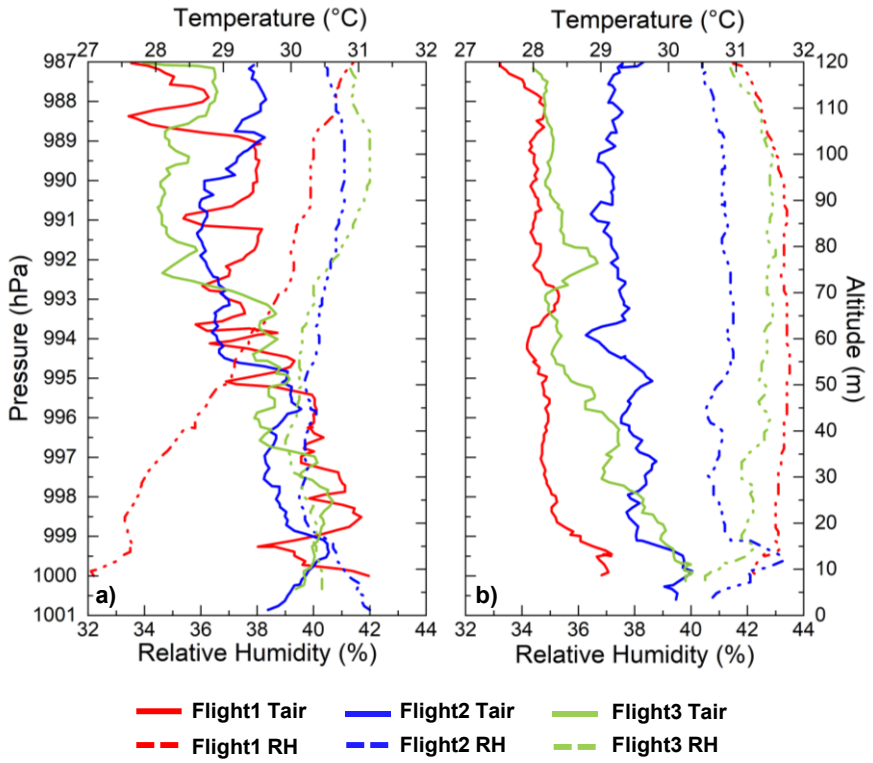

Fig. 44 Upward flights departing from quadrant U1 a) and corresponding downward flights b) on 02 June 2024

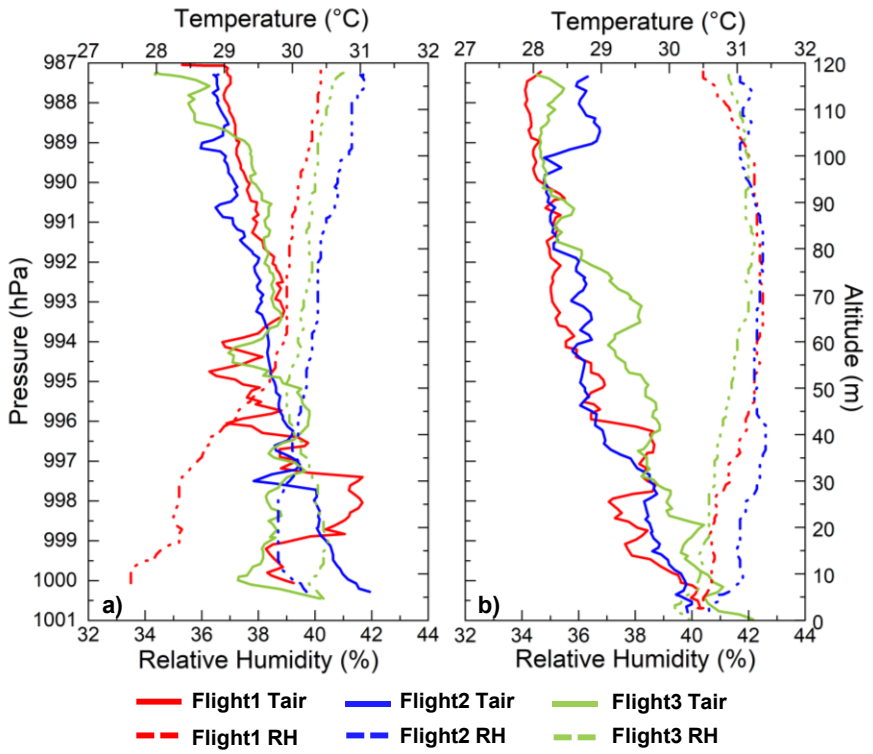

Fig. 45 Upward flights departing from quadrant U4 a) and corresponding downward flights b) on 02 June 2024

On 7 August, air temperature is observed to range from 29 to 33°C, while the relative humidity is situated within the range of 42% to 49%. As shown in Fig. 45a and Fig. 46a, a systematic decrease in temperature with height is observed during the ascending flights. Along the first meters of the track, temperatures typically range from 31 to 32°C. However, at height of 120 m, temperature was 30°C, indicating an overall decrease of 1 to 2°C across the atmosphere column. The range of RH is comparatively narrow, and there is only modest vertical variability, with a tendency toward slightly higher values in the upper atmosphere. During the descending flights (Fig. 45b and Fig. 46b), the profiles are found to be smoother and more repeatable, with reduced short-scale oscillations when compared with the corresponding ascents. Reduced dispersion, particularly at lower altitudes, facilitates the identification of the vertical gradient.

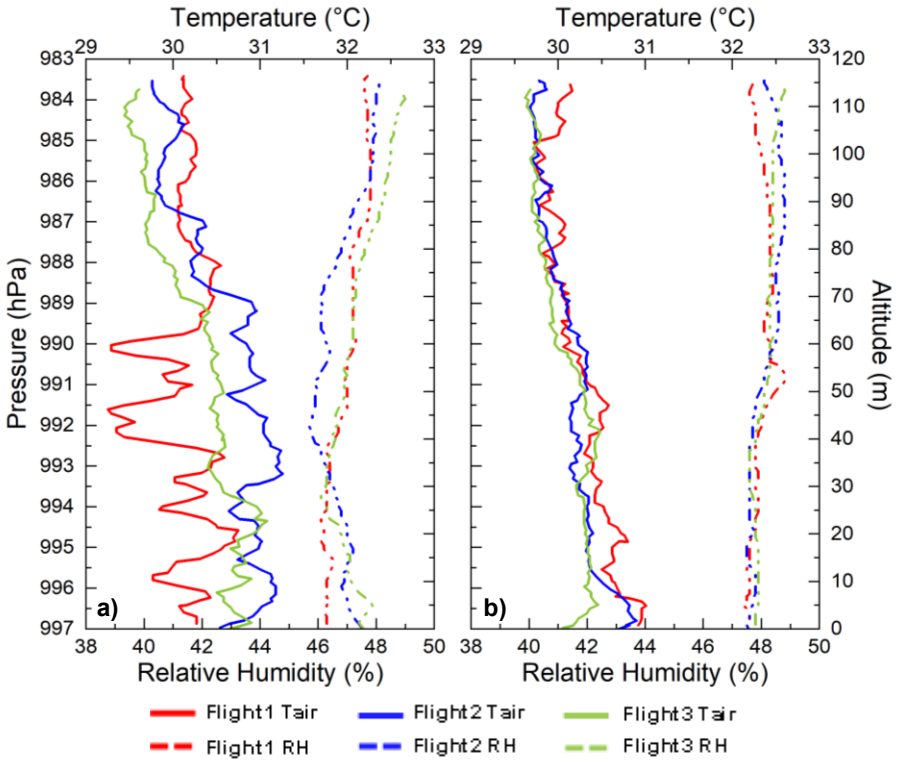

Fig. 46 Upward flights departing from quadrant U1 a) and corresponding downward flights b) on 07 August 2024

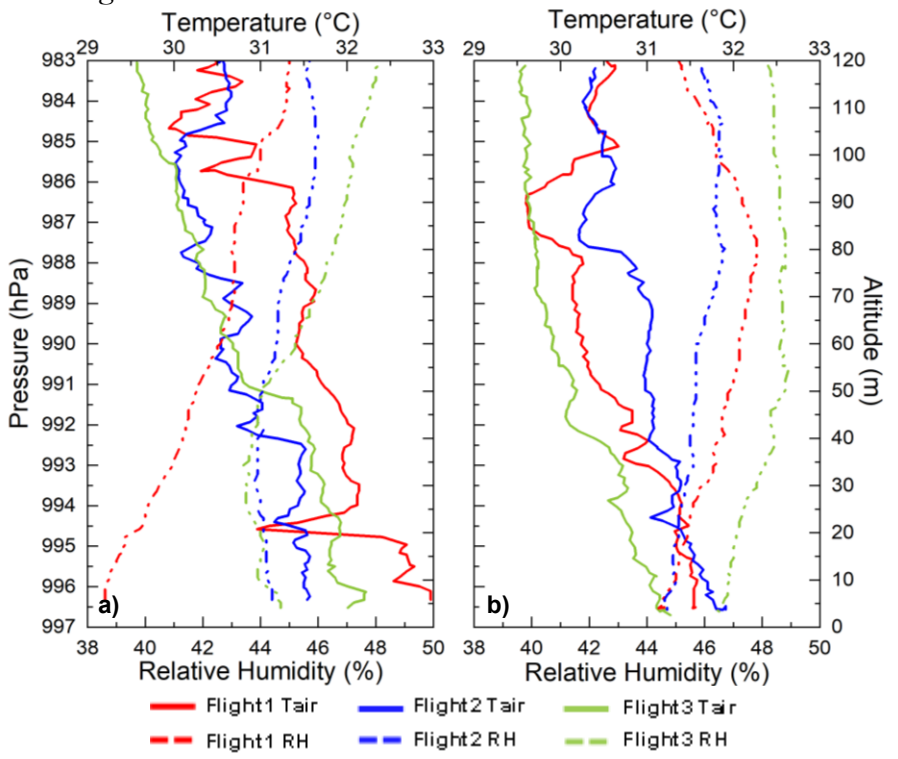

Fig. 47 Upward flights departing from quadrant U4 a) and corresponding downward flights b) on 07 August 2024

In the three campaigns, measurements taken using UAV consistently show greater variability in the lower part of the sampled layer, while a less disturbed structure emerges at higher altitudes. In all cases, a decrease in air temperature with height is evident, with a vertical gradient that is more readily identifiable above the most irregular segment of the profiles near the surface. This phenomenon is typically observed at an altitude of 60 m, which corresponds to approximately twice the height of the buildings in the square. A systematic difference between flight phases is also observed: descents are generally smoother than the corresponding ascents, providing a clearer representation of the average vertical structure. Overall, seasonal progression is characterized by a shift in the thermodynamic range, with warmer profiles observed in summer. Additionally, the persistence of greater dispersion near the surface remains a common feature across all dates. This behaviour is likely attributable to the combined effect of surface-induced instability and turbulent vortices (Bailey et al., 2020).

5.1.3 Numerical model

Numerical simulations were performed to evaluate the microclimatic conditions of Piazza della Scienza using ENVI-met (Bruse and Fleer, 1998), a widely recognized and validated model for urban environmental analysis (Toparlar et al., 2017; Tsoka et al., 2018). ENVI-met is a three-dimensional, non-hydrostatic model that adopts a holistic approach to simulate the interactions between atmospheric processes, soil, vegetation, and built structures.

ENVI-met software includes several modules to manage projects, generate the model domain, set simulation parameters, execute runs, and visualize results. Additionally, the input of material properties and three-dimensional vegetation characteristics is carried out through dedicated modules (Bruse, 2004). A one-dimensional (1D) component extends from ground level up to 2500 m and is used to apply boundary conditions to the primary three-dimensional (3D) model. Additionally, a 1D/3D soil model is included. At the core of ENVI-met is the atmospheric module, which solves the Reynolds-averaged, non-hydrostatic Navier–Stokes equations using Computational Fluid Dynamics (CFD) techniques and combines sub-models to calculate the other variables as air temperature and humidity, turbulence and radiative fluxes (Huttner, 2012). The typical horizontal resolution in simulation is 1 to 10m with a typical simulated time interval of 1-5 days (envi-met.com). This tool was selected in this

study due to its capability to simulate micro- and neighbourhood-scale processes (Detommaso et al., 2021), its comparatively user-friendly interface and the generally accessible nature of its input data.

5.1.3.1 Model set up

The model domain was designed to accurately reflect the geometric and geographic features of the study area (Fig. 48 and Fig. 49). Grid cells were set to dimensions of 2 × 2 × 2 m to balance spatial detail and computational efficiency while still providing reliable results (Salata et al., 2016; Abdollahzadeh and Biloria, 2021). The domain includes Piazza della Scienza and a surrounding buffer zone of 130 m to North, 150 m to East, 190 m to South and 100 m to West (Fig. 49a), which serves a dual purpose: capturing the influence of nearby buildings on airflow and minimizing boundary errors that could affect the accuracy of results within the square. The domain grid is defined in a cartesian plane with square cells; this configuration allows the import of georeferenced bitmap images that can be rotated to align with the orientation of the site. This ensures the accurate representation of solar exposure and wind directions relative to building geometry. This configuration resulted in a computational grid of 178 × 236 × 40 cells (including the buffer zone), covering a plan area of 168032 m^2, with a total simulation domain volume of 13442560 m^3. Each simulation started at 5 AM to capture pre-sunrise conditions. Wind speed and direction were kept constant, while air temperature and relative humidity were updated hourly from measurements. All other environmental inputs, except solar radiation, were taken from the WS.

Three urban regeneration scenarios were simulated (Fig. 48): the square before the regeneration intervention (S0), at the end of intervention work, i.e. post -regeneration (S1), and in a future (planned) condition corresponding to the stage at which the newly planted vegetation is fully established (S2)

- Scenario S0 (Fig. 48a) presents a square surface predominantly covered with dark grey concrete blocks with vegetation limited to twelve Magnolia trees located in the central area adjacent to the tramway.
- Scenario S1 (Fig. 48b) is characterized by different materials and new flowerbeds. Fig. 49b-c shows a quadrant of the entire site, where grey Luserna stone cubes (L1) and nearly white granite slabs (G1) are reported. To accommodate grid resolution limitations, granite slabs were included only between the flowerbeds (Fig. 49c) In addition, shrubs

and trees such as field maples were planted in flowerbeds (B1), though their small size at the time left much of the surface bare (Fig. 49).

- Scenario S2 (Fig. 48c) shares the same ground surface layout as S1 but includes mature vegetation, reflecting the intended long-term effect of regeneration intervention and the growing season state of the square. In this configuration, the flowerbeds are modelled with dense low vegetation approximately 50 cm in height and fully developed 28 trees reaching around 8 m. The height was selected based on what the tree could realistically reach due to the thin soil and pruning.

The main characteristics of each scenario are presented in Table 6.

Table 6
Scenarios characteristics summarized.

	Regeneration phase	Paving / surfaces	Vegetation
S0	Pre-intervention	Dark-grey concrete blocks	12 Magnolia trees, small green patches
S1	Post-intervention (End of works)	**Luserna cubes (L1)** and **granite slabs (G1) / flowerbeds (B1)**	New plantings in flowerbeds (B1) **small**, **bare soil**
S2	Future condition	Same as S1	Mature vegetation

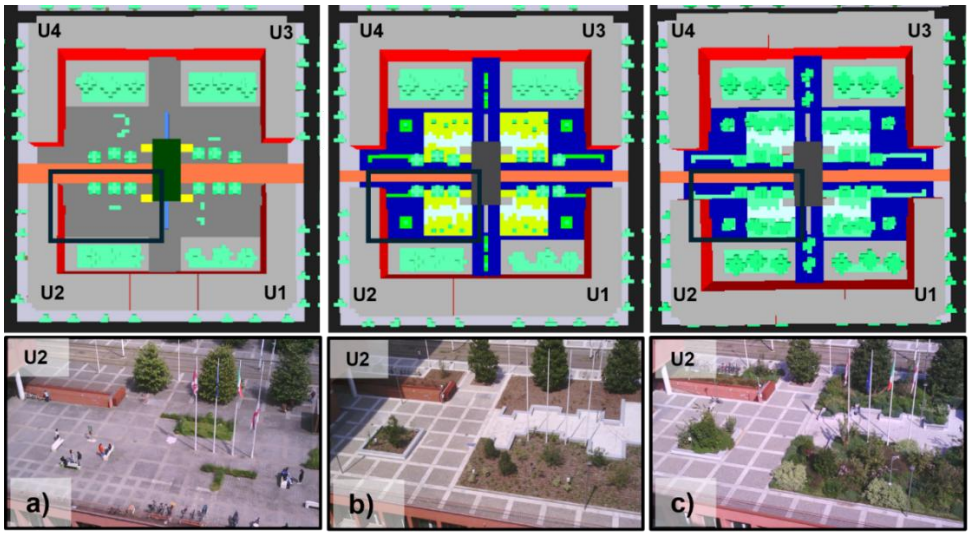

Fig. 48 The three different scenarios S0 – Pre-regeneration a), S1 – Post-regeneration b) and S2 – Post-regeneration (Growing Season) c) exploited to simulate environmental conditions in Piazza della Scienza.

As illustrated in (Fig. 48) certain regions or structural elements within the model remain unaltered across all scenarios. The orange line, oriented Est-West, corresponds to the tramway, which is surrounded by twelve Magnolia trees that were not involved in the regeneration projects. In the central area, the tram stop shelter (Fig. 48) and the staircase (Fig. 48) are located. The latter elements facilitate access to the University building via the basement. Following the completion of the regeneration work, the four underground courts at the corners of the square remained unchanged, despite their inclusion in the project plan. This deviation was attributed to complications during the construction process.

The three representations of the model in (Fig. 48) are accompanied by RGB images of quadrant related to building name U2. The images presented here illustrate the condition of the square on which the development of the scenarios was based. Given the symmetry of the square and the concurrent progression of the works across all areas, quadrant U2, as depicted in the images, can be considered a representative sample of the entire square.

5.1.3.2 Model calibration / validation

S1 (Fig. 49) was considered as the reference scenario for model calibration and testing, corresponding to the square configuration at the end of regeneration works and selected due to the largest availability of T_{surf} and T_a monitoring data. The model was calibrated on a selected day (30 July 2024), representative of the hottest days of the year in Milan, characterised by clear sky conditions, very low wind speed and high solar forcing, which is known to exert a major influence on surface temperatures (Bruse, 2004; Detommaso et al., 2021). Model calibration was conducted by adjusting the imposed values of material properties and wind speed settings and performed at three test areas corresponding to different surface materials, namely L1, G1 and B1 for T_{surf} and using the average simulated value at 3 m above ground, compared with the mean of two HOBO sensors positioned at the same height for T_a.

For each simulation, calibration performance was evaluated by comparing the measured and simulated values of T_a and T_{surf}, since these are the parameters best simulated by the model (Acero and Arrizabalaga, 2018). To do so, Root Mean Square Error (RMSE) and Mean Absolute Error (MAE; Detommaso et al., 2021; Tsoka et al., 2017) statistics were selected.

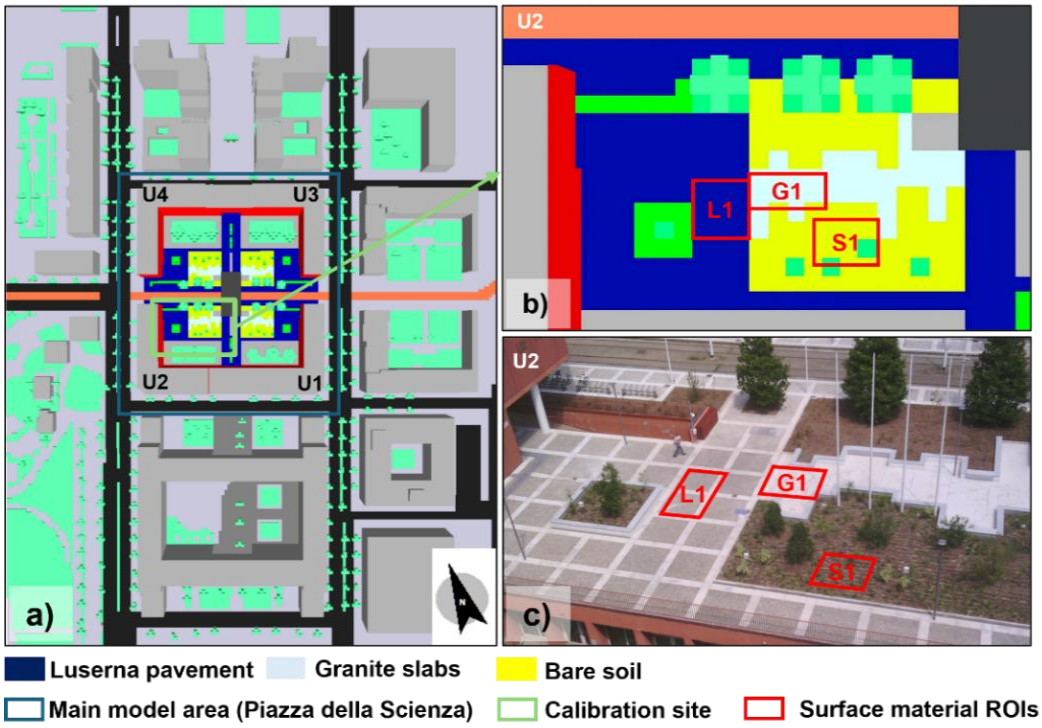

Fig. 49 Whole domain Scenario S1 reproduced in ENVI-met a). Modelled U2 quadrant used as model evaluation site; the different colours represent the new ground surfaces after the square regeneration b). RGB image of U2 quadrant c).

5.1.4 Thermal comfort evaluation with different tools

Thermal comfort was assessed using two complementary approaches: the BIO-met module included in the ENVI-met software and the Advanced Berkeley Comfort (ABC) model (Huizenga et al., 2001; Zhang et al., 2010a, 2010b, 2010c)

For the ENVI-met simulation, the Physiological Equivalent Temperature (PET; Gagge, 1972) was calculated. PET is based on the two-node model proposed by Gagge (1972), which balances body heat flows through radiation, convection, evaporation, and metabolism. The index was selected on the basis that, amongst the range of comfort indices available within ENVI-met, it is best suited to the assessment of outdoor thermal comfort. The input data for BIO-met module are derived from numerical simulations, specifically the output variables of atmospheric conditions.

To complement this evaluation, and to compare the results of two different tools, the ABC model has been utilized. The Advanced Berkeley Comfort Model, itself derived from Slowijk's classic thermoregulation scheme (Stolwijk and Hardy, 1966), has been further

developed to incorporate key improvements, including detailed body segmentation, multilayer tissue representation, and a refined hemodynamic model with countercurrent heat exchange. In contrast to conventional indices, such as PET, the ABC model integrates physiological variables with perceptual predictors, thereby enabling the estimation of both local and whole-body thermal sensation and comfort (Tanabe et al., 2023).

The ABC model necessitates the consideration of several key atmospheric variables to ensure its functionality. These were obtained directly from the outputs of the ENVI-met simulations.

5.1.4.1 Thermal comfort set-up

Thermal comfort analysis was performed, considering the experience of a pedestrian crossing the square where the path is composed of four stops, each lasting 10 minutes (Fig. 61, Fig. 62). The selection of stops was determined by the variation in pedestrian exposure to solar radiation. In scenarios S0 and S1, the shaded areas are confined to the initial and final stops, with shades generated by structures such as the building and the tram canopy. In scenario S2, however, the second stop on the path is located under the shade provided by mature trees.

Regarding the assessment of comfort using ENVI-met, the PET values were extracted from the maps corresponding to a height of 1.4 m.

ABC model accurately reproduces thermal comfort using variables acquired over a short period of time. For this reason, thermal comfort was assessed using hourly ENVI-met simulation outputs. To do so, four receptors were suitable positioned at each stop to have outputs every one minute. It is important to note that all the input variables refer to a particular time of day, specifically from 2 PM to 2:40 PM, one of the hottest times of the day.

Other inputs, such as the demographic characteristics of the subject and their clothing, were kept standard for both tools involved. In particular, a 35-year-old male subject was utilized as a model. The clothing insulation values, for a summer clothes type, refer to those proposed by the study by Lee et al. (2013). Table *7* lists the main thermal comfort indices for reference

Table 7 Overview of thermal comfort indices and approaches commonly used in outdoor urban studies.

Index	Variables considered	Output	Applications and limitations	References
PET (Physiological Equivalent Temperature)	Air temperature, humidity, wind speed, radiation (MRT)	Equivalent temperature (°C)	Widely used for outdoor thermal comfort assessment due to its intuitive interpretation. It relies on standardised assumptions and may not fully capture individual variability	(e.g., Pantavou et al., 2011; Jamei et al., 2016)
UTCI (Universal Thermal Climate Index)	Air temperature, wind, humidity, radiation	Equivalent temperature (°C)	Suitable for large-scale and comparative studies thanks to its strong physiological basis; less commonly applied in detailed design contexts	(e.g., Jamei et al., 2016)
PMV (Predicted Mean Vote)	Air temperature, humidity, wind, radiation, clothing, metabolism	Thermal sensation scale	Standardised approach widely used for indoor environments; its application in outdoor conditions is limited due to high environmental variability	(e.g., Jamei et al., 2016)
MRT (Mean Radiant Temperature)	Shortwave and longwave radiation exchanges	Radiative thermal load	Key variable for interpreting outdoor thermal comfort and the effects of shading; not a standalone comfort index	(e.g., Oke et al., 2017)

5.2 Results

5.2.1 Long term in-situ monitoring results

Fig. 50 shows various monitoring acquisitions carried out during the project phases. Prior to the intervention (Fig. 50a, S0 scenario), the concrete block paving (C) registered surface temperatures of approximately 55 °C at 3 PM, whereas the small permeable grassy area (S) exhibited a maximum temperature of about 32.5 °C. However, after 6 PM, the temperature over the vegetated area exhibited a rapid decline, remaining below the air temperature throughout the night.

In May, during the intermediate phase of the works, the new paving had already been installed (Fig. 50b). The maximum T_{surf} was recorded at approximately 42.5°C at 4 PM on the Luserna stone (L1). Granite (G1) recorded a consistent temperature difference of approximately 5 °C from 12 PM onwards, with a subsequent drop in surface temperature below the T_{air} (20 °C) after 2 AM. The areas of the thermal image that exhibit the highest temperatures correspond to the zones that had been designated for the installation of permeable soil, although these plans had not yet been executed at that time. In conclusion, the August acquisition (Fig. 9c), which was conducted shortly following the completion of the works (S1 scenario), indicates that Luserna stone (L1) reached a maximum of 50°C at 5:30 PM, with T_{surf} above 40°C until midnight. Granite (G1) exhibited a comparable diurnal pattern; however, it remained 8 °C cooler during the afternoon and 5 °C cooler for the rest of the day. Bare soil in the new flowerbeds (B1) exhibited lower temperatures than the paved surfaces, but still reached values close to 40 °C, becoming cooler than the air temperature (32.5 °C) after 8:30 PM.

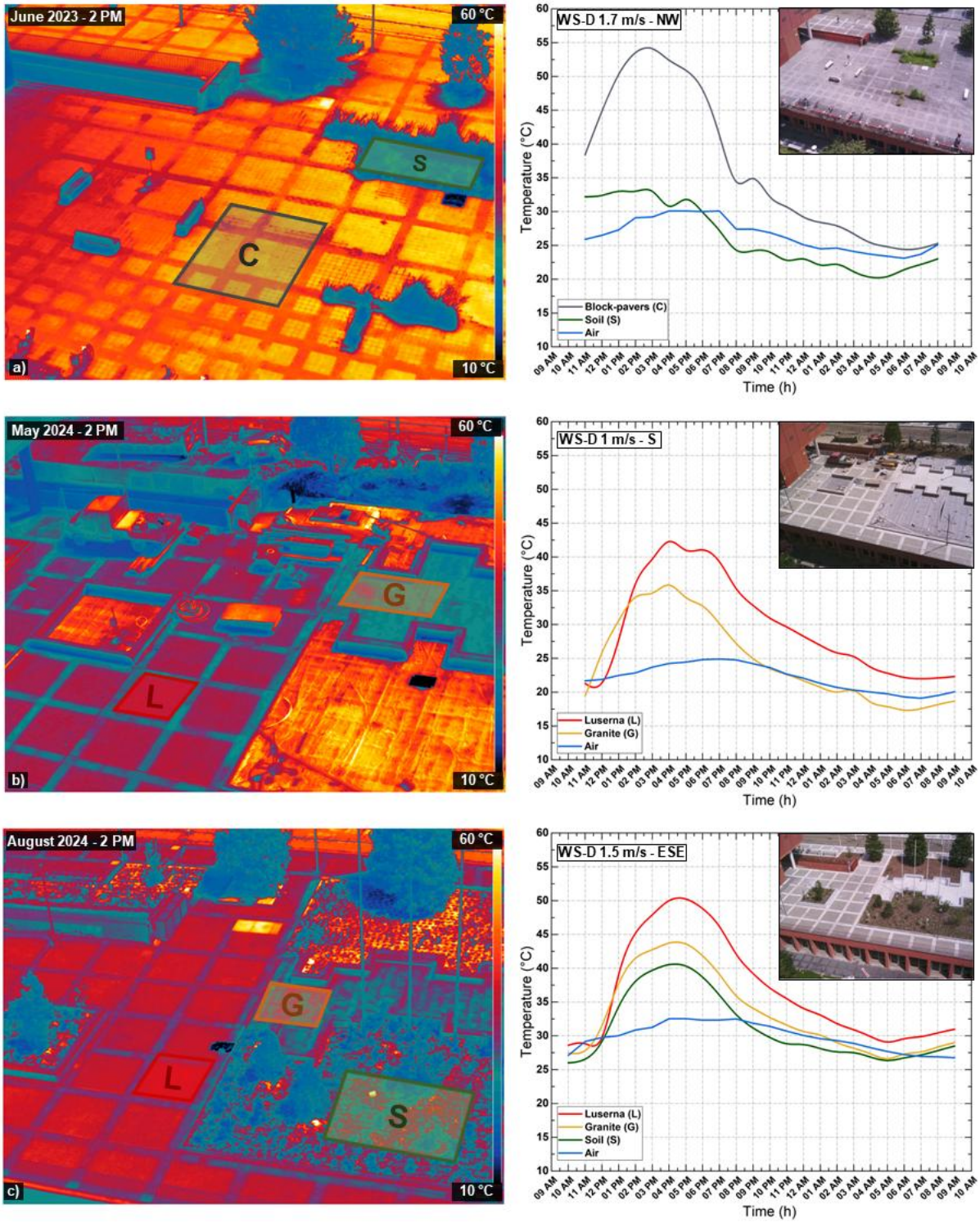

Fig. 50 Thermal images were acquired during the work phases. The graphs below show the T_{surf} measurements for the day, with information on T_a, wind speed and direction (WS-D). Image acquired on 20 June 2023 at 2 PM pre-regeneration (S0 scenario, a), image acquired on 1 August 2024 at 2 PM (Scenario S1, c)

5.2.2 Preliminary calibration tests

Before reaching the final model configuration, several simulation runs were carried out. In particular, using different solar radiation datasets and employing both the basic and advanced meteorology input methods. In the basic configuration, solar radiation is not uploaded manually but is instead calculated by the software based on geographic coordinates and the simulation date, assuming clear sky conditions, while the advanced method uses hourly solar radiation. In this case, the hourly solar radiation data were provided by ENEA (ENEA, 2006), and measurements from the Davis Pro2 weather station installed in the square.

ENEA data are derived from METEOSAT cloud cover satellite imagery, with a spatial resolution of $1 \times 1.5\ km^2$, available from 2006 onwards. As these are estimated values, discrepancies of up to 10% can occur when compared with in-situ measurements. Although WS data are site-specific, they represent global horizontal irradiance (GHI). However, the model requires the separation into direct solar radiation (SW Dir) and diffuse solar radiation (SW Diff). To address this, GHI values were split into their direct and diffuse components by applying the percentage of SW Diff derived from the ENEA dataset.

The graph in (Fig. 51) presents the hourly solar radiation curves from both ENEA and WS sources. The patterns demonstrate typical clear sky behaviour, following a smooth, regular trend without significant drops throughout the day. This consistency suggests that the basic meteorology method, which calculates potential solar radiation under clear sky assumptions, was suitable for the simulation in these conditions. Although the model shows higher values the residual mismatch may partly reflect differences in spectral response and bandwidth between modelled shortwave radiation (0.3–3 μm) and, at least, the WS sensor (0.3–1.1 μm).

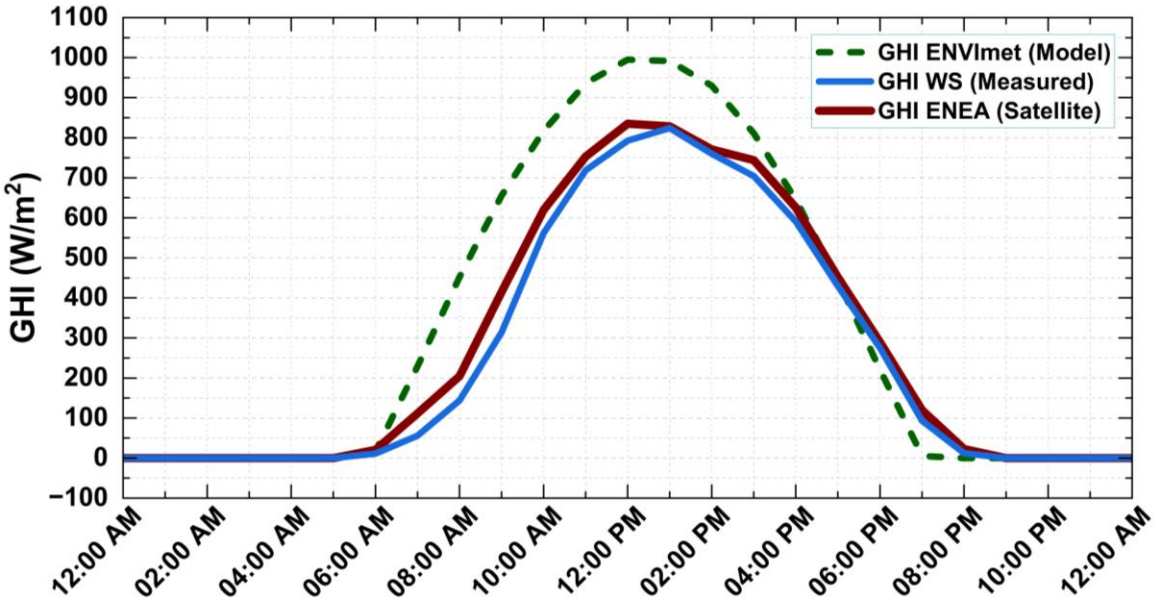

Fig. 51 Global Solar Radiation (GHI) data from different sources (WS and calculated by ENVI-met).

In the initial test, the advanced (full forcing) method was employed, utilising data from the local weather station as meteorological forcing and ENEA data for solar radiation. However, this setting produced simulated air temperatures that were systematically higher than the observations, while surface temperatures were underestimated (Fig. 52). In the second test, the advanced configuration was maintained, with the wind speed increased by 0.5 m/s to verify a possible reduction in air temperature. The effect was present but limited, and the underestimation of surface temperatures remained substantially unchanged (Fig. 53). The third test focused on the radiative properties of the materials, reducing the albedo to increase absorption and induce an increase in surface temperatures. However, the observed effect was limited (Fig. 54). In the fourth test, for the same objective, the emissivity was also reduced, while maintaining the settings of the previous test (Fig. 55). For tests 3 and 4, the duration of the simulation was intentionally reduced to minimise computational time, thereby focusing the analysis on the hours of maximum radiation and peak temperature phases. The RMSE and MAE values for each test are shown in Table 8.

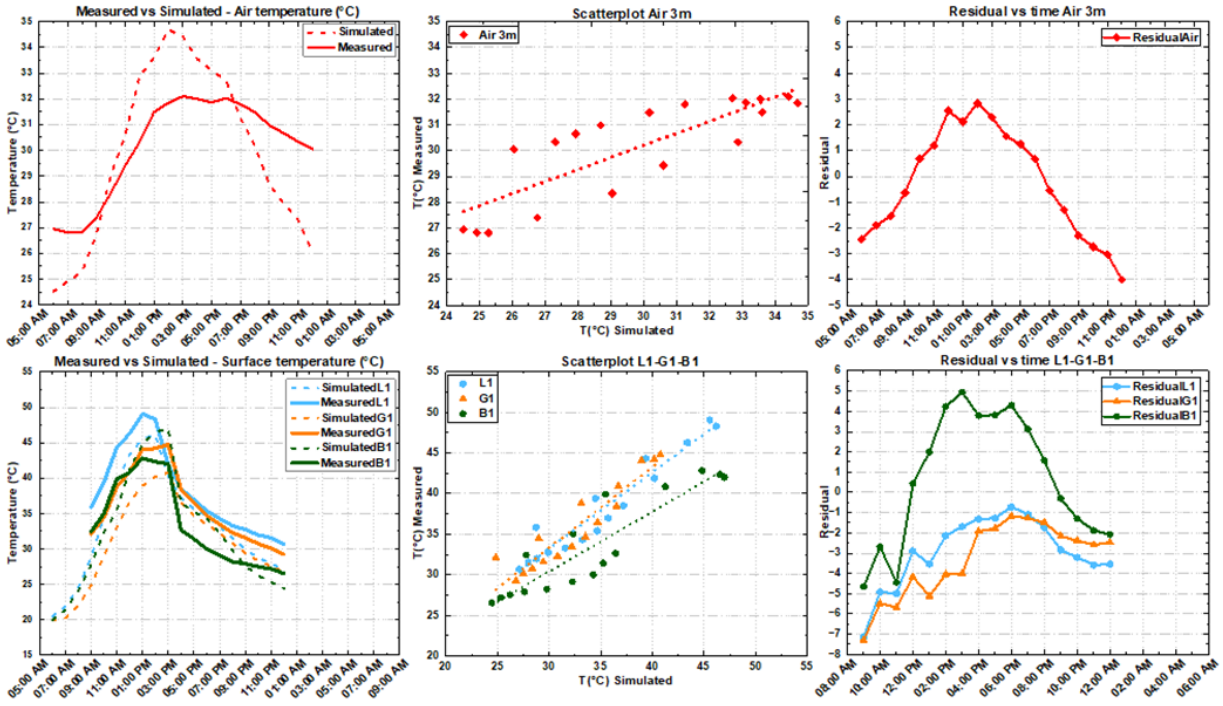

Fig. 52 Test 1. A full forcing setup was adopted using solar radiation from the ENEA dataset and meteorological variables measured by the local weather station (WS) as boundary conditions, to assess the model response against observations.

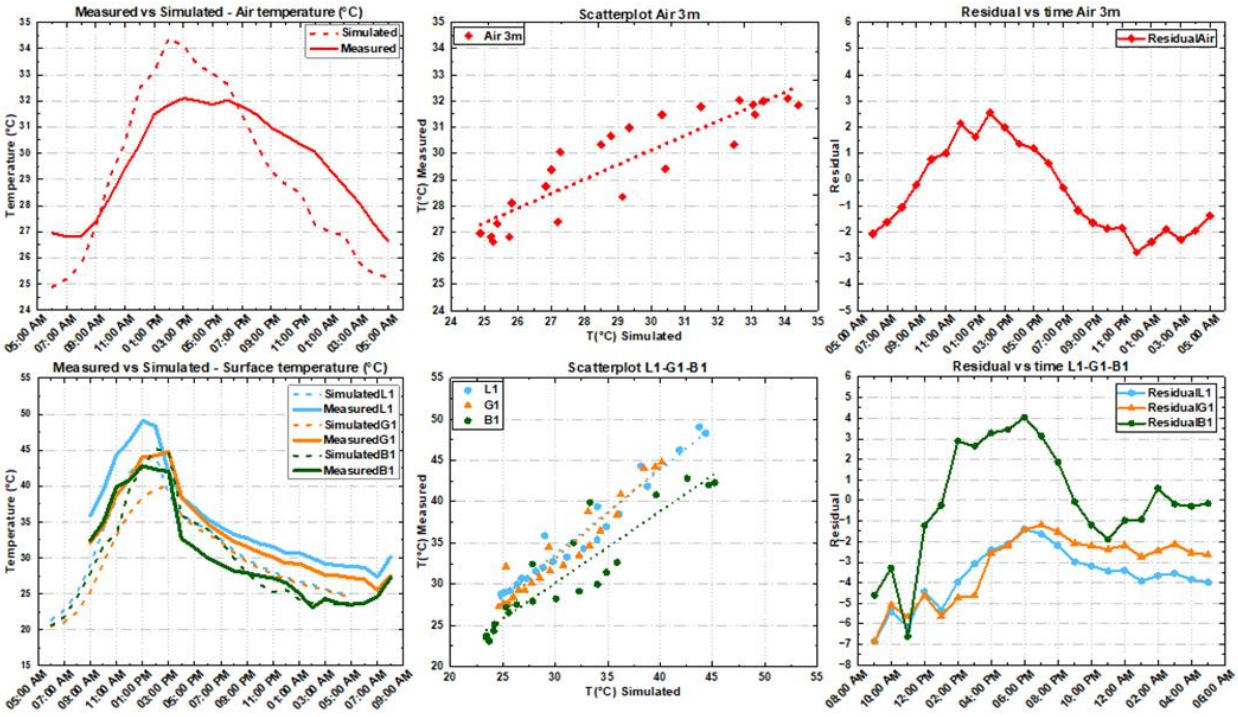

Fig. 53 Test 2. Same configuration as Test 1, but with wind speed increased by +0.5 m/s (relative to the WS record) to test the effect of enhanced ventilation and attempt to reduce the simulated air temperature.

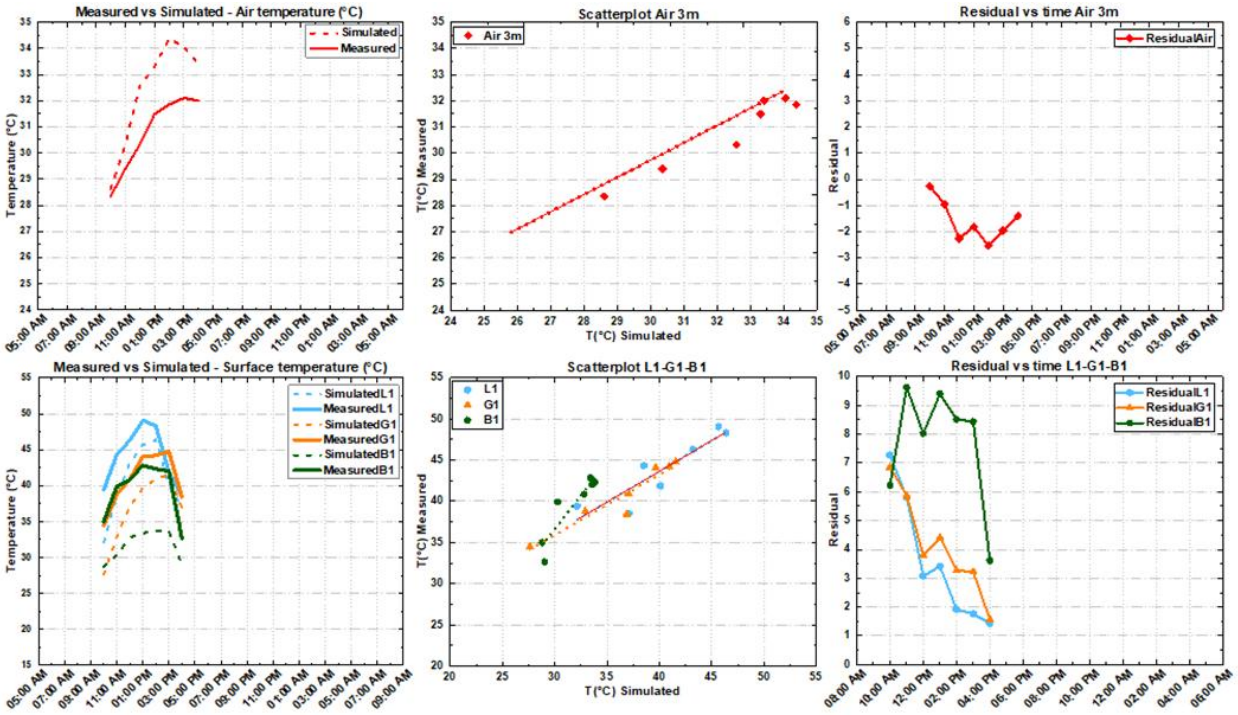

Fig. 54 Test 3. Same setup as Test 2, but with lower albedo to increase radiative absorption and investigate whether simulated surface temperatures could be raised.

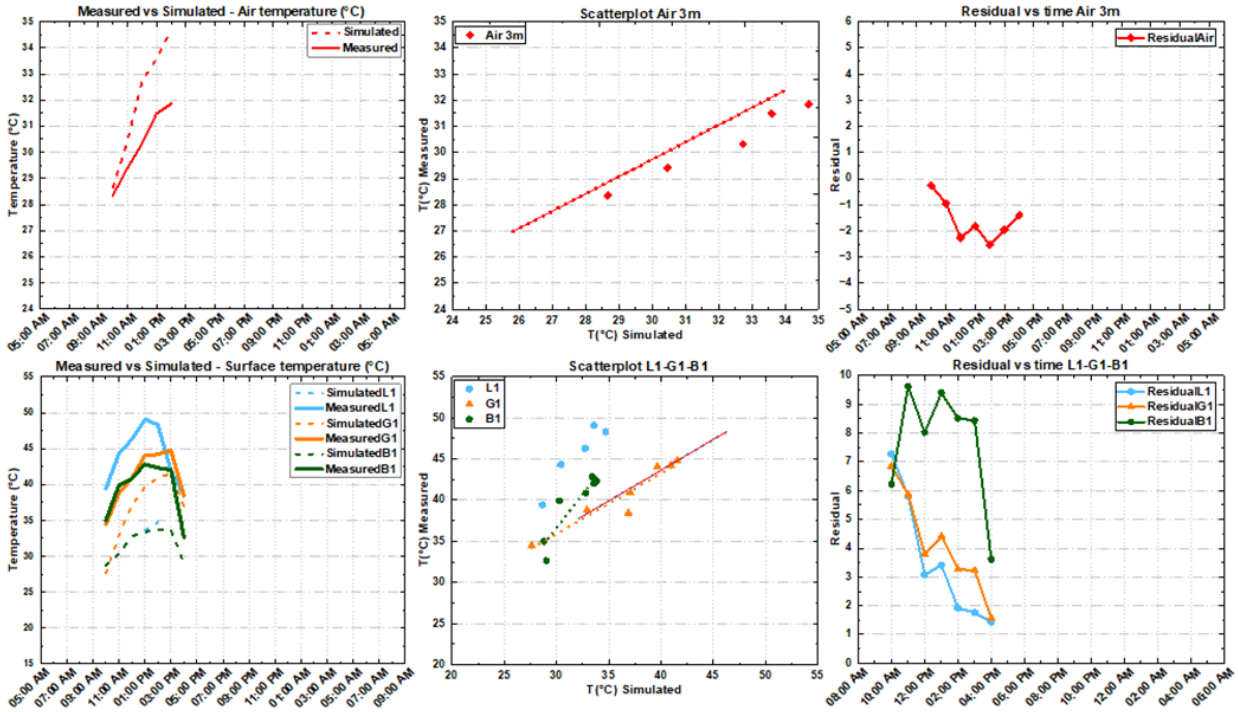

Fig. 55 Test 4. Same setup as Test 3, with a further adjustment by also reducing emissivity, aiming to increase surface temperatures and improve agreement with measurements.

Table 8
RMSE and MAE values for the preliminary calibration tests

Test1	Tair	Tsurf L1	Tsurf G1	Tsurf B1
RMSE	2.08	3.35	4.47	3.21
MAE	1.87	2.91	3.31	2.85
Test2				
RMSE	1.73	3.37	3.98	3.07
MAE	1.59	3.06	3.49	2.65
Test3				
RMSE	1.75	4.08	4.45	7.21
MAE	1.59	3.52	4.14	6.94
Test4				
RMSE	1.97	4.51	4.79	3.54
MAE	1.73	4.23	4.42	2.95

5.2.3 Validation of reference scenario

Among the tested configurations, the combination of basic meteorology and the meteorological input and the material parameters reported in Table 9 minimised errors (RMSE/MAE) across the calibration targets, indicating the most robust model setup.

As illustrated in Fig. 56a, the model tends to overestimate T_a values during the first half of the day, up to 6 PM, and underestimate them afterwards. This behaviour has been reported in other validation studies as well (Yang et al., 2013; Middel et al., 2014; Acero and Herranz-Pascual, 2015; Tsoka et al., 2018). Overall, the agreement represented by the RMSE and MAE values is high (1.36°C and 1.16°C, respectively) and the R^2 value is 0.72.

When compared with reference values reported in the literature (Piselli et al., 2018), the model demonstrates acceptable performance. Both RMSE and MAE fall below the median values presented by (Tsoka et al., 2018) which are 1.51 °C and 1.34 °C, respectively, while R^2 is only slightly lower than the typical median value of 0.92.

T_{surf} (Fig. 56b) is accurately reproduced by the model during the morning and early afternoon for L1. However, a slight underestimation is observed from 5 PM onwards. The Root Mean

Square Error (RMSE) and Mean Absolute Error (MAE) for L1 are 2.30 °C and 2.12 °C, respectively, with an R^2 of 0.97, indicating a strong correlation between observed and simulated data.

A similar trend is evident for G1, where underestimation begins at 5 PM and continues through the evening, as well as between 1 PM and 4 PM. Despite this, the overall agreement remains high, with RMSE and MAE values of 1.45 °C and 1.35 °C, respectively, and an R^2 of 0.98.

In the case of B1, the model overestimates surface temperatures during the hottest part of the day (11 AM to 4 PM), likely due to the model's inability to simulate intermittent irrigation that occurred on-site during this period, at midday and even at nighttime at 3 AM. However, the temporal patterns between measured and simulated values are consistent. The corresponding RMSE and MAE are 3.01 °C and 2.34 °C, respectively, with an R^2 of 0.96. Although relatively few studies have used surface temperature to validate ENVI-met, the R^2 values obtained in this study are near the upper end of the range (0.6 to 0.97) reported in the literature (Tsoka et al., 2018).

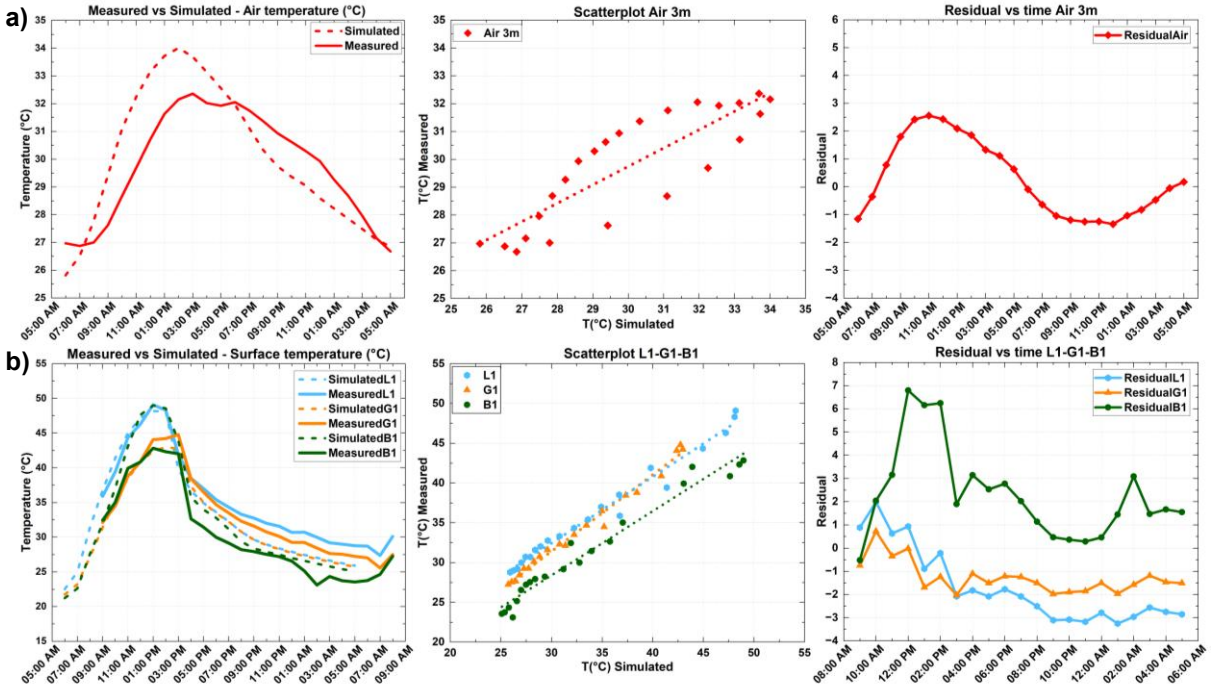

Fig. 56 Graphic visualization of the model calibration. Air temperatures simulated vs measured data above a) and surface temperatures simulated vs measured data below b), with their scatterplots and residual vs time plots

Table 9

Simulation information for model validation and scenarios comparison

Simulation settings				
Start simulation day (dd.mm.yyyy)	30/07/2024			
Start simulation time (hh.mm.ss)	05:00:00			
Total simulation time in hours (h)	24			
Output timestep (min)	60			
Meteorological inputs				
Wind speed [m/s]	2			
Wind direction [∘]	150			
Air Temperature T_a [°C]	Hourly data from weather station			
Relative Humidity RH [%]	Hourly data from weather station			
Soil inputs				
Upper layer (0-20 cm) [°C]	20			
Middle layer (20-50 cm) [°C]	20			
Deep layer (50-200 cm) [°C]	18			
Type of Pavement	**Albedo**	**Emissivity**	**Volumetric heat capacity** $\mathbf{J/(m^3K)*10^{-6}}$	**Heat conductivity (w/mK)**
Concrete	0.15	0.98	2.08[a]	1.63[a]
Luserna	0.25	0.97	1.75[a]	2.33[a]
Granite	0.47	0.96	2.34[a]	3.10[a]
Tram line (Metal line)	0.25[a]	0.95[a]	2.00[a]	1.00[a]

[a] Software default value.

5.2.4 Scenario-based simulations in extreme summer conditions

5.2.4.1 Scenarios comparison

To observe daily temperatures variation, T_a and T_{surf} maps (Fig. 57) of reference scenario S1 were analysed at four different times of the day, namely 9 AM, 2 PM, 5 PM and 9 PM.

T_a maps (Fig. 57 top line *a*) are presented at 1 m above ground level. The eastern portion of Piazza della Scienza is largely shaded due to the orientation of the buildings and their relative position to the sun. At 9 AM, air temperature across the square is approximately 29 °C, with values ranging from 27.7 °C to 30.8 °C. The coolest areas are found near the eastern facades and around the central Magnolia trees, where shading and the presence of vegetation contribute to localized cooling effects. At 2 PM, corresponding to the peak of solar radiation, shading is confined to a few limited areas. Air temperatures rise significantly, ranging from 32.4 °C to 37.2 °C. The northern sector of the square records the highest values, while slightly lower temperatures are observed along the southern edge, particularly near buildings U1 and U2. This gradient reflects differences in solar exposure and shading patterns, which are strongly influenced by the square's geometry and its 21° rotation from the north. By 5 PM, a moderate reduction in air temperature is detected, with values ranging from 31.6 °C to 35.8 °C. The western area appears to be the coolest at this hour, likely due to increased shading in the late afternoon. At 9 PM, after sunset, the thermal gradient within the square becomes less pronounced. The difference between the minimum and maximum values is reduced to approximately 3 °C. The lowest air temperatures are concentrated near the central vegetation and at the corners of the buildings, indicating a residual cooling effect associated with the shaded and vegetated zones, and reduced thermal inertia in these microenvironments.

T_{surf} maps (Fig. 57 bottom line *b*) are presented at the same selected daytime. At 9 AM, following approximately two hours of solar exposure, surface temperatures exhibit significant variation, ranging from 22 to 41.5 °C. In shaded eastern areas, temperatures remain lower than in other regions. On the western side, the lowest recorded temperatures are found in areas of granite slabs and exposed soil, which exhibit minimal heat accumulation during this period. At 2 PM, a marked increase in surface temperatures is observed, ranging from 26 to 58.5 °C. At this time, shadows are minimal, and thermal contrasts are pronounced. Granite surfaces have been found to demonstrate consistently lower temperatures than the

other surfaces, particularly in areas situated beneath Magnolia trees. This phenomenon can be attributed to the material properties of granite itself, including higher reflectance, as well as the impact of vegetation shading. At 5 PM, a slight decrease in surface temperatures is observed, from 27°C to 51.9°C. The eastern side, still exposed to solar radiation, exhibits higher values, particularly in Luserna-paved areas. In contrast, the bare soil zones on the western side cool more rapidly. At 9 PM, the absence of solar radiation results in a more homogeneous surface temperature distribution, with differences reduced to around 9°C. The bare soil patches were found to be the coldest surfaces at this time, indicating faster heat loss compared to mineral paving.

Overall, no clear spatial correspondence emerges between surface temperature patterns driven by paving materials and air temperature at pedestrian level during the day. Areas with lower T_{surf} over more reflective paving do not show systematically lower T_a. Cooler T_a is mainly observed where shading from vegetation and buildings reduces solar exposure.

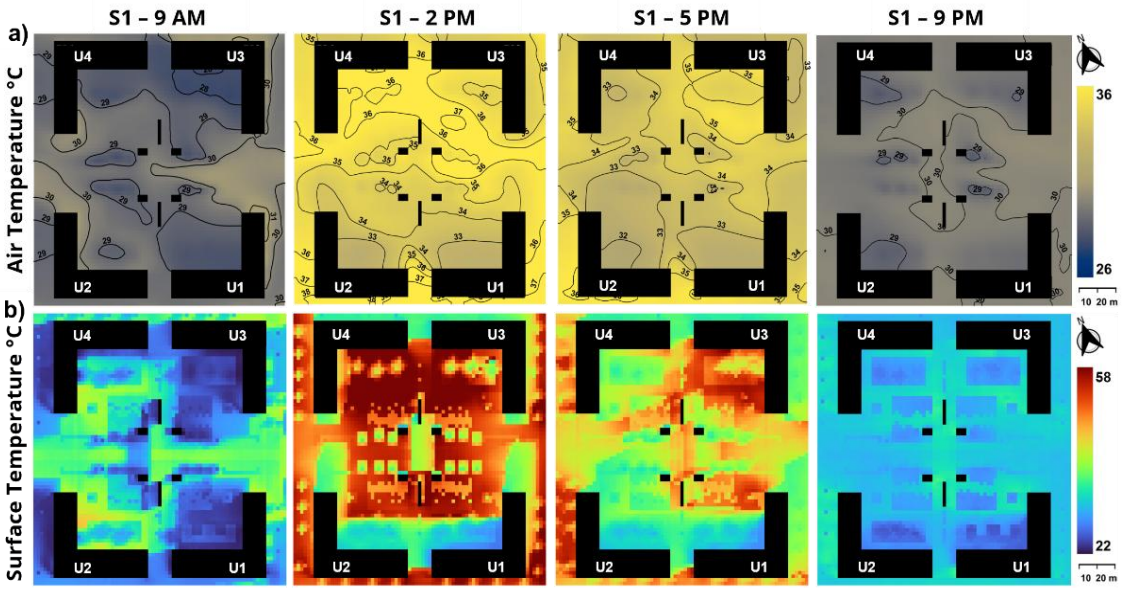

Fig. 57 T_{air} distribution at four different hours of the day (Top line a). Bottom line represents T_{surf} distribution at the same time b)

For a comparative analysis of the three scenarios, a single time of day was selected, with the most extreme conditions occurring during daylight hours; Fig. 58 presents the model output maps for 30 July at 2 PM. The four variables analyzed, namely T_a, RH, T_{surf} and the bio-meteorological parameter Mean Radiant Temperature, were selected since they are among

the key variables affecting outdoor thermal comfort (Abdollahzadeh and Biloria, 2021; Olivieri et al., 2024). T_a, RH and MRT maps were computed at a height of 1 m.

The spatial distribution of air temperature (Fig. 58*a*) appears similar in both S0 and S1 scenarios, with values ranging from 32.4 °C to 37.3 °C. In the S2, cooler zones become more widespread, particularly on the western side of the square. The overall temperature range shifts slightly, with the minimum decreasing to 32.1 °C and the maximum dropping to 36.6 °C. These modest changes suggest a localised cooling effect attributable to increased vegetation and associated shading.

The distribution of relative humidity (Fig. 58*b*) in S0 and S1 shows similar patterns, with only minor localised reductions in the central area. In contrast, S2 reveals a more extensive and uniform increase in relative humidity, especially across the central and southern portions of the domain. This behaviour is consistent with the combined effect of evapotranspiration and lower air temperatures, both of which contribute to higher RH at pedestrian height.

The most pronounced differences between scenarios emerge in surface temperature distributions (Fig. 58*c*). Scenario S0, in paved areas exposed to solar radiation, presents a homogeneous pattern, with values ranging between 47.5 °C and 50 °C, consistent with the uniform surface properties. In both S1 and S2, surface temperatures remain high in areas paved with Luserna stone, similar to those observed in the dark concrete blocks of S0. However, granite slabs consistently exhibit lower temperatures, with reductions of up to 5 °C compared to the pre-regeneration and adjacent Luserna areas. In S2, the presence of vegetation becomes clearly visible, with temperature reductions of approximately 7 °C in vegetated soil zones and up to 10 to 12 °C in areas shaded by tree canopies.

MRT shows a different response (Fig. 58*d*). Compared with S0, S1 does not provide an improvement in MRT under peak solar exposure, and localized increases can occur over highly reflective paving. In S2, substantial reductions are evident beneath mature tree cover, with differences reaching about 25–30 °C in fully shaded areas. This highlights the dominant role of tree shading in reducing radiative heat load at pedestrian level.

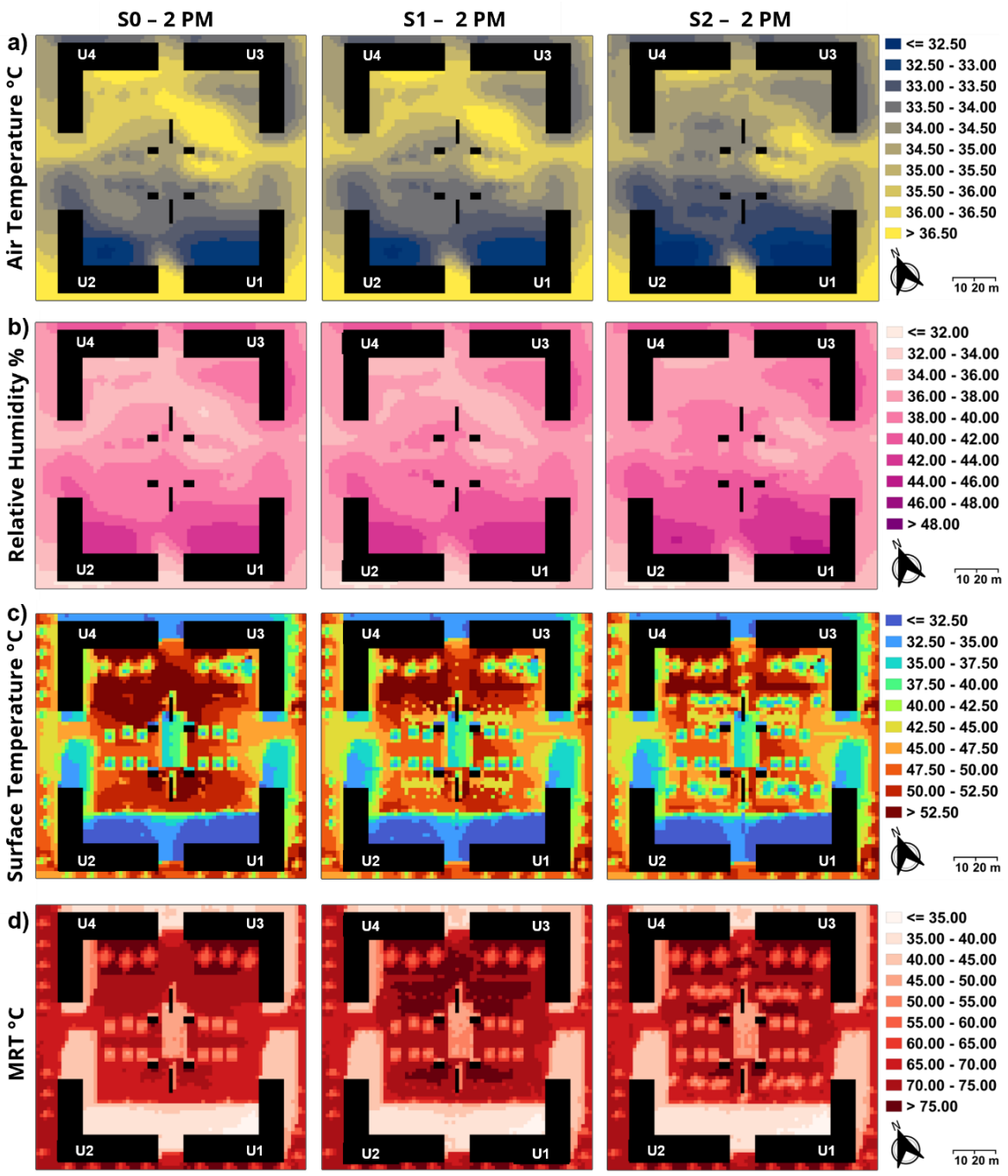

Fig. 58 The maps show the distribution of T_{air} (a), RH (b), T_{surf} (c) and MRT (d), at the same time for scenarios S0, S1 and S2

The comparison of maps allows capturing the spatial patterns of different parameters across the square. However, by extracting the data for each cell, it is possible to obtain a general comparison between the three scenarios for the selected parameters. The extraction cells under consideration are those that fall within the area enclosed by the four buildings. Fig. 59

shows the diurnal variation of the four key parameters previously analysed, represented through boxplots for the three simulated scenarios.

The plots capture both the temporal trends and the internal variability of microclimatic conditions across Piazza della Scienza. These results provide insight into how differences in surface materials and vegetation influence the overall thermal environment throughout the day.

Air temperature at 1m height (Fig. 59a) shows limited variation between scenarios. In Scenario S1, the introduction of new paving materials and bare soil yields only minor reductions compared to the Pre-regeneration. The maximum difference between the median values occurred at 11 AM, reaching 0.2 °C, while after 7 PM, the differences remain below 0.2 °C. In S2, where vegetation has reached full maturity, a more persistent cooling effect is observed. Temperature differences exceed 0.37 °C for most of the day, with the greatest reduction, approximately 0.6 °C, occurring at 5 PM. These findings suggest that the presence of vegetation contributes to modest but continuous reductions in near-ground air temperature during the hottest hours.

Relative humidity at 1m height (Fig. 59b) follows a similar temporal pattern across all scenarios. Absolute differences are consistently below 1.8 %, a value that falls within the typical accuracy range (±2 %) of standard outdoor sensors. Given this limited variation, relative humidity was not considered a critical factor for further microclimatic evaluation in this case. As shown in Fig. 59c, surface temperature demonstrates the highest variability both temporally and spatially. This is attributed to the heterogeneous distribution of shading from buildings and vegetation, as well as the varying thermal properties of ground surfaces. The greatest difference between S0 and S1 is observed at 11 AM, with a maximum drop of mean temperature of 1.5 °C. The highest surface temperatures occur in the early afternoon, when solar forcing is strongest. S2 consistently exhibits lower surface temperatures than the Pre-regeneration. Reductions surpass 2.2 °C for most of the day, with a maximum difference of approximately 2.6 °C recorded around midday. Mean radiant temperature at 1m height (Fig. 59d) also shows notable variability, particularly during early morning and late afternoon hours, when parts of the square remain shaded. This variability reflects the complex radiative exchanges between urban surfaces and the human body, including possible direct solar exposure (Aleksandrowicz et al., 2023). Scenario S1 does not improve mean radiant

temperature compared to the Pre-regeneration; rather, the use of high-albedo granite paving appears to increase MRT values throughout the day. In Scenario S2, the presence of mature vegetation contributes to substantial reductions in mean radiant temperature, especially in shaded zones. These findings underline the critical role of vegetation in mitigating radiant heat load and enhancing outdoor thermal comfort for pedestrians.

Finally, it is significant to observe the variation in surface behaviour throughout the day. The lines shown in Fig. 59c represent the temperature trends of different materials, by selecting three points (L1, G1 and B1) with the same location in the three scenarios. In the first scenario, the surface remains constant, and the trend is applicable to the three points under consideration. In the second case, it is evident that the granite curve attains lower T_{surf} values, even when compared to the bare soil. The latter has been shown to exhibit a slower heating and faster cooling phase than impermeable surfaces yet still reach temperatures similar to those of Luserna at peak times. In the third scenario, characterised by denser vegetation on soil, the temperature remains lower than in Luserna, although it is higher than in granite.

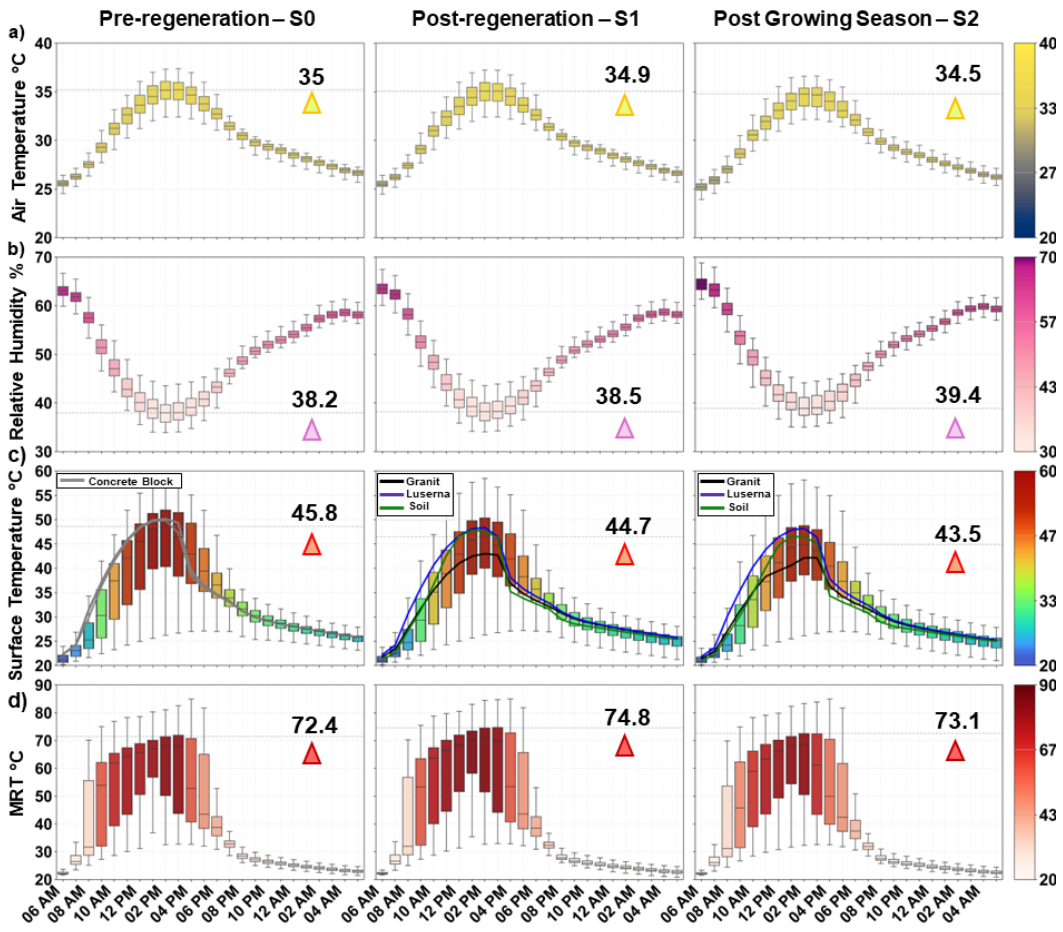

Fig. 59 Boxplot representation of T_{air} (a), RH (b), T_{surf} (c) and MRT (d), throughout the day for scenarios S0, S1 and S2. The lines in surface temperatures (c) graphs represent the different surfaces within the squares. Temperature values reported in each plot correspond to the maximum value (minimum for RH) of the median that has been simulated over the course of the day.

Wind is a key factor in influencing the microclimate and thermal comfort (Salata et al., 2016). As shown in Fig. 60, the wind flow at a height of 1 m is overlaid on the air temperature map (1 m height) at 2 PM for the three scenarios. Within the confines of the square, the areas in proximity to the buildings and the corners of the square exhibit low speeds ranging from 0.4 to 0.8 m/s. The central east-west channel, the flow is slightly attenuated, with speeds in a range between 1.5 and 1.8, which is similar to those at the entrance and exit of the square. Furthermore, a spatial correspondence between ventilation flow and air temperature has been observed.

The transition from S0 to S1 exhibits minimal alterations in wind patterns, suggesting that surface materials and the presence of exposed flower beds have negligible effects on airflow.

In scenario S2, particularly in areas where trees have grown, there is a slight decrease in wind speed compared to the two previous scenarios. It has been observed that, in both the northern and southern regions, a decline in the flow rate is associated with a decrease in temperature at these points.

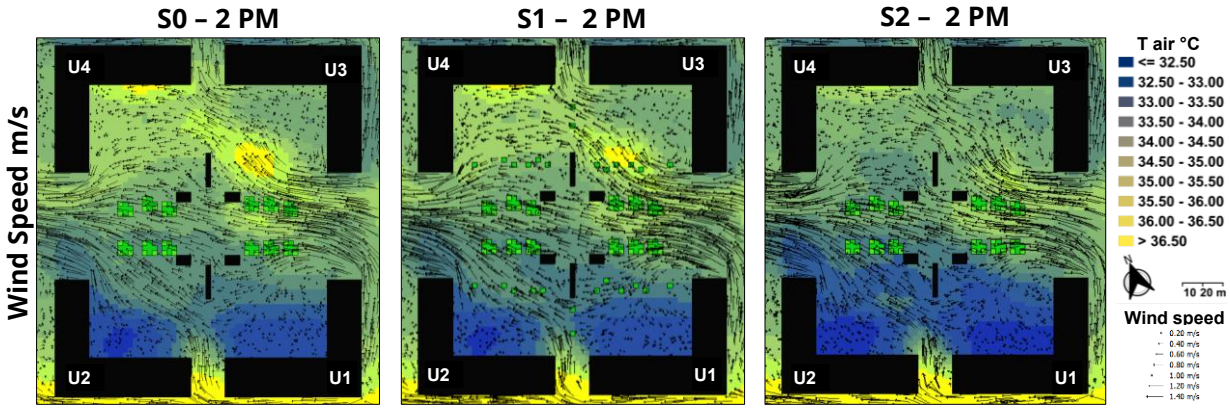

Fig. 60 The wind flow has been overlaid on the T_{air} map. The wind and air temperature map is referenced at a height of 1 m and at 2 PM for the three scenarios

5.2.4.2 Thermal comfort analysis

As shown in Fig. 61, in the pre-regeneration condition (S0), PET peaks around 3 PM, exceeding 45 °C at the most exposed locations, corresponding to conditions of extreme thermal stress. The implementation of high-albedo paving (S1) produces only a modest reduction, up to 2 °C, in central areas, with peak discomfort persisting during the early afternoon hours. Conversely, the scenario with mature vegetation (S2) exhibits a substantial attenuation of PET, with peak values reduced by 4 to 6 °C during the hottest period of the day and a faster cooling in the evening. This improvement reflects the combined influence of tree shading and evapotranspiration.

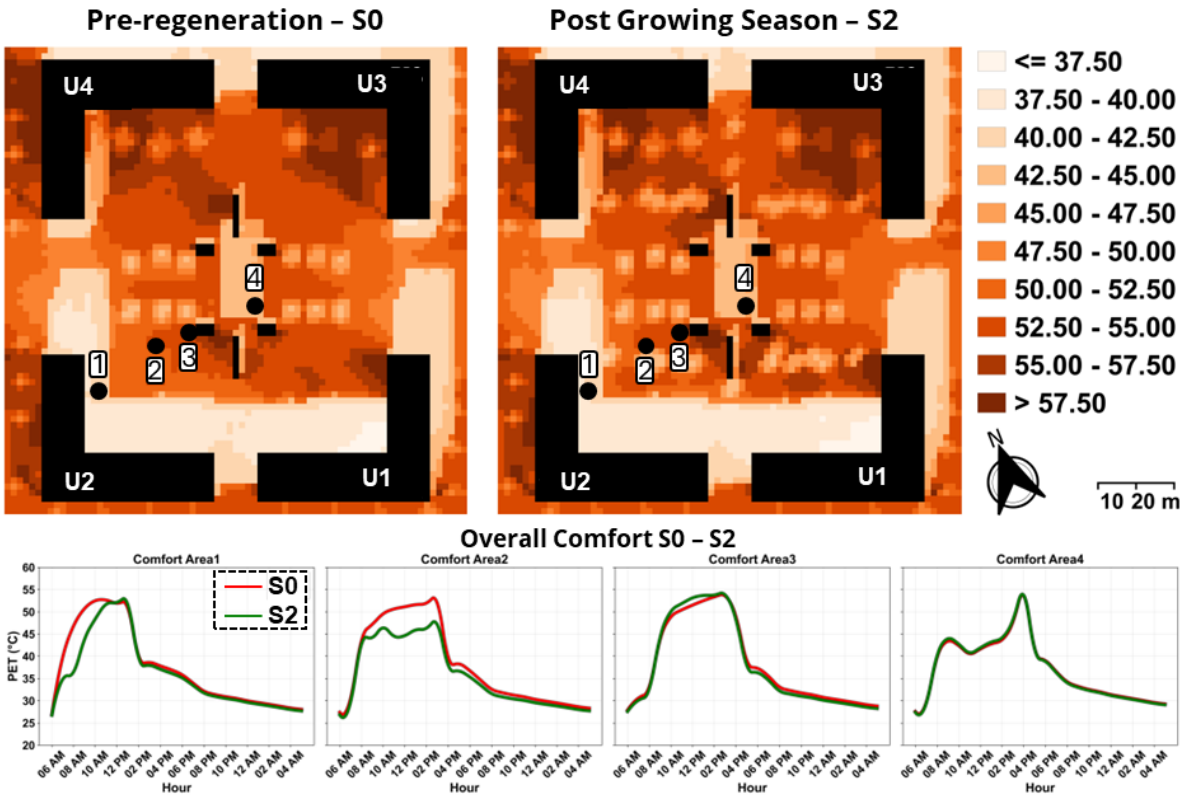

Fig. 61 Diurnal variation of the Physiological Equivalent Temperature (PET) at four receptors for the three simulated scenario

As illustrated in Fig. 62, the four receptors were positioned in the same locations in all scenarios. At the initial stop, which corresponds to 2 PM in the shaded area of the building, the findings suggest the presence of discomfort, which exhibits an increasing trend over the subsequent 10 minutes. During the second stop, the receptor is fully exposed to solar radiation in scenarios S0 and S1, resulting in a rapid decrease in comfort followed by a slight stabilization, probably associated with short-term a brief stabilization to the new thermal conditions. A divergent outcome is observed in scenario S2, wherein the receptor remains in the shaded area, resulting in superior comfort levels compared to those in S0 and S1. In scenarios S0 and S1, comfort remains low at the third stop under direct sunlight. In contrast, a gradual reduction in comfort is observed in scenario S2. In conclusion, at the fourth stop, which is situated in the shade of the tram shelter, an initial improvement in comfort is observed. However, this is followed by a subsequent decrease in comfort, which then stabilizes at an overall level that is perceived as uncomfortable.

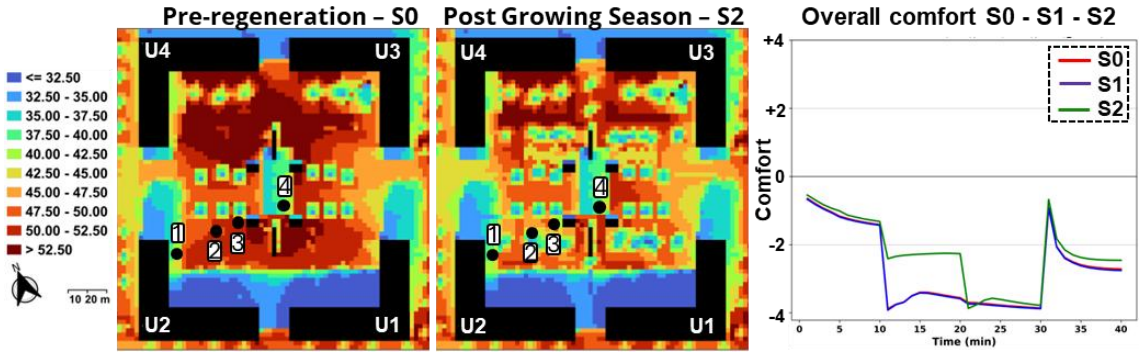

Fig. 62 The maps illustrate surface temperatures pre-work and post-work scenarios with mature vegetation, where the points at which thermal comfort is measured are visible. The following three graphs illustrate the overall comfort levels in each scenario. The values ranging from -4 to +4 express comfort, with -4 representing the most uncomfortable condition (very uncomfortable) and +4 representing the most comfortable condition (very comfortable)

5.2.5 Scenario-based simulations in moderate spring conditions

5.2.5.1 Scenarios comparison

The spatial distribution of air temperature at a height of 1 m (Fig. 63a) shows an overall cooler regime than in summer condition, with values spanning from 26.5 °C to 30.5 °C. Scenarios S0 and S1 remain similar, with the warmest conditions concentrated across the more exposed central and upper regions of the domain and cooler air persisting along the southern area. In S2, the warm core undergoes a slight reduction in extent, while cooler classes undergo local expansion, particularly across the central-western region. However, the magnitude of the air temperature change remains modest, consistent with the suggestion of the previous summer analysis, that the intervention tends to affect air temperature less strongly than radiative and surface conditions.

The relative humidity at a height of 1 m (Fig. 63b) follows coherent patterns across scenarios, ranging from 24% to 40%, with higher values consistently occurring in the southern sector. Differences between S0 and S1 are limited and mostly local. In S2, there is a tendency for slight increases in humidity over more extensive regions of the domain, particularly in areas where vegetation has been introduced. This phenomenon can be attributed to a combination of enhanced evapotranspiration and a concurrent decrease in air temperature.

The most evident scenario contrasts are found in surface temperature (Fig. 63c). In S0, large exposed paved areas fall within the 41 to 48 °C range, with local hotspots reaching the highest

value (51.5 °C). In S1, surface temperatures become more spatially differentiated, with cooler patches emerging over specific paved surfaces while the hottest values remain associated with the most solar-exposed areas. In S2, the distinguishing characteristics of vegetation and shading become more evident. Several zones transition towards cooler classes, typically ranging from 34 to 41 °C, with local variations leading to lower temperatures. Concurrently, the warmest temperatures persist in areas where surfaces remain mineral and exposed to solar radiation.

Finally, mean radiant temperature at 1 m height (Fig. 63d) highlights the dominance of radiative exposure at pedestrian level. S0 and S1 are largely characterised by high MRT over exposed to solar radiation areas (generally 56 °C, with widespread sectors in the 62 to 74 °C range). In S2, shaded areas expand and the fraction of the domain with lower MRT increases, producing more frequent zones below the highest temperature. This finding substantiates the concept that, even under conditions of cooler air temperatures, shading emerges as the primary factor contributing to substantial reductions in radiative heat load. In contrast, material alterations alone tend to manifest smaller or more localized effects on MRT.

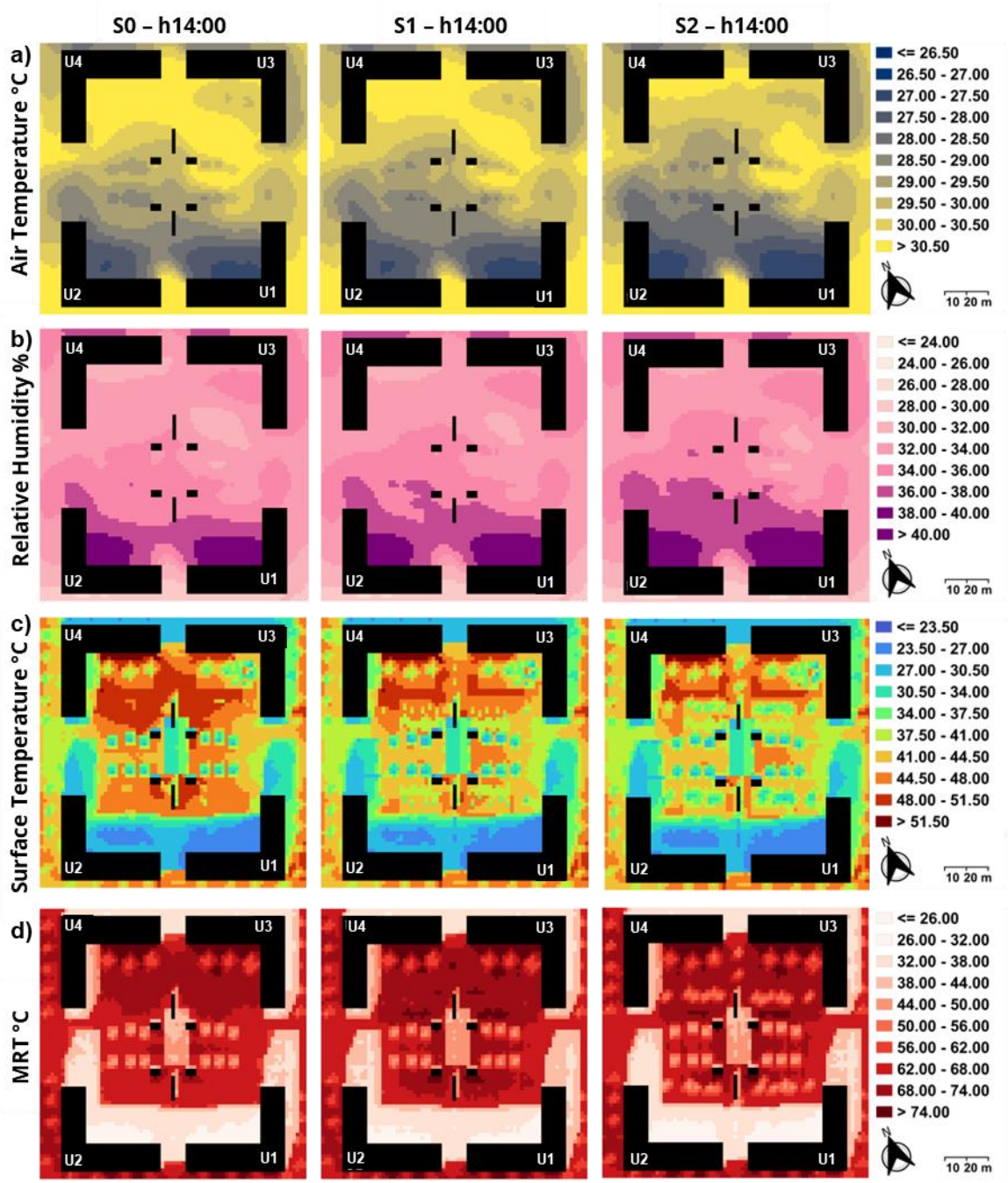

Fig. 63 The maps show the distribution of T_{air} (a), RH (b), T_{surf} (c) and MRT (d), at the same time for scenarios S0, S1 and S2

Air temperature at 1 m height (Fig. 64a) shows a similar diurnal cycle across the three scenarios, with a range of air temperature between 19 to 30 °C. Scenario S1 remains essentially aligned with S0 throughout the day, with only very small differences between medians. Scenario S2 demonstrates slightly more consistent cooling during the warmest hours; however, the effect remains modest. This suggests that, under these boundary conditions, the intervention does not primarily act by strongly lowering air temperature.

Relative humidity at 1 m height (Fig. 64b) follows an inverse pattern, with elevated values observed in the morning and evening hours, and a minimum around early afternoon. Differences between scenarios remain negligible overall. The difference of S2 from S0 and S1 is primarily characterized by a modest increase in humidity during the warm period of the day, which is consistent with increased evapotranspiration and a slight decrease in air temperatures. However, the magnitude is limited and does not change the general interpretation.

Surface temperature (Fig. 64c) exhibits the most significant variability and the most evident scenario sensitivity. Compared with S0, the post-regeneration scenarios reduce the upper tail of surface temperatures around midday and early afternoon. The curves related to materials underscore systematic differences between paving and soil types. In both S1 and S2, granite is consistently the coolest of the represented materials during peak heating, Luserna tends to be the warmest, and soil remains intermediate, with separations of a few degrees around the daily maximum. This confirms that, even when air temperature differences are small, changes in surface properties produce a clear and more robust signal in the surface thermal field.

Mean radiant temperature (Fig. 64d) remains the parameter where scenario contrasts are most relevant for perceived heat stress. S1 does not show a systematic improvement relative to S0 during the core hours of direct solar exposure, and a slight worsening is plausible where more reflective paving increases shortwave load. In S2, MRT is lower during the warmest hours and the afternoon, consistent with the added role of vegetation in reducing radiative exposure even when air-temperature reductions are limited. Overall, the figure (Fig. 64) reinforces the key point already emerging from the maps: material changes primarily reshape surface temperatures, while mature vegetation primarily improves comfort by reducing radiant load rather than by strongly cooling the air.

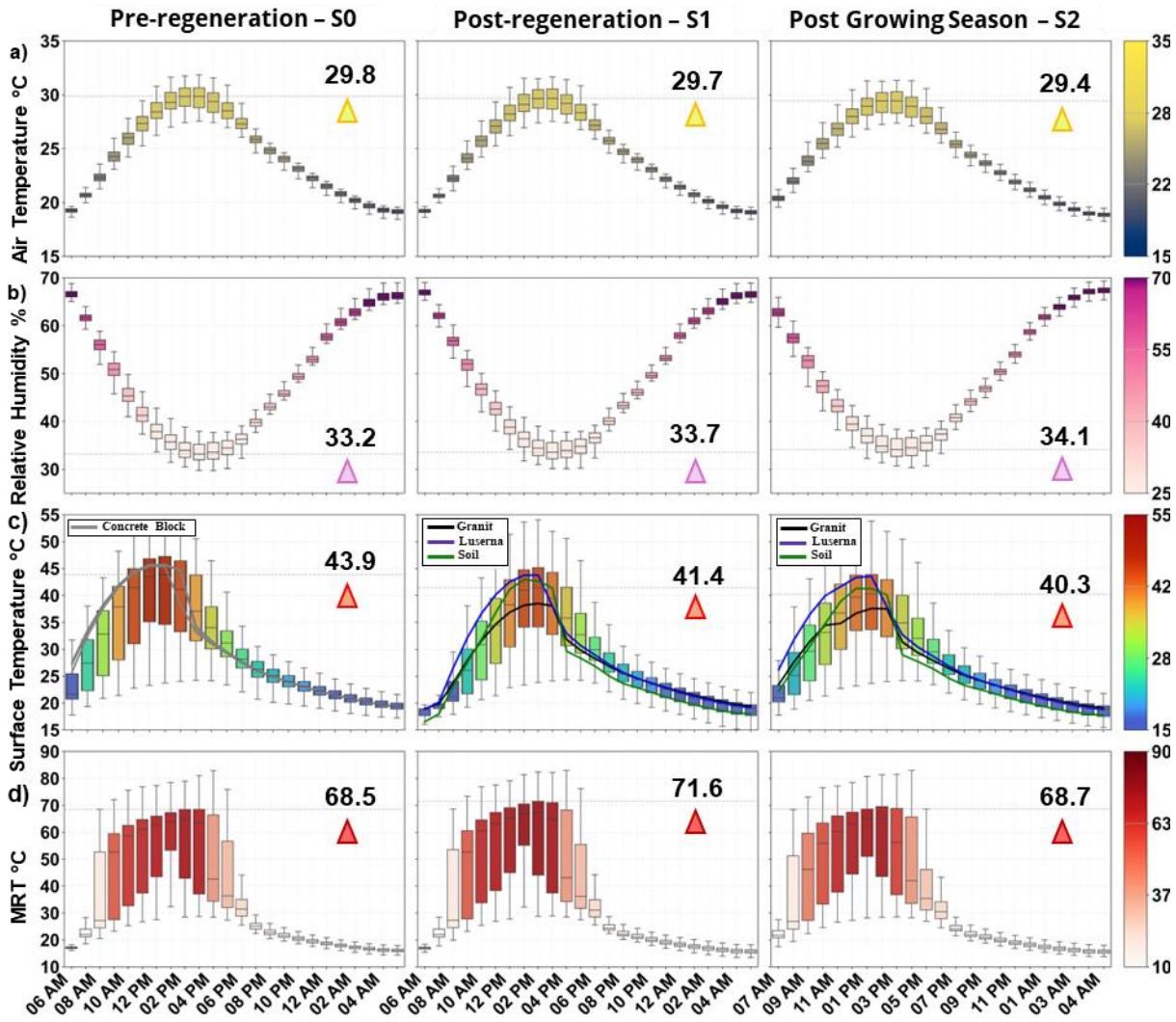

Fig. 64 Boxplot representation of T_{air} (a), RH (b), T_{surf} (c) and MRT (d), throughout the day for scenarios S0, S1 and S2. The lines in surface temperatures (c) graphs represent the different surfaces within the squares

5.2.5.2 Thermal comfort analysis

In the moderate reference conditions (Fig. 65), the overall comfort field shows the same spatial pattern, influenced by solar radiation exposure, observed in the hotter case, but with a generally reduced intensity. PET remains lowest in zones with persistent building shading, while the highest values are still concentrated in the most open and exposed portions of the courtyard. Compared to the hotter July day, the contrast between shaded and exposed areas is therefore preserved. This evidence suggests that geometry and direct solar access remain the primary determinants of peak discomfort even under less extreme boundary conditions.

The diurnal curves extracted at the four receptors confirm this behaviour. In S0, PET increases rapidly during the morning and reaches its maximum between late morning and early afternoon, with peaks in the most exposed locations still approaching or slightly exceeding 45 °C, corresponding to very high thermal stress. In S2, the presence of mature vegetation produces a systematic attenuation of peak PET during the hottest hours. The most significant reductions in temperature occur in areas where there is more shade provided by trees. This results in peak decreases in PET on the order of a few degrees (from 2 to 4 °C). In contrast, more areas receptors exhibit smaller benefits, with reductions ranging from 1–2 °C. As the afternoon progresses, the disparities in scenarios become increasingly minimal, indicating that under these less extreme conditions, the primary function of vegetation is predominantly to decrease the intensity and duration of the maximum diurnal thermal stress, as opposed to significantly affecting the nocturnal cooling process.

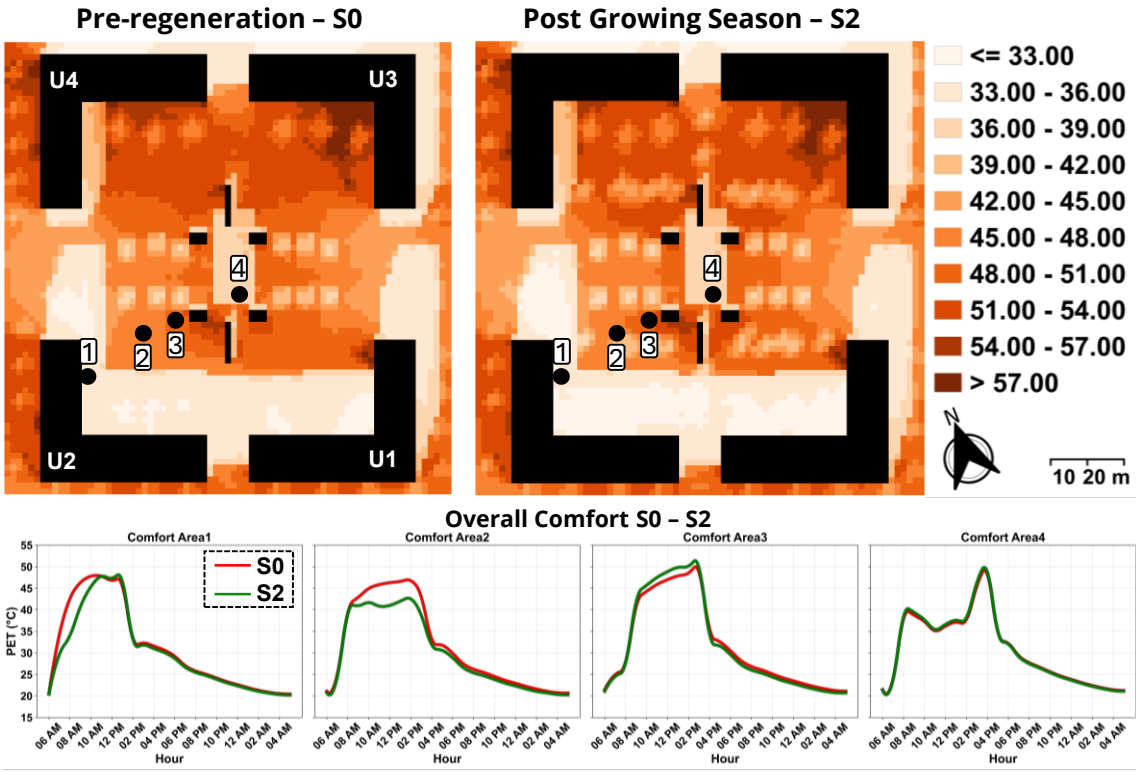

Fig. 65 Diurnal variation of the Physiological Equivalent Temperature (PET) at four receptors for the three simulated scenarios

As shown in Fig. 65, at stop 1 (first 10 minutes), all scenarios start from a comparatively better condition and then gradually drift towards lower comfort. The abrupt change occurs at

stop 2 (10–20 min): in S0 and S1, the receptor moves into a more exposed position and comfort drops and remains low for most of the stop, with only a small transient adjustment. S2 exhibits a distinct behaviour: the drop at Stop 2 is noticeably attenuated and comfort remains consistently higher than in S0 and S1 throughout this interval, coherent with the fact that the receptor is less exposed to direct solar radiations in this scenario.

During Stop 3 (20–30 min), comfort remains poor in all scenarios, indicating that this specific location and time frame are of critical importance even under less extreme boundary conditions. Finally, at stop 4, the move into the sheltered area produces an immediate improvement, followed by a stabilisation at a level that is still not fully comfortable. Overall, the key message is that scenario differences emerge mainly when the pedestrian is exposed: S2 does not alter near-ground conditions everywhere, it mitigates the most severe exposure moments, resulting in a more favourable comfort trajectory along the path.

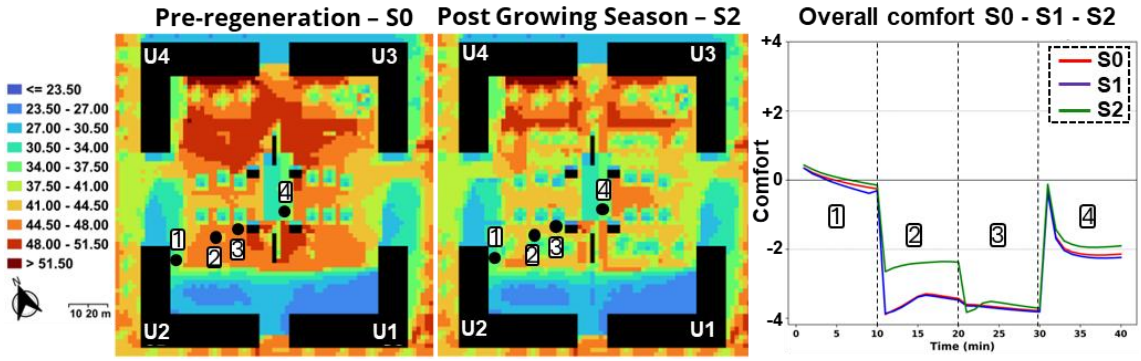

Fig. 66 The maps illustrate the pre-work and post-work scenarios with mature vegetation, where the points at which thermal comfort is measured are visible. The following three graphs illustrate the overall comfort levels in each scenario. The values ranging from -4 to +4 express comfort, with -4 representing the most uncomfortable condition (very uncomfortable) and +4 representing the most comfortable condition (very comfortable)

5.3 Discussion and conclusion

The present study utilised the redevelopment of Piazza della Scienza, a public square situated on the University of Milano-Bicocca campus in Milan, Italy, as a case study to quantify the microclimatic effects of feasible UHI mitigation measures. This was conducted using a combination of multi-sensor field monitoring and numerical simulations. The monitoring campaign captured the main environmental drivers and response variables, providing a detailed characterisation of local conditions and the empirical basis to inform and evaluate the modelling setup. A range of measurements were collected during different phases of the regeneration process. Consequently, the simulations were conducted retrospectively as a post-assessment, rather than as decision support for the project. The numerical analysis focused on the combined introduction of reflective paving materials and new vegetation, comparing the alternative configurations to estimate their impacts on key microclimatic variables and outdoor thermal comfort.

The monitoring campaign was carried out throughout the different phases of the project, allowing the square to be characterized under changing surface configurations and across different seasons. Fig. 9 provides a summary of the monitoring results for the three key stages of the regeneration work. It is notable that in both May (Fig. 9b) and August (Fig. 9c), the paved surfaces reached comparable temperature levels during the morning; however, later in the day, Luserna stone (L1) consistently exhibited higher temperatures compared to granite (G1). This behaviour is indicative of the distinct thermal and optical properties of the two materials, which primarily affect surface temperatures.

The simulation results demonstrate minimal variation for the variables examined in the three scenarios. Regarding air temperature, in Scenario S1, the new materials did not lead to significant reductions in air temperature, either in the proximity of the pavement or over the whole square. The biggest decrease of 0.2 °C was observed at 11 AM, in agreement with the range of 0.2–3 °C reported in literature for air temperature reductions associated with reflective materials (Santamouris, 2013; Tsoka et al., 2017). This behaviour can be attributed to the limited presence of granite slabs within the area, the surface with higher albedo than previous material. Moreover, no clear spatial correlation was found between areas with higher albedo and localized reductions in air temperature.

Changes in relative humidity were limited in both scenarios; even in S2, increases remained below 2 %, consistent with previous work reporting variations as low as 0.32 % (Ambrosini et al., 2014). In this context, relative humidity was not found to be a variable strongly affected by mitigation solutions.

Surface temperature showed a more marked response. The simulations confirmed the strong influence of albedo on surface temperature (Tsoka et al., 2018). After the intervention, T_{surf} decreased across the square, and larger increases in albedo led to larger temperature reductions. Granite, which showed an albedo increase of 0.32 compared to the pre-regeneration state, exhibited the largest cooling, whereas Luserna stone, with an increase of 0.10, produced more modest reductions. The recorded decreases were slightly below the 6–12.3 °C range reported by previous numerical studies (Tsoka et al., 2018) but followed the same trend and were consistent with other findings (Piselli et al., 2018). In Scenario S1, bare permeable soil reached relatively high surface temperatures, at times comparable to or higher than those of mineral surfaces, especially granite. This behaviour reflects the dry soil conditions assumed in the model. Although the site is irrigated at midday and late night (e.g. 3 AM) the model does not allow partial or time-specific irrigation, thus, soil surfaces remained dry and consequently warm the whole day. This aspect led to the maintenance of high surface temperature and significantly limited decrease in air temperature, as the thermal mitigation performance of grass grid pavers is strictly dependent on adequate water availability (Eingrüber et al., 2024).

In scenario S2, the vegetation in the flower beds was assumed to be fully developed. In this case, air temperature reductions were more evident, due to the combined effect of shading and evapotranspiration, through which vegetation cools the air (Bowler et al., 2010). However, ΔT_a (S0 - S2) remained below 1 °C over the 24-hour simulation, in agreement with studies that analyse the combined effect of cool materials and green infrastructure (Castaldo et al., 2017; Piselli et al., 2018). The comparison with S2 highlighted the cooling potential of tree cover: the canopy intercepted incoming solar radiation, limiting heat accumulation at ground level. Differences exceeding 10 °C were observed between exposed and shaded surfaces of identical material, in agreement with the numerical studies that investigated vegetation effects on surface temperature reductions (Piselli et al., 2018; Tsoka et al., 2018).

Mean radiant temperature exhibited strong spatial variability across the square, thereby confirming its dependence on radiative fluxes and material thermal properties (Matzarakis et al., 2010). MRT is highly sensitive to both direct and diffuse solar radiation and is considered a primary determinant of outdoor thermal comfort, especially in conditions of low wind speed (Rosso et al., 2018). The results, particularly those shown in Fig. 10, indicated that high-albedo materials may increase MRT and thus thermal discomfort, in accordance with previous studies (Tsoka et al., 2017; Piselli et al., 2018; Giorio and Paparella, 2023).

Wind advection provides another key element for interpreting the limited and spatially heterogeneous cooling observed in all scenarios. In consideration of the geometry of Piazza della Scienza, the wind flow is concentrated within a preferential corridor. During the day, when temperatures are high, this corridor facilitates the transport of warm air into the square, thereby compensating for part of the local cooling. Consequently, the simulated cooling in S2 remains spatially constrained: cooler air formed in shaded and leeward areas is only weakly exported downwind before being diluted by the dominant inflow. This finding is consistent with other evidence indicating that, in isolated urban spaces, the efficacy of local interventions in reducing near-ground Ta is significantly influenced by advection and urban geometry through channelling driven by temperature and pressure differences (Bartesaghi-Koc et al., 2021).

Vegetation is also essential to balance surface cooling and comfort. As indicated by Salata et al. (2017), tree canopies have the capacity to absorb up to 80% of incoming solar radiation, thereby reducing both shortwave reflections and longwave emissions. The difference in MRT between S1 and S2 reached values of about 25 °C in areas that changed from fully exposed to shaded, within the range of 4–37 °C reported in the literature. However, the overall improvement in MRT in S1 remained limited, and some zones even showed higher values than in S0 as well as for S2compared to S0, despite the increase in shading. The spatial patterns also confirmed the role of shading from adjacent buildings: east-west oriented sector of the square remained consistently warm during peak solar hours due to the lack of shade. The findings on thermal comfort reveal elevated levels of discomfort across all three scenarios. The locations analysed encompassed sun-exposed and shaded areas, all selected within areas designated for pedestrian passage and rest, in proximity to surfaces with elevated albedo. Consequently, the decrease in direct solar exposure was partially compensated for by

an increase in the contribution of reflected shortwave radiation. This increase in radiative load has the potential to compromise the comfort of pedestrians outdoors (Rosso et al., 2018; Song and Park, 2015).

The comfort results should also be interpreted in relation to the boundary conditions of the day analysed, which is representative of a typical July situation in Milan, characterised by high air temperatures, strong solar radiation and low wind speed. Under such extreme summer conditions, the absence of thermal comfort across the square is consistent with expectations.

Taken together, the findings suggest the relative role of surface materials and vegetation in compact regeneration projects. In this study, reflective paving resulted in negligible changes in near ground air temperature (e. g. 1 m height). However, under conditions of sun exposure, it led to an increase in MRT, which has a negative impact on pedestrian comfort. However, given the limitations of implementing vegetation uniformly, the design should prioritize the optimal spatial configuration of shading by trees and reflective surfaces. This configuration should target zones with the highest solar exposure and pedestrian use. The effectiveness of planted areas is influenced by soil moisture (Gao et al., 2024) and maintenance, necessitating the consideration of irrigation and soil-management practices in conjunction with layout and material choices.

This study shows that, beyond the specific test site, coupling dense, site-specific monitoring with scenario-based microscale simulations provides a robust basis for comparing regeneration options and attributing minor yet significant microclimatic differences to particular design choices. This integrated approach is particularly valuable in actual projects where the goals of mitigation and comfort must be balanced against practical constraints and where reliable local characterization is essential to minimize the risk of ineffective or counterproductive interventions.

Chapter 6

6 General remarks and conclusions

This thesis investigated urban overheating in Milan (Italy) through a multi-scale framework linking metropolitan SUHI patterns, mesoscale thermal heterogeneity and microscale microclimatic processes within a regenerating public space. Rather than treating these levels as independent domains, the study interprets them as a continuous chain in which each scale provides a complementary contribution, from the identification of large-scale spatial structures to the evaluation of site-specific exposure conditions and mitigation performance.

At the macroscale, the Urban Heat Island in Milan emerges as a spatially heterogeneous and structurally organised phenomenon, which cannot be reduced to a simple centre–periphery gradient. Instead, summertime overheating reflects the interaction between land cover, urban morphology and infrastructural systems, with the continuity of impervious surfaces and major urban corridors favouring the propagation of high surface temperatures, while vegetated and agricultural areas contribute to persistent cooling effects. In this sense, SUHI assumes an operational role, enabling the identification of priority areas for intervention within the metropolitan domain. At the mesoscale, the analysis of the Bicocca district demonstrates that thermal conditions are strongly differentiated within the urban fabric, and that overheating is largely driven by local variations in surface materials, geometry and land use. The integration of surface characterisation and distributed environmental monitoring highlights that thermal behaviour is highly context-dependent and cannot be interpreted through uniform assumptions. At the microscale, the study of Piazza della Scienza confirms that thermal exposure is ultimately experienced at pedestrian level and is directly reflected in thermal comfort conditions. The combined use of long-term monitoring and validated microclimatic modelling allows for a quantitative and scenario-based evaluation of mitigation strategies, showing that their effects are not always linear and may influence different components of the microclimatic system in distinct ways.

Taken together, these results highlight that urban overheating is scale-dependent not only in magnitude, but also in its driving mechanisms and in the effectiveness of mitigation measures. Macroscale analyses are essential to define spatial priorities and understand the

overall structure of the phenomenon, but they cannot capture the actual exposure experienced by users. Conversely, microscale analyses provide detailed and actionable insights but are inherently site-specific and require contextualisation within the broader urban system. The mesoscale plays a key bridging role, linking spatial patterns to local conditions and enabling a coherent interpretation of how urban form and land cover influence thermal behaviour. This integrated perspective suggests that effective heat mitigation cannot rely on a single level of analysis, but requires a coordinated approach in which diagnosis, prioritisation and design are informed by consistent evidence across scales.

From an applied perspective, the findings underline the need to translate climate objectives into context-specific and performance-driven design strategies. Mitigation measures are not universally interchangeable and should not be assumed to produce additive effects. Interventions based on materials and albedo may reduce surface temperatures but can also alter the radiative balance in ways that do not necessarily improve thermal comfort at pedestrian level. Conversely, shading- and vegetation-based solutions emerge as particularly effective in reducing thermal exposure, provided that they are properly designed, spatially configured and supported by realistic maintenance conditions. This implies that priority should be given to shading-oriented strategies in high-exposure areas, that vegetation should be treated as a functional component of the design rather than as an aesthetic addition, and that different measures should be combined and optimised according to local conditions and patterns of use. Within this framework, the validated microclimatic model represents not only a simulation tool but also a decision-support instrument, enabling the comparison of alternative scenarios and the verification of their expected performance before implementation.

In a context of increasing urban temperatures and intensifying climate risks, the main contribution of this work lies in providing an integrated and empirically grounded approach that connects large-scale thermal patterns with site-specific processes and design-oriented evaluation. By linking spatial diagnosis with measurable microclimatic performance, the study supports a transition from descriptive analyses to actionable and verifiable strategies for climate-sensitive urban regeneration.

7 Limitations and future works

This study has some limitations that should be acknowledged, which may inform the development of future research.

Firstly, the analysis at the macro- and mesoscale is based exclusively on data derived from Landsat 8 satellite imagery. While this dataset provides good spatial resolution and methodological consistency, the number of acquisitions available over time is limited and subject to constraints related to cloud cover. Moreover, this study does not consider near-surface air temperature, which is more closely related to human thermal perception. Future research could therefore integrate data from multiple satellite platforms to increase temporal density and improve the robustness of the analysis. It could also combine these datasets with in-situ air temperature measurements to provide a more comprehensive representation of the urban thermal environment.

Secondly, the microclimatic analysis does not explicitly include some key variables that influence outdoor thermal comfort. In particular, mean radiant temperature (MRT) and wind conditions were not measured directly, despite playing a crucial role in determining heat exchange between the human body and the surrounding environment. Future developments could include directly acquiring these parameters through field measurements or using microclimatic models to improve the calibration and validation of simulations and provide a more accurate assessment of thermal comfort conditions.

Additionally, while drone-based measurements were employed, the interaction between the UAV platform and onboard environmental sensors was not thoroughly investigated. A more detailed assessment of potential sources of uncertainty, together with an advanced data processing approach, could enable a more robust characterisation of the vertical air column and contribute to a more accurate description of local microclimatic conditions.

Finally, the evaluation of thermal comfort is based on a limited sample size and specific criteria, which may not fully capture the variability of human thermal perception. Thermal comfort is subjective and is influenced by physiological, behavioural and psychological factors. Future studies could extend the analysis to a larger, more diverse population and adopt different assessment methods to improve the robustness of the results.

References

Abdi, H., and Williams, L. J. (2010). Principal component analysis. In *Wiley Interdisciplinary Reviews: Computational Statistics* (Vol. 2, Number 4, pp. 433–459). https://doi.org/10.1002/wics.101

Abdollahzadeh, N., and Biloria, N. (2021). Outdoor thermal comfort: Analyzing the impact of urban configurations on the thermal performance of street canyons in the humid subtropical climate of Sydney. *Frontiers of Architectural Research*, *10*(2), 394–409. https://doi.org/10.1016/j.foar.2020.11.006

Acero, J. A., and Arrizabalaga, J. (2018). Evaluating the performance of ENVI-met model in diurnal cycles for different meteorological conditions. *Theoretical and Applied Climatology*, *131*(1–2), 455–469. https://doi.org/10.1007/s00704-016-1971-y

Acero, J. A., and Herranz-Pascual, K. (2015). A comparison of thermal comfort conditions in four urban spaces by means of measurements and modelling techniques. *Building and Environment*, *93*, 245–257. https://doi.org/10.1016/j.buildenv.2015.06.028

Akbari, H., and Konopacki, S. (2005). Calculating energy-saving potentials of heat-island reduction strategies. *Energy Policy*, *33*(6), 721–756. https://doi.org/10.1016/j.enpol.2003.10.001

Aleksandrowicz, O., Saroglou, T., and Pearlmutter, D. (2023). Evaluation of summer mean radiant temperature simulation in ENVI-met in a hot Mediterranean climate. *Building and Environment*, *245*, 110881. https://doi.org/10.1016/j.buildenv.2023.110881

Ambrosini, D., Galli, G., Mancini, B., Nardi, I., and Sfarra, S. (2014). Evaluating mitigation effects of urban heat islands in a historical small center with the ENVI-Met® climate model. *Sustainability (Switzerland)*, *6*(10), 7013–7029. https://doi.org/10.3390/su6107013

Anderson, G. B., and Bell, M. L. (2011). Heat Waves in the United States: Mortality Risk during Heat Waves and Effect Modification by Heat Wave Characteristics in 43 U.S. Communities. *Environmental Health Perspectives*, *119*(2), 210–218. https://doi.org/10.1289/ehp.1002313

Andreou, E. (2014). The effect of urban layout, street geometry and orientation on shading conditions in urban canyons in the Mediterranean. *Renewable Energy*, *63*, 587–596. https://doi.org/10.1016/j.renene.2013.09.051

Aoki, T., Kuchiki, K., Niwano, M., Kodama, Y., Hosaka, M., and Tanaka, T. (2011). Physically based snow albedo model for calculating broadband albedos and the solar heating profile in snowpack for general circulation models. *Journal of Geophysical Research*, *116*(D11), D11114. https://doi.org/10.1029/2010JD015507

ARPA. (2014). *L'aria che respiro: L'inquinamento atmosferico locale e globale*. www.regione.lombardia.it

Arrau, C. P., and Peña, M. A. (2010). The urban heat island (uhi) effect. *Urban Heat Islands (UHIs)*.

Bacci and Maugeri. (1992). The Urban Heat Island of Milan. *IL NUOVO CEMENTO*, *15 C*.

Baccini, M., Biggeri, A., Accetta, G., Kosatsky, T., Katsouyanni, K., Analitis, A., Anderson, H. R., Bisanti, L., D'Ippoliti, D., Danova, J., Forsberg, B., Medina, S., Paldy, A., Rabczenko, D., Schindler, C., and Michelozzi, P. (2008). Heat Effects on Mortality in 15 European Cities. *Epidemiology*, *19*(5), 711–719. https://doi.org/10.1097/EDE.0b013e318176bfcd

Bailey, S. C. C., Sama, M. P., Canter, C. A., Felipe Pampolini, L., Lippay, Z. S., Schuyler, T. J., Hamilton, J. D., Macphee, S. B., Rowe, I. S., Sanders, C. D., Smith, V. G., Vezzi, C. N., Wight, H. M., Hoagg, J. B., Guzman, M. I., and Smith, S. W. (2020). University of Kentucky measurements of wind, temperature, pressure and humidity in support of LAPSE-RATE using multisite fixed-wing and rotorcraft unmanned aerial systems. *Earth System Science Data*, *12*(3), 1759–1773. https://doi.org/10.5194/essd-12-1759-2020

Bartesaghi-Koc, C., Haddad, S., Pignatta, G., Paolini, R., Prasad, D., and Santamouris, M. (2021). Can urban heat be mitigated in a single urban street? Monitoring, strategies, and performance results from a real scale redevelopment project. *Solar Energy*, *216*, 564–588. https://doi.org/10.1016/j.solener.2020.12.043

Boeters, R., Donkers, S., Lee, D., Liem, V., Montazeri, S., van Oostveen, J., and Pietrzyk, P. (2012). *The effect of 3D geometry complexity on simulating radiative, conductive and convective fluxes in an urban canyon*.

Borghi, S., Corbetta, G., and De Biase, L. (2000). *A heat island model for large urban areas and its application to Milan (*)* (Vol. 23, Number 5).

Bowler, D. E., Buyung-Ali, L., Knight, T. M., and Pullin, A. S. (2010). Urban greening to cool towns and cities: A systematic review of the empirical evidence. *Landscape and Urban Planning*, *97*(3), 147–155. https://doi.org/10.1016/j.landurbplan.2010.05.006

Bruse, M. (2004). *ENVI-met 3.0: Updated Model Overview*.

Bruse, M., and Fleer, H. (1998). Simulating surface–plant–air interactions inside urban environments with a three dimensional numerical model. *Environmental Modelling and Software*, *13*(3–4), 373–384. https://doi.org/10.1016/S1364-8152(98)00042-5

Castaldo, V. L., Pisello, A. L., Pigliautile, I., Piselli, C., and Cotana, F. (2017). Microclimate and air quality investigation in historic hilly urban areas: Experimental and numerical investigation in central Italy. *Sustainable Cities and Society*, *33*, 27–44. https://doi.org/10.1016/j.scs.2017.05.017

Chatzidimitriou, A., and Yannas, S. (2015). Microclimate development in open urban spaces: The influence of form and materials. *Energy and Buildings*, *108*, 156–174. https://doi.org/10.1016/j.enbuild.2015.08.048

Cheng, C. Y., Cheung, K. K. S., and Chu, L. M. (2010). Thermal performance of a vegetated cladding system on facade walls. *Building and Environment*, *45*(8), 1779–1787. https://doi.org/10.1016/j.buildenv.2010.02.005

Ciacci, C., Banti, N., Di Naso, V., and Bazzocchi, F. (2023). Green strategies for improving urban microclimate and air quality: A case study of an Italian industrial district and facility. *Building and Environment*, *244*. https://doi.org/10.1016/j.buildenv.2023.110762

Clarke, F. J. (1969). *Nocturnal urban boundary layer over cincinnati, Ohio*. 582–589.

Comune di Milano. (2019a). *Piazze aperte. Da cittadini e associazioni proposte per 65 nuovi interventi*. https://www2.comune.milano.it/-/piazze-aperte.-da-cittadini-e-associazioni-proposte-per-65-nuovi-interventi

Comune di Milano. (2019b). *Verde. Nasce il fondo ForestaMi, obiettivo 3 milioni di alberi entro il 2030*. https://www2.comune.milano.it/-/verde.-nasce-il-fondo-forestami-obiettivo-3-milioni-di-alberi-entro-il-2030

Comune di Milano. (2025). *DIREZIONE RIGENERAZIONE URBANA AREA PIANIFICAZIONE ATTUATIVA 2*.

Crank, P. J., Sailor, D. J., Ban-Weiss, G., and Taleghani, M. (2018). Evaluating the ENVI-met microscale model for suitability in analysis of targeted urban heat mitigation strategies. *Urban Climate*, *26*, 188–197. https://doi.org/10.1016/j.uclim.2018.09.002

Datcu, S., Ibos, L., Candau, Y., and Matteï, S. (2005). Improvement of building wall surface temperature measurements by infrared thermography. *Infrared Physics and Technology*, *46*(6), 451–467. https://doi.org/10.1016/j.infrared.2005.01.001

De Ridder, K., Lauwaet, D., and Maiheu, B. (2015). UrbClim – A fast urban boundary layer climate model. *Urban Climate*, *12*, 21–48. https://doi.org/10.1016/j.uclim.2015.01.001

Deilami, K., Kamruzzaman, M., and Liu, Y. (2018). Urban heat island effect: A systematic review of spatio-temporal factors, data, methods, and mitigation measures. *International Journal of Applied Earth Observation and Geoinformation*, *67*, 30–42. https://doi.org/10.1016/J.JAG.2017.12.009

Detommaso, M., Costanzo, V., and Nocera, F. (2021). Application of weather data morphing for calibration of urban ENVI-met microclimate models. Results and critical issues. *Urban Climate*, *38*. https://doi.org/10.1016/j.uclim.2021.100895

Diem, J. E., Stauber, C. E., and Rothenberg, R. (2017). Heat in the southeastern United States: Characteristics, trends, and potential health impact. *PLOS ONE*, *12*(5), e0177937. https://doi.org/10.1371/journal.pone.0177937

Doulos, L., Santamouris, M., and Livada, I. (2004). Passive cooling of outdoor urban spaces. The role of materials. *Solar Energy*, *77*(2), 231–249. https://doi.org/10.1016/J.SOLENER.2004.04.005

EEA, E. E. A. (n.d.). *Climate-ADAPT Sharing adaptation knowledge for a Climate-Resilient Europe*. Retrieved January 25, 2026, from https://climate-adapt.eea.europa.eu/en/eu-adaptation-policy/sector-policies/urban

Eingrüber, N., Domm, A. S., Korres, W., and Schneider, K. (2024). *Simulation of the heat mitigation potential of unsealing measures in cities by parameterizing grass grid pavers for urban microclimate modelling with ENVI-met (V5)*. https://doi.org/10.5194/egusphere-2024-697

ENEA. (2006). *ENEA - Dipartimento Tecnologie Energetiche e Fonti Rinnovabili Atlante Italiano della Radiazione Solare*. Http://Www.Solaritaly.Enea.It/.

European Commission. (2018). *Management Plan 2019*.

European Commission. (2021). *COMMUNICATION FROM THE COMMISSION TO THE EUROPEAN PARLIAMENT, THE COUNCIL, THE EUROPEAN ECONOMIC AND SOCIAL COMMITTEE AND THE COMMITTEE OF THE REGIONS*. https://ec.europa.eu/jrc/en/peseta-iv/economic-impacts

Gagge, A. P. J. A. S. and Y. Nishi. (1972). An effective temperature scale based on a simple model of human physiological regulatiry response. *Memoirs of the Faculty of Engineering, Hokkaido University*, *13(Suppl)*, 21–36.

Gao, K., Haddad, S., Paolini, R., Feng, J., Altheeb, M., Mogirah, A. Al, Moammar, A. Bin, and Santamouris, M. (2024). The use of green infrastructure and irrigation in the mitigation of urban heat in a desert city. *Building Simulation*, *17*(5), 679–694. https://doi.org/10.1007/s12273-024-1110-0

Giorio, M., and Paparella, R. (2023). Climate Mitigation Strategies: The Use of Cool Pavements. *Sustainability (Switzerland)*, *15*(9). https://doi.org/10.3390/su15097641

Guattari, C., Evangelisti, L., and Balaras, C. A. (2018). On the assessment of urban heat island phenomenon and its effects on building energy performance: A case study of Rome (Italy). *Energy and Buildings*, *158*, 605–615. https://doi.org/10.1016/J.ENBUILD.2017.10.050

Han, D., Zhang, T., Qin, Y., Tan, Y., and Liu, J. (2023). A comparative review on the mitigation strategies of urban heat island (UHI): a pathway for sustainable urban development. In *Climate and Development* (Vol. 15, Number 5, pp. 379–403). Taylor and Francis Ltd. https://doi.org/10.1080/17565529.2022.2092051

Heaviside, C., Macintyre, H., and Vardoulakis, S. (2017). The Urban Heat Island: Implications for Health in a Changing Environment. In *Current environmental health*

reports (Vol. 4, Number 3, pp. 296–305). Springer. https://doi.org/10.1007/s40572-017-0150-3

Hotelling, H. (1933). Analysis of a complex of statistical variable into principal components. *J. Educ. Psych*, *24*, 417–441.

Howard, L. (1833). *The Climate of London Deduced from Meteorological Observations, Made in the Metropolis, and at Various Places Around It: Vol. 1-3* (Harvey and Darton, Ed.).

Hu, J., Zhou, Y., Yang, Y., Zhu, Z., Yang, J., Meng, X., and Lai, F. (2025). Multi-city local climate zone mapping and its quantitative applications on measuring surface urban heat Island in China. *Remote Sensing of Environment*, *330*. https://doi.org/10.1016/j.rse.2025.114965

Huizenga, C., Hui, Z., and Arens, E. (2001). A model of human physiology and comfort for assessing complex thermal environments. *Building and Environment*, *36*(6), 691–699. https://doi.org/10.1016/S0360-1323(00)00061-5

Huttner. (2012). *Further development and application of the 3D microclimate simulation ENVI-met*.

Imhoff, M. L., Zhang, P., Wolfe, R. E., and Bounoua, L. (2010). Remote sensing of the urban heat island effect across biomes in the continental USA. *Remote Sensing of Environment*, *114*(3), 504–513. https://doi.org/10.1016/J.RSE.2009.10.008

ISPRA. (2023). *Ambiente in Italia: uno sguardo d'insieme. Annuario dei dati ambientali 2022*. oma: Istituto Superiore per la Protezione e la Ricerca Ambientale. https://indicatoriambientali.isprambiente.it

Iungman, T., Cirach, M., Marando, F., Pereira Barboza, E., Khomenko, S., Masselot, P., Quijal-Zamorano, M., Mueller, N., Gasparrini, A., Urquiza, J., Heris, M., Thondoo, M., and Nieuwenhuijsen, M. (2023). Cooling cities through urban green infrastructure: a health impact assessment of European cities. *The Lancet*, *401*(10376), 577–589. https://doi.org/10.1016/S0140-6736(22)02585-5

Jabbar, H. K., Hamoodi, M. N., and Al-Hameedawi, A. N. (2023). Urban heat islands: a review of contributing factors, effects and data. *IOP Conference Series: Earth and Environmental Science*, *1129*(1). https://doi.org/10.1088/1755-1315/1129/1/012038

Jenkin, M. E., and Clemitshaw, K. C. (2000). Ozone and other secondary photochemical pollutants: chemical processes governing their formation in the planetary boundary layer. *Atmospheric Environment*, *34*(16), 2499–2527. https://doi.org/10.1016/S1352-2310(99)00478-1

Jiang, Z., Huete, A. R., Chen, J., Chen, Y., Li, J., Yan, G., and Zhang, X. (2006). Analysis of NDVI and scaled difference vegetation index retrievals of vegetation fraction. *Remote Sensing of Environment*, *101*(3), 366–378. https://doi.org/10.1016/j.rse.2006.01.003

Kalinkat, G., and Rall, B. C. (2015). Effects of climate change on the interactions between insect pests and their natural enemies. In *Climate change and insect pests* (pp. 74–91). CABI. https://doi.org/10.1079/9781780643786.0074

Kim, M., Lee, K., and Cho, G. H. (2017). Temporal and spatial variability of urban heat island by geographical location: A case study of Ulsan, Korea. *Building and Environment*, *126*, 471–482. https://doi.org/10.1016/J.BUILDENV.2017.10.023

Kim, S. W., and Brown, R. D. (2021). Urban heat island (UHI) intensity and magnitude estimations: A systematic literature review. In *Science of the Total Environment* (Vol. 779). Elsevier B.V. https://doi.org/10.1016/j.scitotenv.2021.146389

Kottek, M., Grieser, J., Beck, C., Rudolf, B., and Rubel, F. (2006). World Map of the Köppen-Geiger climate classification updated. *Meteorologische Zeitschrift*, *15*(3), 259–263. https://doi.org/10.1127/0941-2948/2006/0130

Krayenhoff, E. S., Broadbent, A. M., Zhao, L., Georgescu, M., Middel, A., Voogt, J. A., Martilli, A., Sailor, D. J., and Erell, E. (2021). Cooling hot cities: a systematic and critical review of the numerical modelling literature. *Environmental Research Letters*, *16*(5), 053007. https://doi.org/10.1088/1748-9326/abdcf1

Kyriakodis, G. E., and Santamouris, M. (2018). Using reflective pavements to mitigate urban heat island in warm climates - Results from a large scale urban mitigation project. *Urban Climate*, *24*, 326–339. https://doi.org/10.1016/j.uclim.2017.02.002

Lee, J., Zhang, H., and Arens, E. (2013). *UC Berkeley Indoor Environmental Quality (IEQ) Title Typical Clothing Ensemble Insulation Levels for Sixteen Body Parts*. http://escholarship.org/uc/item/18f0r375

Lietzke, B., Vogt, R., Young, D. T., Castro, E. A. de., and Moors, E. J. . (2015). *Understanding urban metabolism : a tool for urban planning*. Routledge.

Lin, P., Lau, S. S. Y., Qin, H., and Gou, Z. (2017). Effects of urban planning indicators on urban heat island: a case study of pocket parks in high-rise high-density environment. *Landscape and Urban Planning*, *168*, 48–60. https://doi.org/10.1016/j.landurbplan.2017.09.024

Lindberg, F., Holmer, B., and Thorsson, S. (2008). SOLWEIG 1.0 – Modelling spatial variations of 3D radiant fluxes and mean radiant temperature in complex urban settings. *International Journal of Biometeorology*, *52*(7), 697–713. https://doi.org/10.1007/s00484-008-0162-7

Liu, H., He, B. jie, Gao, S., Zhan, Q., and Yang, C. (2023). Influence of non-urban reference delineation on trend estimate of surface urban heat island intensity: A comparison of seven methods. *Remote Sensing of Environment*, *296*. https://doi.org/10.1016/j.rse.2023.113735

Lobaccaro, G., De Ridder, K., Acero, J. A., Hooyberghs, H., Lauwaet, D., Maiheu, B., Sharma, R., and Govehovitch, B. (2021). Applications of models and tools for mesoscale and microscale thermal analysis in mid-latitude climate regions—A review. In *Sustainability (Switzerland)* (Vol. 13, Number 22). MDPI. https://doi.org/10.3390/su132212385

Loveland, T. R., and Irons, J. R. (2016). Landsat 8: The plans, the reality, and the legacy. *Remote Sensing of Environment*, *185*, 1–6. https://doi.org/10.1016/j.rse.2016.07.033

Luber, G., and McGeehin, M. (2008). Climate Change and Extreme Heat Events. *American Journal of Preventive Medicine*, *35*(5), 429–435. https://doi.org/10.1016/J.AMEPRE.2008.08.021

MacQueen, J. (1967). Multivariate observations. *Proceedings Ofthe 5th Berkeley Symposium on Mathematical Statisticsand Probability*, *1*, 281–297.

Makido, Y., Shandas, V., Ferwati, S., and Sailor, D. (2016). Daytime Variation of Urban Heat Islands: The Case Study of Doha, Qatar. *Climate*, *4*(2), 32. https://doi.org/10.3390/cli4020032

Makropoulou, M. (2017). Microclimate improvement of Inner-city urban areas in a Mediterranean coastal city. *Sustainability (Switzerland)*, *9*(6). https://doi.org/10.3390/su9060882

Manteghi, G., Limit, H. Bin, and Remaz, D. (2015). Water Bodies an Urban Microclimate: A Review. *Modern Applied Science*, *9*(6). https://doi.org/10.5539/mas.v9n6p1

Marando, F., Heris, M. P., Zulian, G., Udías, A., Mentaschi, L., Chrysoulakis, N., Parastatidis, D., and Maes, J. (2022). Urban heat island mitigation by green infrastructure in European Functional Urban Areas. *Sustainable Cities and Society*, *77*, 103564. https://doi.org/10.1016/J.SCS.2021.103564

Maronga, B., Banzhaf, S., Burmeister, C., Esch, T., Forkel, R., Fröhlich, D., Fuka, V., Gehrke, K. F., Geletič, J., Giersch, S., Gronemeier, T., Groß, G., Heldens, W., Hellsten, A., Hoffmann, F., Inagaki, A., Kadasch, E., Kanani-Sühring, F., Ketelsen, K., … Raasch, S. (2020). Overview of the PALM model system 6.0. *Geoscientific Model Development*, *13*(3), 1335–1372. https://doi.org/10.5194/gmd-13-1335-2020

Masson, V., Lemonsu, A., Hidalgo, J., and Voogt, J. (2020). *Urban Climates and Climate Change*. https://doi.org/10.1146/annurev-environ-012320

Matzarakis, A., Rutz, F., and Mayer, H. (2007). Modelling radiation fluxes in simple and complex environments—application of the RayMan model. *International Journal of Biometeorology*, *51*(4), 323–334. https://doi.org/10.1007/s00484-006-0061-8

Matzarakis, A., Rutz, F., and Mayer, H. (2010). Modelling radiation fluxes in simple and complex environments: basics of the RayMan model. *International Journal of Biometeorology*, *54*(2), 131–139. https://doi.org/10.1007/s00484-009-0261-0

Mazzali, U., Peron, F., Romagnoni, P., Pulselli, R. M., and Bastianoni, S. (2013). Experimental investigation on the energy performance of Living Walls in a temperate climate. *Building and Environment*, *64*, 57–66. https://doi.org/10.1016/j.buildenv.2013.03.005

Meier, P., Holloway, T., Patz, J., Harkey, M., Ahl, D., Abel, D., Schuetter, S., and Hackel, S. (2017). Impact of warmer weather on electricity sector emissions due to building energy use. *Environmental Research Letters*, *12*(6), 064014. https://doi.org/10.1088/1748-9326/aa6f64

Meng, F., Qin, M., Gao, Z., Wang, H., Xu, X., and Xu, F. (2025). A review of RayMan in thermal comfort simulation: Development, applications and prospects. *Building and Environment*, *270*, 112547. https://doi.org/10.1016/j.buildenv.2025.112547

Middel, A., Häb, K., Brazel, A. J., Martin, C. A., and Guhathakurta, S. (2014). Impact of urban form and design on mid-afternoon microclimate in Phoenix Local Climate Zones. *Landscape and Urban Planning*, *122*, 16–28. https://doi.org/10.1016/j.landurbplan.2013.11.004

Mineo, S., and Pappalardo, G. (2021). Rock emissivity measurement for infrared thermography engineering geological applications. *Applied Sciences (Switzerland)*, *11*(9). https://doi.org/10.3390/app11093773

Mutani, G., Todeschi, V., and Beltramino, S. (2022). Improving Outdoor Thermal Comfort in Built Environment Assessing the Impact of Urban Form and Vegetation. *International Journal of Heat and Technology*, *40*(1), 23–31. https://doi.org/10.18280/ijht.400104

Nagy, L. and D. F. (2004). *EUFORGEN Technical Guidelines for genetic conservation and use for field maple (Acer campestre)*.

Ng, E. R. C. (2015). *The urban climatic map: a methodology for sustainable urban planning* (C. Ren, Ed.). Routledge.

Nuvolati, G. ; B. G. (2018). *Raccontare un quartiere. Luoghi, volti e memorie della Bicocca*. https://doi.org/https://hdl.handle.net/10281/219564

Oke, T. R. (1976). The distinction between canopy and boundary-layer urban heat islands. *Atmosphere*, *14*(4), 268–277. https://doi.org/10.1080/00046973.1976.9648422

Oke, T. R. (1982). The energetic basis of the urban heat island. *Quarterly Journal of the Royal Meteorological Society*, *108*(455), 1–24. https://doi.org/10.1002/qj.49710845502

Oke, T. R. (1988). Street design and urban canopy layer climate. *Energy and Buildings*, *11*(1–3), 103–113. https://doi.org/10.1016/0378-7788(88)90026-6

Oke, T. R. (1995). The Heat Island of the Urban Boundary Layer: Characteristics, Causes and Effects. In *Wind Climate in Cities* (pp. 81–107). Springer Netherlands. https://doi.org/10.1007/978-94-017-3686-2_5

Oke, T. R. (2002). *Boundary Layer Climates* (Second). Taylor and Francis Group.

Oke, T. R., Johnson, G. T., Steyn, D. G., and Watson, I. D. (1991). Simulation of surface urban heat islands under ?ideal? conditions at night part 2: Diagnosis of causation. *Boundary-Layer Meteorology*, *56*(4), 339–358. https://doi.org/10.1007/BF00119211

Oke, T. R., Millis, Gerald., Christen, A., and Voogt, J. A. (2017). *Urban Climates* (United States: Cambridge University Press, Ed.).

Oliveira, S., Andrade, H., and Vaz, T. (2011). The cooling effect of green spaces as a contribution to the mitigation of urban heat: A case study in Lisbon. *Building and Environment*, *46*(11), 2186–2194. https://doi.org/10.1016/j.buildenv.2011.04.034

Olivieri, F., Sassenou, L.-N., and Olivieri, L. (2024). Potential of Nature-Based Solutions to Diminish Urban Heat Island Effects and Improve Outdoor Thermal Comfort in Summer: Case Study of Matadero Madrid. *Sustainability*, *16*(7), 2778. https://doi.org/10.3390/su16072778

Oxoli, D., Ronchetti, G., Minghini, M., Molinari, M. E., Lotfian, M., Sona, G., and Brovelli, M. A. (2018). Measuring urban land cover influence on air temperature through multiple geo-data—the case of Milan, Italy. *ISPRS International Journal of Geo-Information*, *7*(11). https://doi.org/10.3390/ijgi7110421

Palusci, O., Laurino, V., Barbieri, V., and Buccolieri, R. (2023). Identifying and monitoring the Urban Heat Island in the compact Mediterranean city using satellite imagery and in-situ measurement data. *Journal of Physics: Conference Series*, *2600*(9). https://doi.org/10.1088/1742-6596/2600/9/092006

Pantavou, K., Theoharatos, G., Mavrakis, A., and Santamouris, M. (2011). Evaluating thermal comfort conditions and health responses during an extremely hot summer in Athens. *Building and Environment*, *46*(2), 339–344. https://doi.org/10.1016/j.buildenv.2010.07.026

Pearson, K. (1901). On lines and planes of closest fit to systems of points in space. *Philosophical Magazine 2*, *11*, 559–572.

Peel, M. C., Finlayson, B. L., and McMahon, T. A. (2007). Updated world map of the Köppen-Geiger climate classification. *Hydrology and Earth System Sciences*, *11*(5), 1633–1644. https://doi.org/10.5194/hess-11-1633-2007

Pena Acosta, M., Vahdatikhaki, F., Santos, J., and Dorée, A. G. (2023). A comparative analysis of surface and canopy layer urban heat island at the micro level using a data-driven approach. *Sustainable Cities and Society*, *99*. https://doi.org/10.1016/j.scs.2023.104944

Perini, K., and Magliocco, A. (2014). Effects of vegetation, urban density, building height, and atmospheric conditions on local temperatures and thermal comfort. *Urban Forestry and Urban Greening*, *13*(3), 495–506. https://doi.org/10.1016/j.ufug.2014.03.003

Pichierri, M., Bonafoni, S., and Biondi, R. (2012). Satellite air temperature estimation for monitoring the canopy layer heat island of Milan. *Remote Sensing of Environment*, *127*, 130–138. https://doi.org/10.1016/j.rse.2012.08.025

Piselli, C., Castaldo, V. L., Pigliautile, I., Pisello, A. L., and Cotana, F. (2018). Outdoor comfort conditions in urban areas: On citizens' perspective about microclimate mitigation of urban transit areas. *Sustainable Cities and Society*, *39*, 16–36. https://doi.org/10.1016/j.scs.2018.02.004

Podaras, P. and B. N. (1996). The propagation of lesser known and unusual maple species. *Combined Proceedings International Plant Propagator's Society*, 497–507.

Puche, M., Vavassori, A., and Brovelli, M. A. (2023). Insights into the Effect of Urban Morphology and Land Cover on Land Surface and Air Temperatures in the Metropolitan City of Milan (Italy) Using Satellite Imagery and In Situ Measurements. *Remote Sensing*, *15*(3). https://doi.org/10.3390/rs15030733

Regione Lombardia. (2023). *Uso e Copertura del Suolo 2021 (DUSAF 7.0)*. Geoportale della Lombardia.

Rizwan, A. M., Dennis YC, L., Leung, D. Y., and Chunho, L. (2008). A review on the generation, determination and mitigation of Urban Heat Island. In *Journal of Environmental Sciences* (Vol. 20).

Rosso, F., Golasi, I., Castaldo, V. L., Piselli, C., Pisello, A. L., Salata, F., Ferrero, M., Cotana, F., and de Lieto Vollaro, A. (2018). On the impact of innovative materials on outdoor thermal comfort of pedestrians in historical urban canyons. *Renewable Energy*, *118*, 825–839. https://doi.org/10.1016/j.renene.2017.11.074

Rouse Jr, J. W. , H. R. H. (1974). Paper A 20. *Third Earth Resources Technology Satellite-1 Symposium: Section AB. Technical Presentations.*, *351*, 309.

Salata, F., Golasi, I., de Lieto Vollaro, R., and de Lieto Vollaro, A. (2016). Urban microclimate and outdoor thermal comfort. A proper procedure to fit ENVI-met simulation outputs to experimental data. *Sustainable Cities and Society*, *26*, 318–343. https://doi.org/10.1016/j.scs.2016.07.005

Salata, F., Golasi, I., Petitti, D., de Lieto Vollaro, E., Coppi, M., and de Lieto Vollaro, A. (2017). Relating microclimate, human thermal comfort and health during heat waves: An analysis of heat island mitigation strategies through a case study in an urban outdoor environment. *Sustainable Cities and Society*, *30*, 79–96. https://doi.org/10.1016/j.scs.2017.01.006

Salvati, L., Zambon, I., Pignatti, G., Colantoni, A., Cividino, S., Perini, L., Pontuale, G., and Cecchini, M. (2019). A Time-Series Analysis of Climate Variability in Urban and Agricultural Sites (Rome, Italy). *Agriculture*, *9*(5), 103. https://doi.org/10.3390/agriculture9050103

Santamouris, M. (2013). Using cool pavements as a mitigation strategy to fight urban heat island—A review of the actual developments. *Renewable and Sustainable Energy Reviews*, *26*, 224–240. https://doi.org/10.1016/j.rser.2013.05.047

Santamouris, M. (2014a). Cooling the cities – A review of reflective and green roof mitigation technologies to fight heat island and improve comfort in urban environments. *Solar Energy*, *103*, 682–703. https://doi.org/10.1016/j.solener.2012.07.003

Santamouris, M. (2014b). On the energy impact of urban heat island and global warming on buildings. *Energy and Buildings*, *82*, 100–113. https://doi.org/10.1016/J.ENBUILD.2014.07.022

Santamouris, M. (2015). Analyzing the heat island magnitude and characteristics in one hundred Asian and Australian cities and regions. *Science of The Total Environment*, *512–513*, 582–598. https://doi.org/10.1016/j.scitotenv.2015.01.060

Santamouris, M. (2020). Recent progress on urban overheating and heat island research. Integrated assessment of the energy, environmental, vulnerability and health impact.

Synergies with the global climate change. In *Energy and Buildings* (Vol. 207). Elsevier Ltd. https://doi.org/10.1016/j.enbuild.2019.109482

Santamouris, M., Cartalis, C., Synnefa, A., and Kolokotsa, D. (2015). On the impact of urban heat island and global warming on the power demand and electricity consumption of buildings—A review. *Energy and Buildings*, *98*, 119–124. https://doi.org/10.1016/J.ENBUILD.2014.09.052

Sarrat, C., Lemonsu, A., Masson, V., and Guedalia, D. (2006). Impact of urban heat island on regional atmospheric pollution. *Atmospheric Environment*, *40*(10), 1743–1758. https://doi.org/10.1016/j.atmosenv.2005.11.037

Sawka, M., Millward, A. A., Mckay, J., and Sarkovich, M. (2013). Growing summer energy conservation through residential tree planting. *Landscape and Urban Planning*, *113*, 1–9. https://doi.org/10.1016/j.landurbplan.2013.01.006

Schinasi, L. H., Benmarhnia, T., and De Roos, A. J. (2018). Modification of the association between high ambient temperature and health by urban microclimate indicators: A systematic review and meta-analysis. *Environmental Research*, *161*, 168–180. https://doi.org/10.1016/J.ENVRES.2017.11.004

Seto, K. C., Güneralp, B., and Hutyra, L. R. (2012). Global forecasts of urban expansion to 2030 and direct impacts on biodiversity and carbon pools. *Proceedings of the National Academy of Sciences*, *109*(40), 16083–16088. https://doi.org/10.1073/pnas.1211658109

Skamarock, W. C. ; K. J. B. (2024). *Weather Research and Forecasting (WRF) Model*. National Center for Atmospheric Research (NCAR).

Song, B., and Park, K. (2015). Contribution of greening and high-albedo coatings to improvements in the thermal environment in complex urban areas. *Advances in Meteorology*, *2015*. https://doi.org/10.1155/2015/792172

Stathopoulou, E., Mihalakakou, G., Santamouris, M., and Bagiorgas, H. S. (2008). *On the impact of temperature on tropospheric ozone concentration levels in urban environments*.

Stewart, I. D., and Oke, T. R. (2012). Local climate zones for urban temperature studies. *Bulletin of the American Meteorological Society*, *93*(12), 1879–1900. https://doi.org/10.1175/BAMS-D-11-00019.1

Stocker, T. (2014). *Climate change 2013: the physical science basis: Working Group I contribution to the Fifth assessment report of the Intergovernmental Panel on Climate Change.* Cambridge university press.

Stolwijk, J. A. J., and Hardy, J. D. (1966). Temperature regulation in man ? A theoretical study. *Pflugers Arch Gesamte Physiol Menschen Tiere*, *291*(2), 129–162. https://doi.org/10.1007/BF00412787

Stone, B., Hess, J. J., and Frumkin, H. (2010). Urban Form and Extreme Heat Events: Are Sprawling Cities More Vulnerable to Climate Change Than Compact Cities? *Environmental Health Perspectives*, *118*(10), 1425–1428. https://doi.org/10.1289/ehp.0901879

Taleghani, M., and Berardi, U. (2018). The effect of pavement characteristics on pedestrians' thermal comfort in Toronto. *Urban Climate*, *24*, 449–459. https://doi.org/10.1016/j.uclim.2017.05.007

Tanabe, S., Nomoto, A., Takahashi, Y., and Ogawa, Y. (2023). *Human Thermal Comfort Modeling* (pp. 61–78). https://doi.org/10.1007/978-981-99-0718-2_4

Toparlar, Y., Blocken, B., Maiheu, B., and van Heijst, G. J. F. (2017). A review on the CFD analysis of urban microclimate. *Renewable and Sustainable Energy Reviews*, *80*, 1613–1640. https://doi.org/10.1016/j.rser.2017.05.248

Tsoka, S., Tsikaloudaki, A., and Theodosiou, T. (2018). Analyzing the ENVI-met microclimate model's performance and assessing cool materials and urban vegetation applications–A review. In *Sustainable Cities and Society* (Vol. 43, pp. 55–76). Elsevier Ltd. https://doi.org/10.1016/j.scs.2018.08.009

Tsoka, S., Tsikaloudaki, K., and Theodosiou, T. (2017). Urban space's morphology and microclimatic analysis: A study for a typical urban district in the Mediterranean city of Thessaloniki, Greece. *Energy and Buildings*, *156*, 96–108. https://doi.org/10.1016/j.enbuild.2017.09.066

Tucker, C. J. (1979). Red and photographic infrared linear combinations for monitoring vegetation. *Remote Sensing of Environment*, *8*(2), 127–150. https://doi.org/10.1016/0034-4257(79)90013-0

UNFCCC. (2016). *Climate action now: summary for policymakers 2016* (phoenix design Aid, Ed.). United Nations Framework Convention on Climate Change.

Vailshery, L. S., Jaganmohan, M., and Nagendra, H. (2013). Effect of street trees on microclimate and air pollution in a tropical city. *Urban Forestry and Urban Greening*, *12*(3), 408–415. https://doi.org/10.1016/j.ufug.2013.03.002

Vemado, F., and Pereira Filho, A. J. (2016). Severe Weather Caused by Heat Island and Sea Breeze Effects in the Metropolitan Area of São Paulo, Brazil. *Advances in Meteorology*, *2016*, 1–13. https://doi.org/10.1155/2016/8364134

Vieira Zezzo, L., Pereira Coltri, P., and Dubreuil, V. (2023). Microscale models and urban heat island studies: a systematic review. In *Environmental Monitoring and Assessment* (Vol. 195, Number 11). Springer Science and Business Media Deutschland GmbH. https://doi.org/10.1007/s10661-023-11906-2

Vogel, J., Afshari, A., Chockalingam, G., and Stadler, S. (2022). Evaluation of a novel WRF/PALM-4U coupling scheme incorporating a roughness-corrected surface layer representation. *Urban Climate*, *46*. https://doi.org/10.1016/j.uclim.2022.101311

Vollmer, Michael., and Mollmann, K.-P. (2008). *Handbook of optical systems. Volume 4, Survey of optical systems*. Wiley-VCH.

Voogt, J. A., and Oke, T. R. (2003). Thermal remote sensing of urban climates. *Remote Sensing of Environment*, *86*(3), 370–384. https://doi.org/10.1016/S0034-4257(03)00079-8

Wang, Y., Bakker, F., de Groot, R., Wörtche, H., and Leemans, R. (2015). Effects of urban green infrastructure (UGI) on local outdoor microclimate during the growing season. *Environmental Monitoring and Assessment*, *187*(12), 732. https://doi.org/10.1007/s10661-015-4943-2

Wise, E. K. (2008). Climate-based sensitivity of air quality to climate change scenarios for the southwestern United States. *International Journal of Climatology*, *29*(1), 87–97. https://doi.org/10.1002/joc.1713

World Bank. (2020). *Analysis of Heat Waves and Urban Heat Island Effects in Central European Cities and Implications for Urban Planning The International Bank for Reconstruction and Development*.

World Population Prospects. (2024). *World Population Prospects 2024: Ten Key Messages*.

World Urbanization Prospects Revision. (2019). *World Urbanization Prospects: The 2018 Revision*. UN. https://doi.org/10.18356/b9e995fe-en

Yamato, H., Mikami, T., and Takahashi, H. (2017). Impact of sea breeze penetration over urban areas on midsummer temperature distributions in the Tokyo Metropolitan area. *International Journal of Climatology*, *37*(15), 5154–5169. https://doi.org/10.1002/joc.5152

Yang, X., Zhao, L., Bruse, M., and Meng, Q. (2013). Evaluation of a microclimate model for predicting the thermal behavior of different ground surfaces. *Building and Environment*, *60*, 93–104. https://doi.org/10.1016/j.buildenv.2012.11.008

Yuan, F., and Bauer, M. E. (2007). Comparison of impervious surface area and normalized difference vegetation index as indicators of surface urban heat island effects in Landsat imagery. *Remote Sensing of Environment*, *106*(3), 375–386. https://doi.org/10.1016/j.rse.2006.09.003

Zha, Y. J. G. and S. N. (2003). Use of normalized difference built-up index in automatically mapping urban areas from TM imagery. *International Journal of Remote Sensing*, *24.3*, 583–594.

Zhang, H., Arens, E., Huizenga, C., and Han, T. (2010a). Thermal sensation and comfort models for non-uniform and transient environments: Part I: Local sensation of individual body parts. *Building and Environment*, *45*(2), 380–388. https://doi.org/10.1016/j.buildenv.2009.06.018

Zhang, H., Arens, E., Huizenga, C., and Han, T. (2010b). Thermal sensation and comfort models for non-uniform and transient environments, part II: Local comfort of individual body parts. *Building and Environment*, *45*(2), 389–398. https://doi.org/10.1016/j.buildenv.2009.06.015

Zhang, H., Arens, E., Huizenga, C., and Han, T. (2010c). Thermal sensation and comfort models for non-uniform and transient environments, part III: Whole-body sensation and comfort. *Building and Environment*, *45*(2), 399–410. https://doi.org/10.1016/j.buildenv.2009.06.020

Zhou, D., Xiao, J., Bonafoni, S., Berger, C., Deilami, K., Zhou, Y., Frolking, S., Yao, R., Qiao, Z., and Sobrino, J. A. (2019). Satellite remote sensing of surface urban heat islands: Progress, challenges, and perspectives. In *Remote Sensing* (Vol. 11, Number 1). MDPI AG. https://doi.org/10.3390/rs11010048

Tesi di dottorato realizzata nell'ambito del progetto MUSA finanziato dal PNRR Missione 4 Comonente 2 Investimento 1.5, finanziato dall'Unione Europea - NextGenerationEU - CUP H43C22000550001